EVAPORATIVE HOTSPOT COOLING OF MICROPROCESSORS USING ELECTROWETTING ON DIELECTRIC (EWOD)

by

ARVIND VENKATESAN

Presented to the Faculty of the Graduate School of
The University of Texas at Arlington in Partial Fulfillment
of the Requirements
for the Degree of

DOCTOR OF PHILOSOPHY

THE UNIVERSITY OF TEXAS AT ARLINGTON
December 2018

Copyright © by Arvind venkatesan 2018

All Rights Reserved

To my parents and wife

ACKNOWLEDGEMENTS

First and foremost, I would like to thank my supervisor, Dr. Hyejin moon, for her great support and guidance throughout my PhD. She has been an excellent mentor and has guided my research with utmost patience. She has always provided me with invaluable feedback and positively influenced me in making the right decisions. Dr. Moon's dedication and passion towards research has inspired me to conduct my own research with great zeal. I am forever thankful to Dr. Moon for taking me into her research group and guiding me.

I would like to express my sincere thanks to my committee members Dr. Frank lu, Dr. Ratan kumar, Dr. Choong-Un kim, Dr. Ashfaq adnan and Dr. Miguel amaya. Their critical feedback has helped immensely to portray my research work in a better light and improved the quality of this dissertation. They have been very kind and accommodating in their schedules. I would also to thank Dr. Seiichi nomura, Lanie gordon, Ayesha fatima and Wendy ryan for helping me with the administrative side during my studies.

I am grateful to Shreyas bindiganevale and Jagath nikapitiya for inspiring this research. I would like to offer special thanks to Shimadzu institute for research technologies, UT Arlington for supporting this research through their wonderful fabrication facilities. And more specifically, I am thankful to Dennis bueno and Richard chambers for spending countless hours in troubleshooting my fabrication. I would like to extend special thanks to Dr. Anirudh balram, Bryan steinhoff and Dr. Sunand santhanagopalan for supporting my research by providing me with their proprietary superhydrophilic coating.

Many thanks to my lab mates Ali farzbod, Mun mun nahar, Shubhodeep paul, Matin torabinia, Omkar pawar, Subhadeep chakraborti, Kunjan chaudhari, Chintan gandhi, Ibaad habib, Viraj sabane and Ajinkya shetye for their support throughout my PhD studies. It has been a memorable experience working with them. I will always cherish the fun we had during our lab outings and memories we created for ourselves. I wish them all the very best for their future endeavors.

I am extremely thankful and grateful to my father, Mr. Venkatesan rajagopalan, for always being there for me and imparting me with practical friendly advice. He has provided me with many invaluable life lessons, but the greatest one being the way he conducts his own life. Thank you Pops!

I would like to thank my mother Mrs. Thangam venkatesan for her unconditional love and support. She has stood by me like a rock through some of the toughest moments in my life. Her many prayers and blessings has made me into the man I am today. I thank my parents for inculcating their values in me and for bringing me up as a better human being.

I would like to thank my mother-in-law Mrs. Sampoornam jayabal for her love, blessings and prayers. And finally, I would like to thank my dearest wife, Yamini jayabal, for her love, friendship and support in my life. She is my lucky charm and has been extremely patient and understanding throughout my PhD.

I am thankful to God for blessing me with my beautiful family.

November 26, 2018

ABSTRACT

The increased use of smart devices and great strides in fabrication technologies have resulted in densely packed electronics. Combined with 3D packaging, high heat fluxes have become the norm. The need for advanced thermal management solutions has risen. Most devices based on their load profile and architecture are susceptible to non-uniformities in heat fluxes. These non-uniformities with very high heat fluxes are known as hotspots. Mitigation of hotspots is very important for the normal functioning and long term reliability of microprocessors.

Multiple attempts have been made at developing microscale thermal solutions. Most prominent among them are microchannels and heat pipes. The shrinking size of electronics demands compact thermal solutions. One of them is electrowetting on dielectric (EWOD) digital microfluidics. They are highly suitable due to their unique features such as no moving mechanical parts, low power consumption and pump-less operation. Moreover, unlike microchannels, they are immune to flow instabilities.

This research focuses on utilizing EWOD devices to cool hotspots evaporatively. Indium tin oxide (ITO) as well as nickel thin film resistors are integrated in the devices to simulate hotspots as well as make temperature measurements. The experiments were carried out in ambient conditions. Cooling of the hotspot is studied by measuring the hotspot temperature with different heat fluxes and water droplet delivery speeds. Heat fluxes higher than 40 W/cm^2 resulted in enhanced cooling due to phase change happening at the advancing and receding menisci of droplets. Sustained droplet motion cools and maintains the hotspot temperature.

Phase change phenomena although present at high heat fluxes, was not the main mode of heat transfer. To increase the role of evaporation, a superhydrophilic area was integrated in the electrowetting device. The superhydrophilic region, owing to its near zero contact angle, increases the length of the transition region in the thin film[1]. Visuals of spreading of the liquid thin film synchronized with the hotspot temperature data was used to study evaporative hotspot cooling. Different spreading regimes were observed corresponding to various heat transfer modes governing heat dissipation.Also, a thermal resistance analysis was conducted to understand the heat transfer mechanism. The effect of various evaporation parameters was studied.

The work focuses on studying evaporative heat transfer in hotspot cooling. While doing so, it also elucidates the challenges faced in designing a purely evaporative hotspot cooling solution.

TABLE OF CONTENTS

ACKNOWLEDGEMENTS iv

ABSTRACT vi

LIST OF ILLUSTRATIONS xi

Chapter Page

1. INTRODUCTION 1

2. HOTSPOT MITIGATION USING ELECTROWETTING 9

   2.1 Requirements 10

   2.2 Principles of electrowetting 11

   2.3 Types of EWOD 12

   2.4 Microfluidic functions 14

      2.4.1 Droplet generation 14

      2.4.2 Droplet transport 17

   2.5 Electrowetting based cooling 18

   2.6 Conclusions 19

3. STUDY I - HOTSPOT COOLING USING HIGH SPEED DROPLET MOTION 21

   3.1 Motivation and objectives 21

   3.2 Design 22

      3.2.1 Device structure 22

      3.2.2 Material selection 26

   3.3 RTD calibration 27

   3.4 Fabrication 28

   3.5 Experiment 33

3.5.1 Setup and methodology 33
3.6 Results and discussions 37
3.6.1 Anatomy of hotspot cooling curve 38
3.6.2 Continuous/sustained droplet motion 39
3.6.3 Variation of heat flux 40
3.6.4 Effect of inter-droplet delay 41
3.6.5 Effect of switching time 41
3.6.6 Thermal circuit analysis 42
3.7 Conclusions 44
4. STUDY II - HOTSPOT COOLING USING THIN FILM EVAPORATION 46
4.1 Thin film evaporation 47
4.2 Literature review 50
4.3 Design 56
4.3.1 Device structure 56
4.3.2 Material selection 60
4.4 RTD calibration 62
4.5 Fabrication 62
4.5.1 Cleanroom fabrication 63
4.5.2 Electrophoretic deposition 66
4.6 Experiment 67
4.6.1 Setup and methodology 67
4.7 Droplet spreading over superhydrophilic area 71
4.8 Results 72
4.8.1 Spreading phase 72
4.8.2 Thin film phase 75
4.8.3 Dryout phase 76

4.9 Discussion 77
4.9.1 Thermal circuit analysis - baseline 77
4.9.2 Thermal circuit analysis considering thin film evaporation . . 80
4.9.3 Comparison with Study I 86
4.10 Conclusions 87
5. CONCLUSIONS 89
6. FUTURE WORK 91
REFERENCES 93

LIST OF ILLUSTRATIONS

Figure | Page

1.1 Power dissipation trends in chips[3] 2

1.2 Liquid cooling using embedded microchannels[7] 3

1.3 Synthetic microjet over chip (left). Junction to ambient thermal resistance of microjet cooling comparable to cooling with heat sink with natural convection[9] 4

1.4 Integration of thermoelectric cooler with heatsink[10] 5

1.5 Use of mutliple jets for jet impingement cooling[11] 6

1.6 Electroosmotic cooling device containing two chambers separated by a sintered glass frit[14] 7

1.7 Schematic of an electrocapillary pump[15] 7

1.8 Electrowetting on dielectric (EWOD) with a hydrophilic hotspot[16] . 8

2.1 Electrowetting on dielectric. (a) Surface tension forces acting on a droplet resting on a hydrophobic surface. (b) Reversible electrowetting 11

2.2 Difference between (a) parallel plate and (b) open plate electrowetting configuration[22] 13

2.3 Droplet cutting: creation of neck to generate droplets from reservoir[20] 15

2.4 L-junction droplet generation scheme 16

2.5 Difference in actuation and deformation in (a)Square and (b)Slender electrodes[26] 17

2.6 Hotspot cooling using electrowetting 18

3.1 Device design for high speed droplet cooling. 23

3.2 Ground (top) chip design with embedded thin film resistor 24
3.3 (a) Front and (b) back of ITO ground (top) chip with embedded ITO RTD 25
3.4 Material selection: EWOD stack in parallel plate configuration 26
3.5 Calibration curve for ITO RTD 28
3.6 Photolithography process for EWOD (bottom) and ground (top) chips 29
3.7 UV photolithography exposure characterization for Chromium coated glass substrates 30
3.8 (a)Individual setup elements to assemble EWOD (b) Lexan pieces assembled with PCB (c) Close up view of ground (top) chip attached to EWOD device before placing PCB 34
3.9 Schematic showing basic elements needed to operate EWOD 35
3.10 Pictures of EWOD setup. Syringe pump used for pumping liquid into the system (inset) 36
3.11 Electrowetting and heat transfer parameters 37
3.12 Anatomy of a transient cooling curve for electrowetting based hotspot cooling. Heat flux = 60 W/cm^2, switching time = 50 ms, inter-droplet delay = 250 ms, operating voltage = 150 ACV at 1 kHz 38
3.13 Hotspot temperature vs time for different heat fluxes 20, 40, 60 W/cm^2. Switching time = 50 ms, inter-droplet delay = 250 ms, operating voltage = 150 ACV at 1 kHz 40
3.14 Visible condensation for droplet moving over the hotspot at high heat flux (60 W/cm^2). Switching time = 50 ms, inter-droplet delay = 250 ms, operating voltage = 150 ACV at 1 kHz. Detailed video available at [link] 41

3.15 Hotspot temperature vs time for varying inter-droplet delay and constant switching time. Heat flux = 60 W/cm^2, switching time = 50 ms, operating voltage = 150 ACV at 1 kHz 42
3.16 Hotspot temperature vs time for different switching times and constant inter-droplet delay. Heat flux = 60 W/cm^2, inter-droplet delay = 500 ms, operating voltage = 150 ACV at 1 kHz 43
3.17 Thermal resistance circuit for EWOD cooling 44
4.1 Anatomy of a perfectly wetting fluid. Variation of adhesion force, interface curvature and thermal resistance along the three regions [34] 49
4.2 Nanostructured Copper oxide attached to heater chip (left) [38].Vapor chamber heat spreader lined with carbon nanotubes/nanowicks [37] . . 51
4.3 Capillary confinement using nanoporous membrane (left) [40].Micro-XCT image showing micromembrane composed of copper mesh [39] 52
4.4 Hydrophilic hotspot implemented in open EWOD configuration (left)[42]. Copper mesh hydrophilic hotspot implemented in a hybrid open-sandwiched configuration [41] 53
4.5 Jumping drop vapor chamber [44] 54
4.6 Passive liquid transport using nanoporous membrane [45] 55
4.7 EWOD (top) chip design 57
4.8 Ground chip (bottom) design before dicing 59
4.9 Ground chip (bottom) design for two EWOD device halves 59
4.10 Material selection: EWOD stack in parallel plate configuration 60
4.11 Calibration curve for Nickel RTD 62
4.12 Photolithography process for EWOD (top) chip 63
4.13 Photolithography process for ground (bottom) chip 64
4.14 Electrophoretic deposition of alumina nanoparticles [47] 67

4.15 (a) Various elements of EWOD setup Lexan pieces assembled with PCB: (b) Front side (c) Back side 69
4.16 Pictures of EWOD setup. EWOD inverted and mounted on a stand with superhydrophilic area facing up 70
4.17 (a) Schematic of droplet spreading in superhydrophilic area (b) Photograph of sandwiched droplet spreading in superhydrophilic area 71
4.18 Hotspot temperature variation during the entire experiment. Images show various stages of liquid film propagation.Heat flux = 110 W/cm^2, inter-droplet delay = 5s, switching time = 500 ms, operating voltage = 150 ACV at 1 kHz 73
4.19 Hotspot temperature and extent of spreading. Heat flux = 110 W/cm^2, inter-droplet delay = 5s, switching time = 500 ms, operating voltage = 150 ACV at 1 kHz 74
4.20 Hotspot temperature and receding of liquid film. Heat flux = 110 W/cm^2, inter-droplet delay = 5s, switching time = 500 ms, operating voltage = 150 ACV at 1 kHz 75
4.21 Hotspot temperature and dryout of liquid film over hotspot. Heat flux = 110 W/cm^2, inter-droplet delay = 5s, switching time = 500 ms, operating voltage = 150 ACV at 1 kHz 77
4.22 Approximation of rectangular substrate as equivalent circular model . 78
4.23 (a)Thermal resistance network with evaporation(b) Critical parameters varied to analyse heat dissipation 81
4.24 Variation of hotspot temperature with evaporation heat transfer coefficient, h_{evap}. Inset shows zoomed in view of plot 84
4.25 Variation of hotspot temperature with thin film area 85

4.26 (a)Variation of hotspot temperature with thin film distance from hotspot (b) Variation of surface conduction thermal resistance with thin film distance from hotspot 85
4.27 Comparison of percentage of convection and evaporation in Studies I and II 86

CHAPTER 1

INTRODUCTION

The age of electronics has brought about comfort and ease of living to the average consumer. The prevalence of smart devices has mandated the inclusion of microprocessors in almost every device man can think of. The ubiquitousness of microprocessors gives rise to a new set of problems. Microprocessors at the core are collection of various logic gates formed with the help of transistors. It is a well known fact that transistors dissipate heat owing to the joule heating produced by the leakage current [2].

At the inception of the transistor based microprocessors, the heat generated was insignificant. As a result, thermal design considerations were always an afterthought until recently. Microprocessors have since grown in terms of complexity and transistor density due to huge strides made in the field of micro/nano fabrication. Transistor density has increased at a brisk rate empirically by Moore's law. Logically, an improvement on the fabrication side would lend itself to increased efficiency of the transistor. However, the reduced transistor size encouraged higher transistor density and die sizes. This coupled with stacking of integrated circuits (ICs) in system on a chip (SoC) type devices have compounded the problem of heat dissipation. Figure 1.1 depicts the power dissipation trends over the last 48 years.

Over the years, the steady rise in overall heat dissipation has been mitigated by air cooling. The increased complexity and hence high thermal resistance throughout

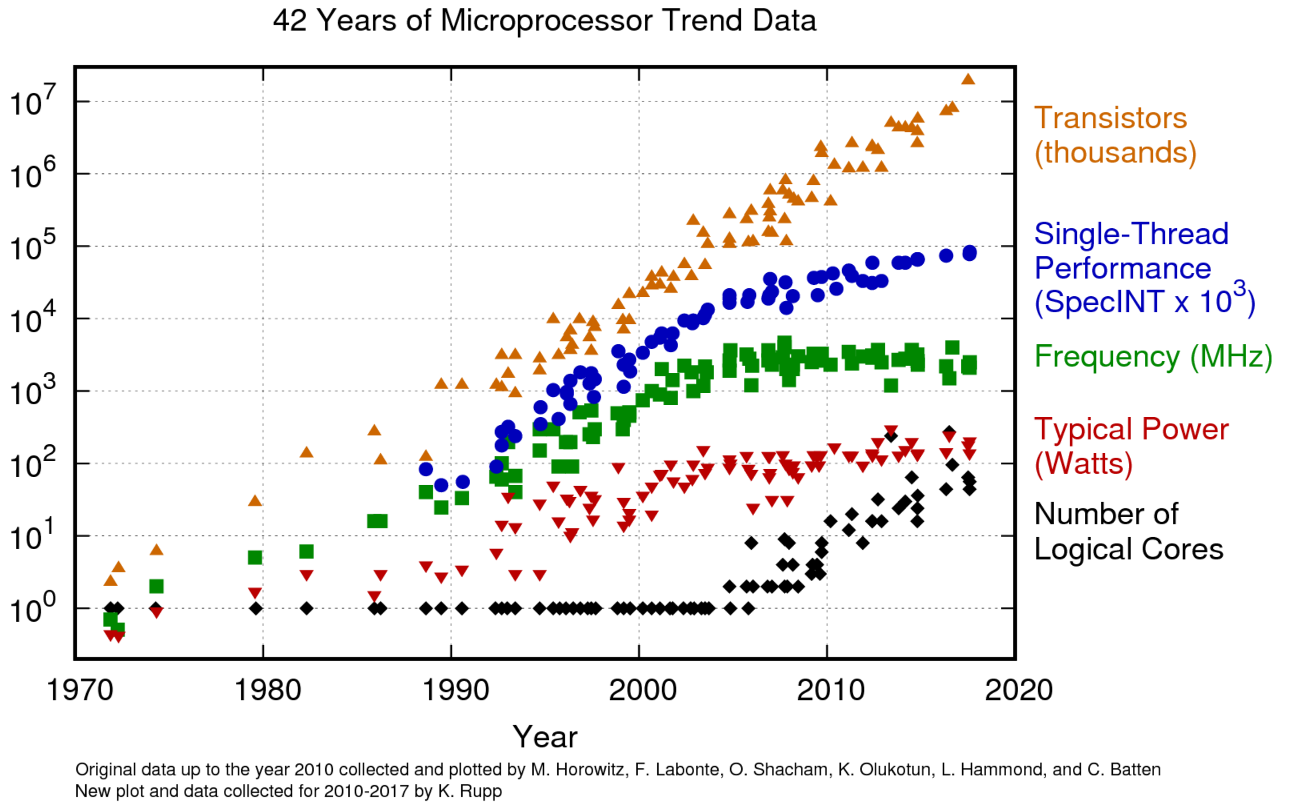

Figure 1.1. Power dissipation trends in chips[3].

the chip has resulted in non-uniformities in the thermal profile. These non-uniformities when highly localized, result in hotspots with very high heat fluxes of the order of 1 kW/cm^2 [4]. These hotspots threaten normal functioning of the microprocessor and affect long term reliability. Conventional air cooling supplemented with commercially available liquid cooling are maintaining the status quo as of now. The increasing complexity, mobility and prevalence of smart devices is forcing a rethink of cooling mitigation technologies.

As mentioned earlier, air cooling has been widely used in various computing sectors. Air cooling consists of mounting a finned heat sink on top of the chip package. A fan is attached to the heat sink to dissipate heat. This technology is unchanged

with minor improvements. Unlike air cooling, which is active, passive cooling methods such as natural convection, heat pipes [5], thermosyphon pumps [6], thermal pastes (conduction) and radiation have also been developed. These methods are cheap and easy to implement but they cannot compare with active cooling in performance terms.

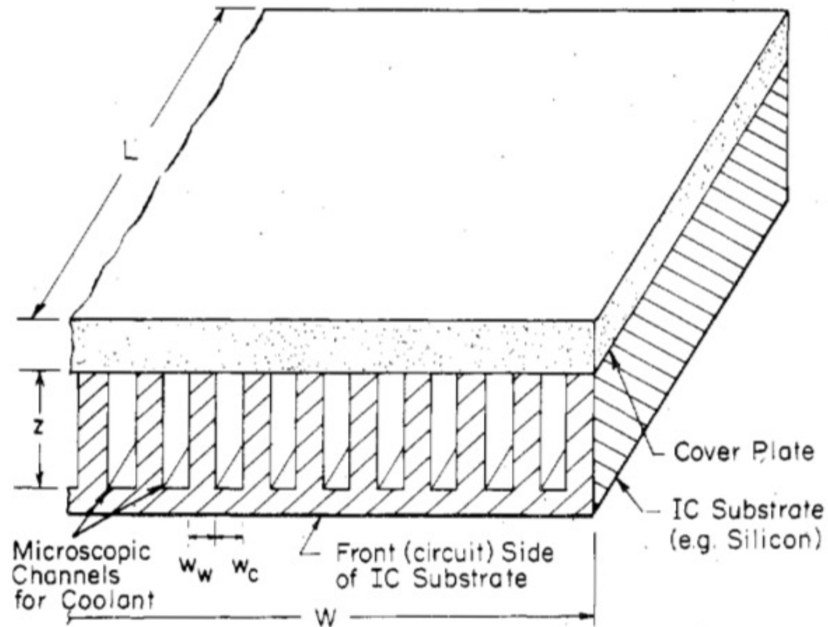

Figure 1.2. Liquid cooling using embedded microchannels[7].

Active cooling requires the supply of power in the form of pumps, fans and refrigeration devices. Air cooling is primarily limited by the specific heat of air and hence would require a large mass flow rate for high heat fluxes. To offset this, liquid cooling became a viable alternative. Due to it's high specific heat, it can operate at low flow rates resulting in compact systems for high heat flux cases. Furthermore, integrating the cooling system closer to chip results in low thermal resistances. Tuckerman and Pease in 1981 [7], demonstrated liquid cooling using

microchannels embedded in the silicon substrate as shown in Figure 1.2. Owing to very low thermal resistance of 0.09 °C/W, they were able to dissipate up to 790 W/cm^2. Microchannel cooling although effective, involves high pumping requirements. Liquid cooling has been implemented on the macroscale in the form of immersion cooling [8]. The heat transfer modes consist of convection (natural/forced) and boiling. Forced convection is very effective in removing heat but requires large pumps and tubing.

Micro-electro-mechanical systems (MEMS) based solutions have also been researched

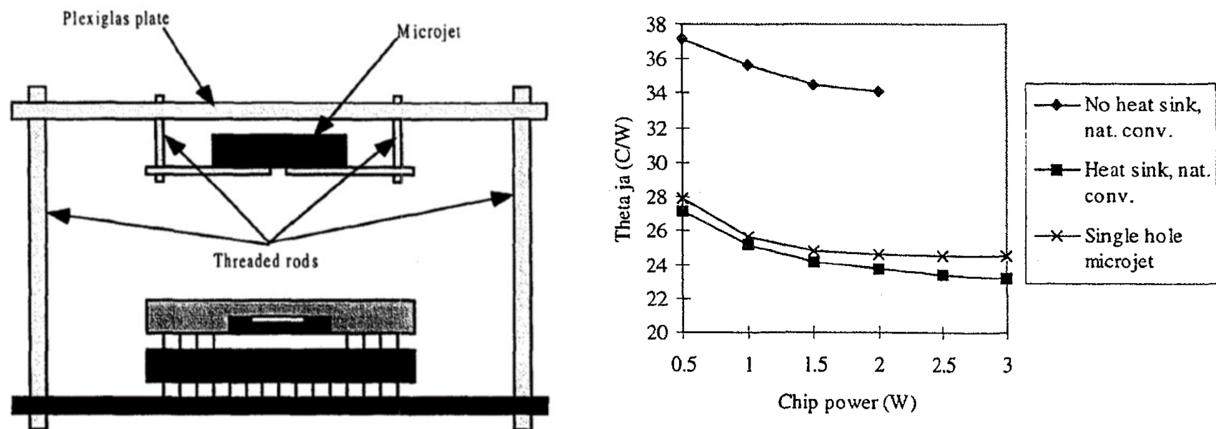

Figure 1.3. Synthetic microjet over chip (left). Junction to ambient thermal resistance of microjet cooling comparable to cooling with heat sink with natural convection[9].

owing to the advancements in microfabrication. An application of this includes air-impinging jet heat exchangers [9]. This works on the principle of injecting air to create special flow patterns which can enhance heat transfer hydrodynamically as shown in Figure 1.3. Refrigeration systems can substantially cool the chip with low thermal resistances but are very bulky compared to other systems. Researchers have used thermoelectric coolers instead [10]. Figure 1.4 shows the schematic of a thermoelectric cooler integrated with a heat sink. Thermoelectric coolers make use

of the Peltier effect. The coefficient of performance of such devices are on the lower side which is a detriment for implementation.

Thermoelectric coolers owing to their working principle, need to have the hot junction

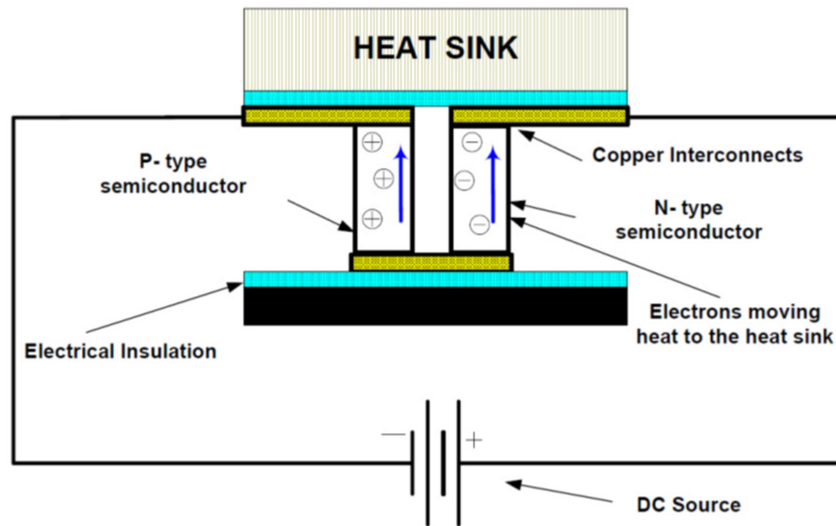

Figure 1.4. Integration of thermoelectric cooler with heatsink[10].

exposed to a heat sink for effectiveness. The hot junction can also infuse heat back into the system and thus influence the cold side.

Kandlikar and Bapat [11] have investigated jet impingement and spray cooling. These are fraught with high pressures, complex fluidic connections and generally require a big setup. Spray cooling uses a combination of conduction and evaporation as its heat transfer mechanism. Another major avenue of research is the use of flow boiling in microchannels [12]. In addition to the high pressure requirements, as in the case of two phase flow, flow instabilities and low critical heat fluxes make this challenging to implement.

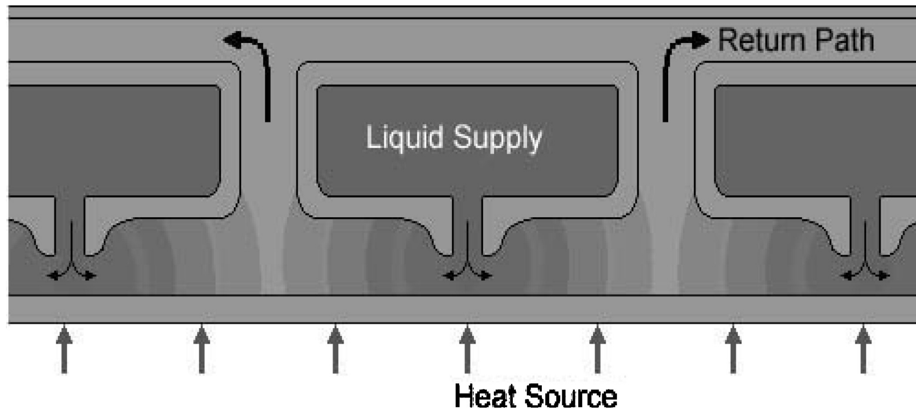

Figure 1.5. Use of mutliple jets for jet impingement cooling[11].

Microfluidic cooling pumps small volumes of coolants over the chip surface to remove heat. Improvements in microfabrication have allowed for design of complex microfluidic devices. Microchannel heat sinks are a major application of this technology. With hydraulic diameters in the micron range [13], it promotes high surface to volume ratio for the coolant. As previously mentioned, the high pressure drops and bulky setup makes it unsuitable for application in highly mobile and compact devices as well.

Jiang et al. implemented electroosmotic pumps in a closed-loop cooling system as a IC thermal management solution[14]. These pumps make use of electroosmosis to deliver coolant without any moving parts. Also, this works in conjunction with a microchannel heat sinks because of their small footprint. This setup was able to remove 38 W from a 1 cm^2 chip while maintaining its temperature at 100°C. Figure 1.6 shows schematic and actual pump.
Another microfluidic cooling method is a MEMS based micro capillary pump by Pettigrew et al. [15]. The use of photolithography is beneficial as it will allow for easy integration in ICs. The pump behaves like a planar heat pipe with an evaporator

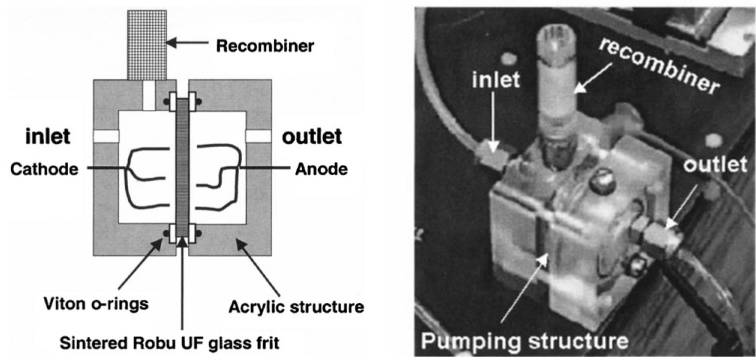

Figure 1.6. Electroosmotic cooling device containing two chambers separated by a sintered glass frit[14].

and condenser as shown in Figure 1.7. The evaporator is composed of deep channels etched into a silicon wafer. This is covered by a glass wafer containing the wicking structure which aids evaporation. These two wafers are anodically bonded to seal the cooling fluid. The device was able to induce cooling of 7 degrees on the backside of the wafer heated using a 7.5 W laser.

Recently, electrowetting on dielectric, a concept utilized for lab on a chip applications

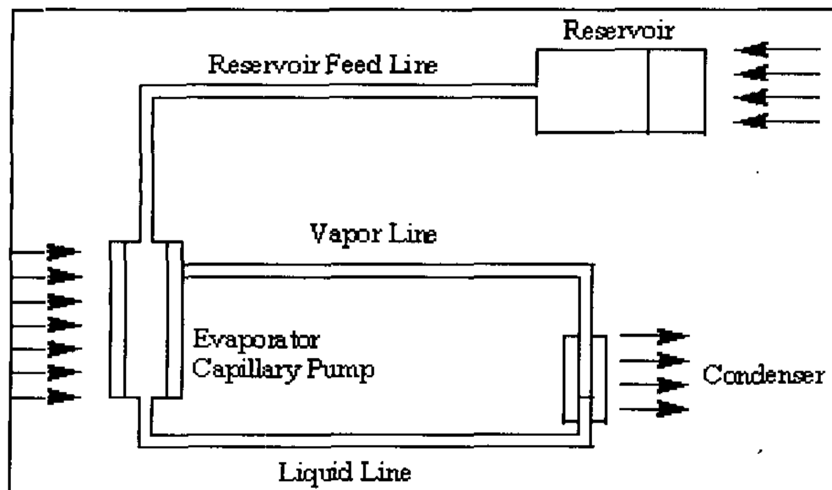

Figure 1.7. Schematic of an electrocapillary pump[15].

is gaining popularity for thermal management of ICs. It involves manipulating individual droplets of coolant to induce cooling in a target area. Bindiganevale and Moon implemented electrowetting by sandwiching a droplet between two plates to cool a simulated hotspot as shown in Figure 1.8. A heat flux of upto 36.6 W/cm^2 was cooled using a hydrophilic area integrated in the device.

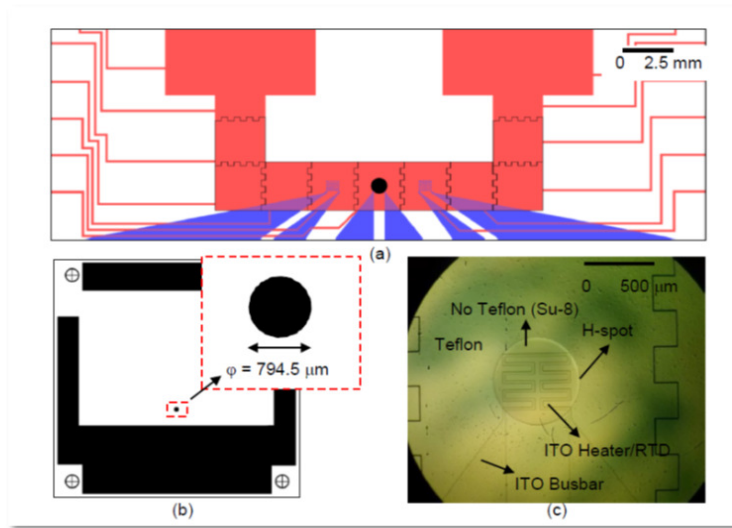

Figure 1.8. Electrowetting on dielectric (EWOD) with a hydrophilic hotspot[16].

CHAPTER 2

HOTSPOT MITIGATION USING ELECTROWETTING

Hamann et al.[17] demonstrated the prevalence of hotspots by studying the infrared thermal image of a consumer grade microprocessor during boot-up. Hotspots have been known to affect both performance and reliability of the IC. It is essential that hotspot mitigation be taken seriously as these processors are increasingly being used in handheld devices which combined with lithium-ion batteries could pose a significant threat to life.

Despite the high heat dissipation afforded by current cooling solutions, they require elaborate setups to function. Staying in line with the current trend of miniaturization of computing devices, the cooling solutions need to be compact. Hence, microfluidic devices are being considered for use in ICs. At the same time, phase change heat transfer can provide high heat flux dissipation. As seen in the previous chapter, phase change in microchannels has been studied but owing to flow instabilities and high pumping requirements, are not suitable for embedded cooling. Solid state cooling using thin film thermoelectrics have been considered but are incapable of dissipating high heat fluxes.

In this chapter, the requirements of an ideal cooling system will be presented and the use of electrowetting on dielectric hereafter, referred to as EWOD would be proposed. It is the discretized flow of liquid by using the principle of electrowetting.

2.1 Requirements

There are several shortcomings in the cooling methods covered so far. An ideal cooling system should fulfill the following requirements:

- The system must be compact and easy to integrate with the IC
- The fabrication process flow should be compatible with that of ICs
- Low power consumption
- Closed loop operation
- Individually address hotspots occuring during different loading conditions
- Make use of phase change heat transfer

Majority of the traditional cooling methods are either have a large footprint and/or only provide bulk cooling. For example, fan cooling can tackle the overall heat dissipated by the processor but does nothing to address hotspots. Moreover, microchannels, in addition to not being able to tackle hotspots require a high pressure to operate. This necessitates extensive plumbing and a bulky power hungry pump. The methods covered in chapter 1 are unsuited for addressing individual hotspots and impractical for embedding in modern ICs.

To scale down power consumption and footprint, microfluidic cooling is preferred as it can be integrated with ICs. However, a different approach to microfluidic cooling needs to be taken to consider the individual hotspot addressing requirement. Electrowetting is a legitimate option which can send discretized droplets to the target area. Also, being electrically driven, the droplet movement is highly programmable which allows for customizing the droplet delivery for different thermal loads. Finally, EWOD also consumes less operational power compared to conventional methods.

2.2 Principles of electrowetting

Electrocapillary effect or electrowetting was discovered by Lippmann [18] in 1875. The idea of using dielectric films on top of electrodes was introduced by Berge [19] in 1993. This forms the basis for modern electrowetting devices.

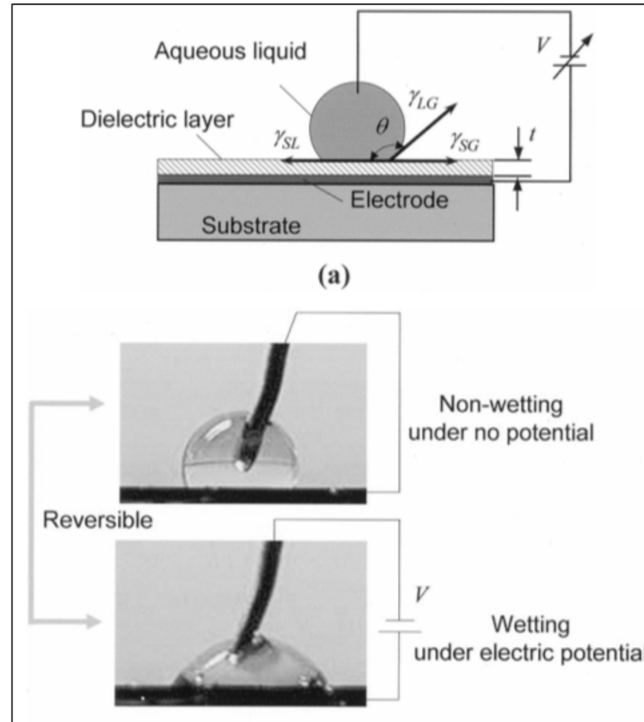

Figure 2.1. Electrowetting on dielectric. (a) Surface tension forces acting on a droplet resting on a hydrophobic surface. (b) Reversible electrowetting. [20]

On application of electric voltage, electric charge accumulates on the dielectric surface which changes the surface energy as shown in Figure 2.1. This produces a change in wettability of the liquid droplet. This phenomena is highly reversible and is governed by the Lippmann equation[18]:

$$\gamma_{SL} = \gamma_{SL}|_{V=0} - \frac{1}{2}CV^2 \tag{2.1}$$

where γ is the surface tension, V is the electric voltage across the interface and C is the capacitance of the dielectric. The relationship between contact angle and surface tension was given by Young-Dupre [21]:

$$cos\theta = \frac{\gamma_{SG} - \gamma_{SL}}{\gamma_{LG}} \tag{2.2}$$

The two equations combine to form the Lippmann-Young equation which gives the relationship between contact angle change and electric voltage[20]:

$$cos\theta_V - cos\theta_0 = \frac{\epsilon_0\epsilon}{2\gamma_{LG}t}V^2 \tag{2.3}$$

where θ_0 is the equilibrium contact angle at V=0, ϵ is the dielectric constant of the dielectric layer, ϵ_0 is the permittivity of free space and t is the thickness of the dielectric.

2.3 Types of EWOD

Based on the previous section, EWOD requires certain basic elements for it to function. The major elements include:

- Electrodes (both positive and negative), to apply electric field to the drop
- Dielectric layer, to insulate the drop from electric current to prevent electrolysis
- Hydrophobic layer, to facilitate the change of contact angle on application of electric field

These elements can be implemented in two different configurations: (i) Open plate (ii) Parallel-plate. Figure 2.2 shows the basic elements of EWOD in these two configurations. The main difference between the two is the integration of the ground

electrode on the same plane in the case of open-plate configuration. Thus, the electric field on the droplet is applied by these co-planar electrodes which manipulate the drop in a sessile mode. On the other hand, the droplet is sandwiched between the two

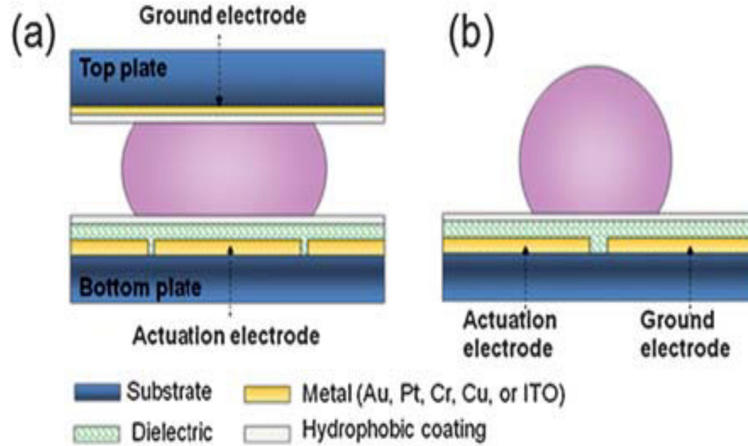

Figure 2.2. Difference between (a) parallel plate and (b) open plate electrowetting configuration[22].

plates in the parallel plate configuration. One plate contains the positive electrodes, dielectric layer and hydrophobic layer. The ground is provided by means of the 2nd plate which is a large electrode with a hydrophobic layer connected to ground. Both configurations have their own advantages and disadvantages.

The main advantage of open plate operation is there is less friction owing to the absence of another plate in contact with the droplet. However, in the parallel-plate case, this higher friction can be handled by supplying a higher voltage which results in a higher electrowetting force. On the other hand, open plate configuration has issues with cutting large droplets into small ones. This is not an issue with parallel-plate configuration. Finally, open-plate configuration is not practical for integrating with ICs for hotspot cooling to prevent coolant leakage.

Hence, for hotspot cooling purpose, parallel plate configuration is preferred. The droplet is sandwiched between the two plates which are maintained at a specific gap. The height of this gap plays a crucial role in droplet motion behavior.

2.4 Microfluidic functions

Cho et al.[20] talks about various microfluidic functions possible in a parallel plate configuration. Out of which, we are interested in droplet generation and transport. Generation refers to cutting a droplet of manageable size from a reservoir. These small packets of liquid could then be used for various purposes whether it be for cooling, merging with other droplets to form new products or separate to remove chemicals.

Hence, to use the full potential of EWOD, droplet generation is necessary. In case of hotspot cooling, these small liquid packets are used to cool the hotspot. The generation of droplets forms a major bottleneck in the operation speed of the device to cater to the cooling of the hotspot. Therefore, it is vital to understand the droplet generation process and what methods are available to reduce this bottleneck.

Once these droplets are generated, they are transported over the hotspot to induce cooling. The frequency and velocity of these droplets should be high enough to be able to mitigate the hotspot. Hence, high speed droplet generation and transport is essential for electrowetting to compete with other microfluidic technologies.

2.4.1 Droplet generation

The most logical way is to pull the droplet in two opposite directions by wetting electrodes on opposite ends as demonstrated by Cho et al.[20]. Figure 2.3 shows the droplet cutting and merging process. By slowly dewetting in the middle, a neck is created to preserve the total volume of the droplet. The pinching of the droplet in

the nonwetting region helps to cut the droplet into two. Based on findings from [20], a large droplet and a small gap between the parallel plates results in favorable cutting. Reservoirs are designed to follow this principle to create droplets. The

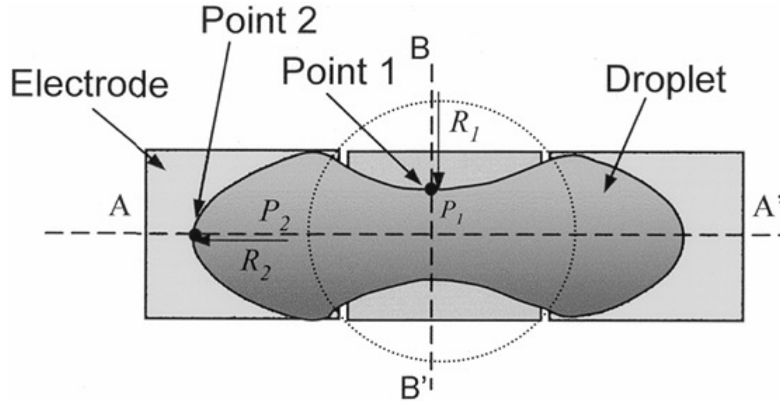

Figure 2.3. Droplet cutting: creation of neck to generate droplets from reservoir[20].

most popular reservoir designs are based on this principle. Electrodes remain ON as long as the electric field is maintained on the electrodes. The time an electrode remains ON is referred to as the switching time. Based on the design, the minimum switching time for various microfluidic functions can vary. The switching times are of the order of milliseconds. The typical time taken for generating droplets using this principleis above 200ms. Moreover, the volume of the generated droplet is inaccurate as the pinch off point for each droplet varies. This creates a tail of varying volumes which could add to the actual droplet volume thus, causing the inaccuracy.

To solve this issue, Nikapitiya and Moon [23] created a droplet generation scheme which improves both generation speed as well as generated droplet volume accuracy. This scheme makes use of two electrodes arranged diagonally instead of longitudinally[24]. This allows for the electrodes to assume a diamond shape and readily form two daughter droplets with little perturbation. This satisfies two critical

conditions: (i) Minimization of tail formation (ii) Formation of pinch off point or neck at the same location. This allows for repeatable accurate droplet generation. This coupled with slender electrodes instead of square electrodes considerably speed up the droplet generation process. The droplet generation now takes between 55-110ms instead of 200ms.

The droplet generation scheme works as follows: (1) Pull out liquid from reservoir and form a column of liquid C_1, (2) Transport liquid along a 90° arc, (3) Activate electrodes along column C_2 while deactivating electrodes along arc. This generation scheme is called L-junction owing to the L formed by the two columns as seen in Figure 2.4. This method of generation creates a diamond formation between the two columns C_1 and C_2 which aids in creating a small repeatable neck at intersection of the two columns.

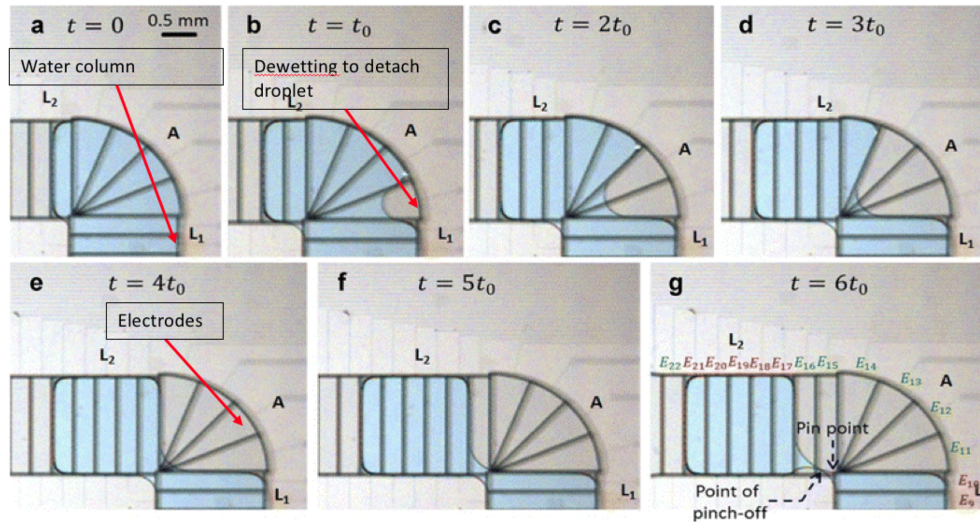

Figure 2.4. L-junction droplet generation scheme.
(a) Column of water formed, (b)-(f) Droplet detached by dewetting electrode in sequence, (g) Neck formation between columns L_1 and L_2 results in generated droplet[24].

2.4.2 Droplet transport

Droplets in EWOD can be manipulated using electric fields. This provides a lot of flexibility and high degree of control over the droplet movement. Droplets are moved over individually addressable electrodes insulated by a dielectric layer. These electrodes are separated by a gap which have an effect on the extent of contact angle change[25]. Based on their findings, a smaller gap favors higher contact angle change. A 10μm gap is chosen based on the findings and fabrication constraints. Traditionally, square electrodes have been used for most applications. In recent times,

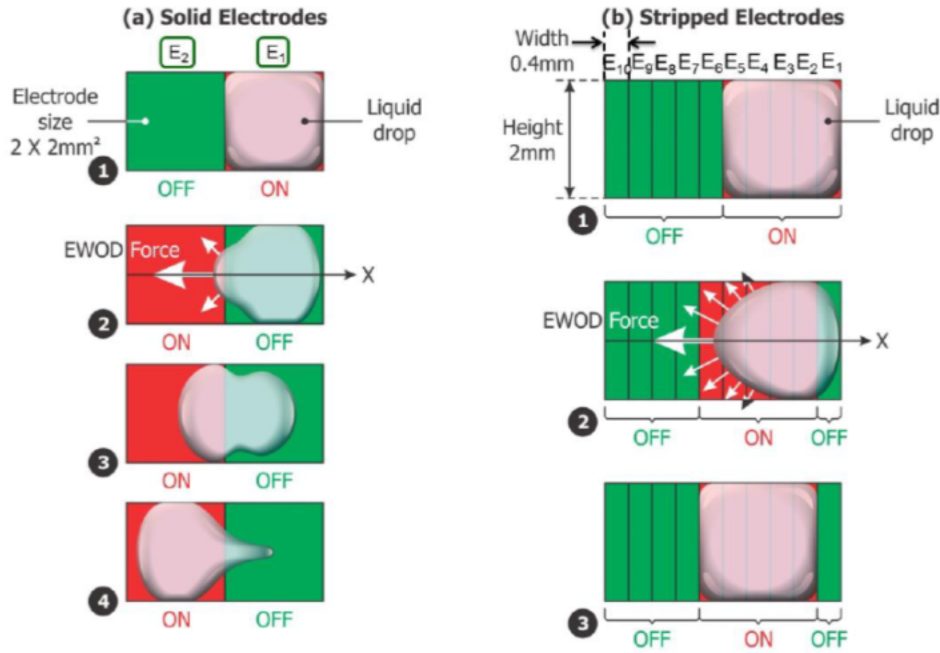

Figure 2.5. Difference in actuation and deformation in (a)Square and (b)Slender electrodes[26].

inter-digitated electrodes have become popular owing to the increased electrode-droplet contact. As mentioned earlier, switching time, time taken by the droplet to activate electrodes, becomes a factor in droplet velocity. Square droplets have high switching

times owing to increased deformation of the droplet when transitioning from one electrode to the other. To counteract this effect, Nikapitiya and Moon[24] suggested the use of slender electrodes which are one-fifth the width of square electrodes. Five of these electrodes could hold a droplet of volume equal to that of one square electrode. This mitigates the deformation problem and improves droplet velocity by reducing the switching time[27]. Figure 2.5 shows the differences between the two electrode designs.

2.5 Electrowetting based cooling

Electrowetting has been widely used for biological applications owing to its low reagent use, high surface to volume ratio and low power requirements [28]. Adapting electrowetting devices for use as a cooling platform requires certain design considerations. First and foremost, parallel plate configuration is more suitable

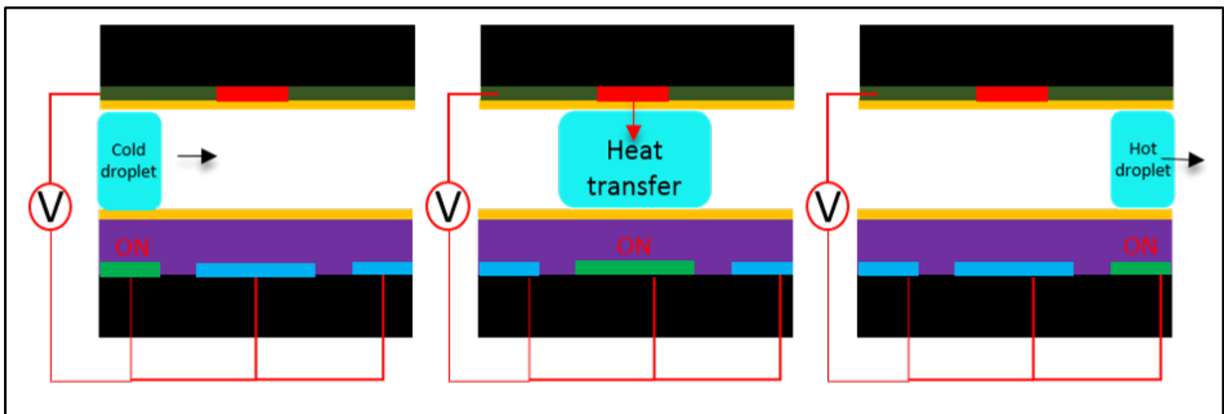

Figure 2.6. Hotspot cooling using electrowetting.

for embedding into an IC as it essentially seals the coolant which is necessary to avoid coolant leakage. Since electrowetting requires electric voltage to be applied to manipulate droplets, it can be easily be fabricated using traditional photolithography

techniques already used for IC fabrication. Figure 2.6 shows a droplet sandwiched between the EWOD chip and the ground plate. To demonstrate hotspot cooling, we need to simulate a hotspot. This can be done using thin film resistors whose resistance is a function of temperature. Their design and use is detailed in the next chapter.

The generation of droplets provides us with independent and precise control over these discrete liquid packets. Individual control affords us the adaptability of cooling as per the thermal load present at the hotspot. Due to the absence of side walls like in the case of microchannels, there is no restriction in the pathways these drops can take to reach the target area. Also, the lack of side walls helps prevent any flow instabilities which can occur during phase change. To orchestrate cooling, drops are generated using L-junction outlined earlier and transported using slender electrodes over the hotspot. Owing to no moving mechanical parts, this pumpless operation could be completed with low power.

As the droplet moves over the hotspot, heat transfer between the drop and heater would be observed and the temperature recorded using thin film resistance temperature detectors (RTDs). The used droplet would continue to another reservoir where it will be removed from the system. There are several works done wherein EWOD has been used to implement hotspot cooling. Cheng and Chen [29] used coplanar EWOD electrodes to handle heat fluxes upto 27W/cm^2. Mohseni proposed the use of liquid alloys to cool hotspots using electrowetting [30]. Liquid metals such as mercury pose a toxicity risk. Coplanar electrodes on the other hand are not suitable for integration with semiconductors due to their open configuration.

2.6 Conclusions

It has been established that the presence of hotspots in ICs is a serious problem affecting long term reliability and performance of the IC. Based on the literature

survey, it was concluded that most cooling methods focus on bulk cooling instead of hotspot cooling. Moreover, the methods are not suitable for integration into an IC owing to their large footprint and/or high power requirements.

Requirements for the ideal cooling system have been listed. These requirements have only been met partially by current cooling methods. Microfluidic cooling, more specifically, EWOD has been identified as a potential hotspot mitigating solution. Electrowetting principles have also been explained in this chapter. Additionally, the basic elements of an EWOD device and configurations have been outlined while highlighting the requisite microfluidic functions. Two important methods for droplet generation and transport have been detailed.

Based on these principles, hotspot cooling using electrowetting has been proposed. This involves designing an electrowetting device having L-junction and slender electrodes along with an embedded thin film heater. This device utilized in a parallel plate configuration would be used to demonstrate hotspot cooling using EWOD. Owing to their flexibility, the cooling could be studied under thermal loads and operating parameters.

CHAPTER 3

STUDY I - HOTSPOT COOLING USING HIGH SPEED DROPLET MOTION

3.1 Motivation and objectives

Due to the many advantages associated with EWOD, there have been many attempts at using EWOD to cool hotspots. Electrowetting phenomena has primarily been used for lab on a chip devices. Utilizing the same technology for hotspot cooling without modification results in slow droplet speeds and dealing with low heat fluxes. Figure 2.6 shows a droplet sandwiched between two parallel plates containing the EWOD and ground electrodes. By actuating electrodes in a consecutive manner five at a time, the droplet is moved from the inlet reservoir to the outlet reservoir. The hotspot is simulated by using a heater embedded in the ground (top) chip. Each droplet spanning five electrodes moves over the hotspot and cools it. This process is repeated by translating multiple droplets over the heater and thus maintaining the hotspot temperature below the initial steady state value. We can control various experimental parameters to reduce the temperature further.

By utlizing this setup, the following are the objectives of study I:

- Demonstrate hotspot cooling using electrowetting. Show pumpless operation of EWOD and leverage it to showcase the ability to sustain a steady stream of droplets at high speed.
- Study the effect of various parameters on cooling performance
- Study the heat transfer mechanism in this cooling methodology.

3.2 Design

In the previous chapter, a paradigm for cooling hotspots using electrowetting was established. It consisted of transporting droplets over a hotspot to produce cooling over the intended target area. To accomplish the aforementioned objectives, the following design requirements for the device need to be met:

- Inject coolant droplets into system
- Transport coolant droplets over hotspot
- Collect used coolant droplets
- Heater to simulate hotspot
- Monitor and record hotspot temperature

3.2.1 Device structure

As already discussed in chapter 2, there are two basic configurations available to implement EWOD namely: (i) Open plate (ii) Parallel-plate configurations. Parallel-plate configuration is preferred as it is more conducive to integrate this design into microprocessors for cooling. This would allow for the coolant to be sealed and prevent any seepage to the underlying systems. Also, generation of droplets is way easier in this configuration.

EWOD in parallel plate configuration requires the use of two plates or chips. The bottom plate is usually the EWOD chip consisting of conductive electrodes coated with dielectric and hydrophobic layers. The top plate, also conductive is coated with a hydrophobic layer completing the circuit. Both the plates are separated by a small gap (100 microns) where the droplet is sandwiched. This way, an electric field is created between the top and bottom plates which can be used to manipulate the droplet and move it along the conductive electrode paths designed on the EWOD (bottom) chip.

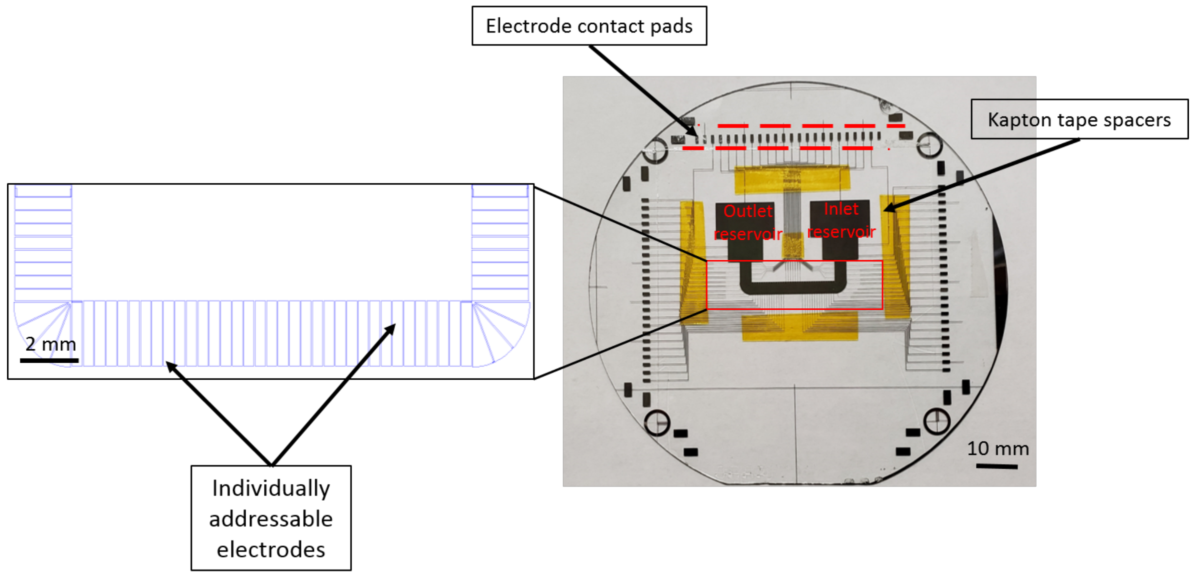

Figure 3.1. Device design for high speed droplet cooling..

Figure 3.1 shows the design of EWOD bottom chip. To transport droplets efficiently over the hotspot, a manageable droplet volume must be generated. As mentioned in chapter 2, it is preferred to use L-junction along with slender electrodes to expedite the generation and delivery of droplets to the hotspot. Sustained droplet delivery is enabled by creating a large reservoir to hold the coolant and supply as needed. Two of these reservoirs have been used and are connected by a path of inter-digitated slender electrodes to facilitate movement of droplets between the two reservoirs. These electrodes owing to their slender design provide for high droplet velocity compared to the conventional square electrode.

One reservoir acts to serve as a tank to hold the coolant and the other collects the used coolant droplets. The droplets can either be moved left to right or vice versa. The dimensions are so chosen that 5 electrodes worth of coolant when sandwiched between the two plates will amount to 0.9 μL. The gap between electrodes is ten microns, which is a limitation imposed by fabrication constraints. Each of electrodes

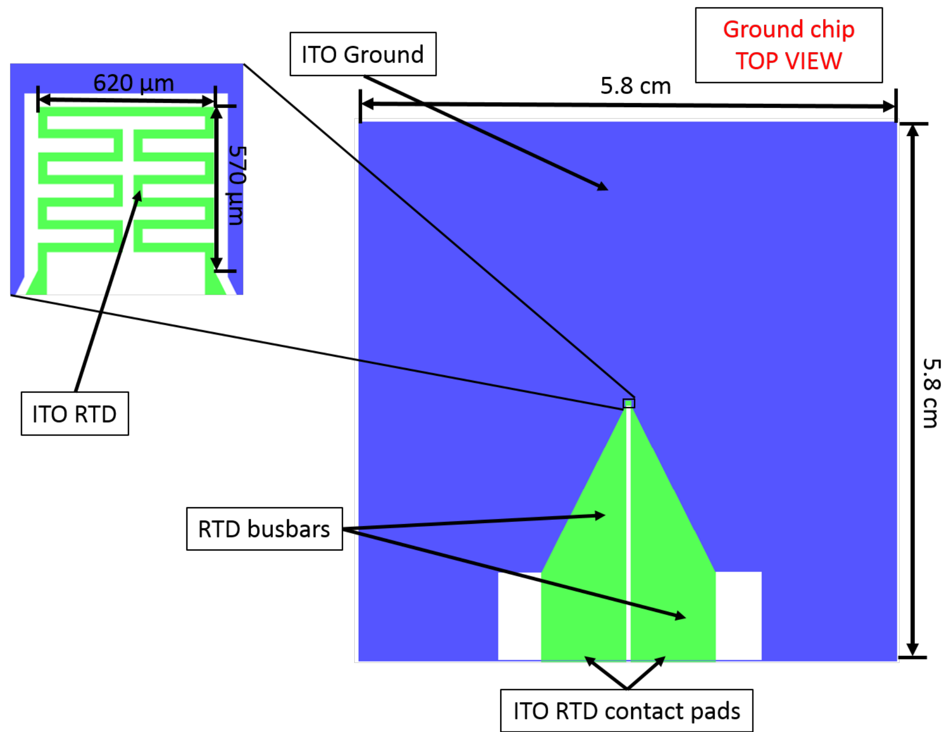

Figure 3.2. Ground (top) chip design with embedded thin film resistor.

are connected by traces to contact pads surrounding the edge of device which will interface to a PCB.

Figure 3.2 depicts the top view of the ground (top) chip. The ground (top) chip is composed of one single electrode and an embedded thin film resistor coated with a hydrophobic layer. The two plates are maintained at a fixed gap of 100 microns using kapton double sided tape as a spacer. Although EWOD would still function at different gaps, this value has been chosen for optimal electrowetting force for cutting and transport. Coolant must be continuously supplied to the reservoir to sustain droplet generation. To accomplish this, two holes have been drilled in the top chip to coincide with the location of the reservoirs when assembled in parallel plate configuration. Furthermore, two pipette tips have been attached to these holes using quick-set epoxy to allow for external fluidic connections. Both pipette tips were

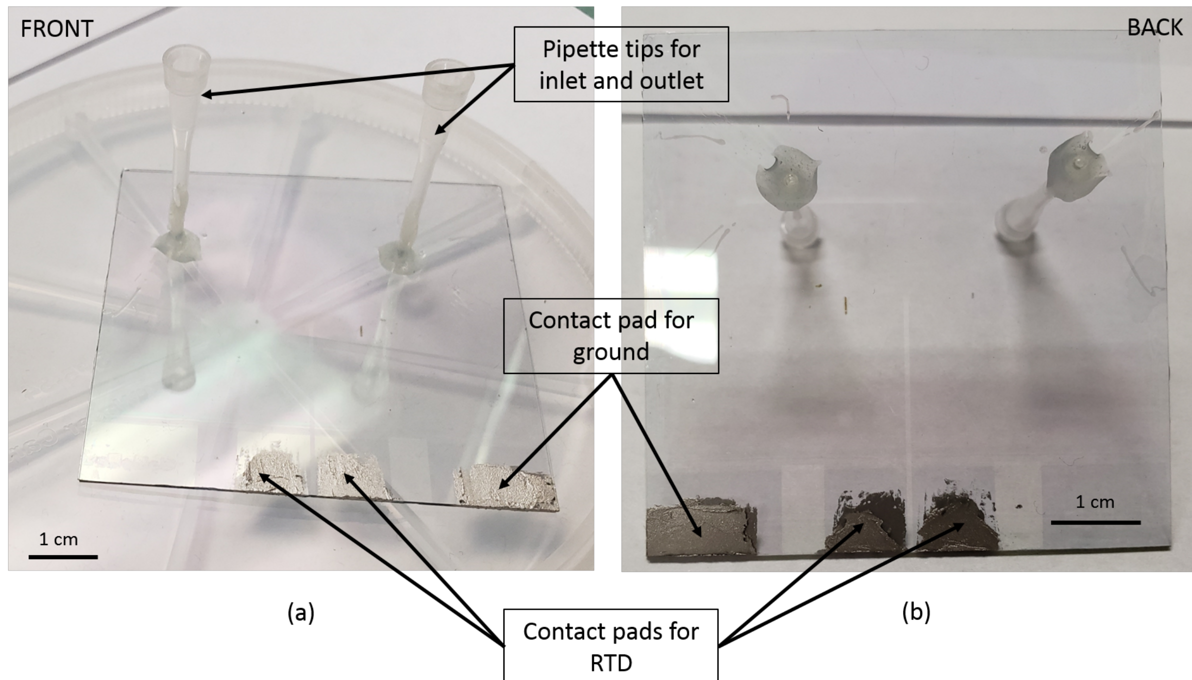

Figure 3.3. (a) Front and (b) back of ITO ground (top) chip with embedded ITO RTD.

connected to syringes using TYGON tubing. One of the syringes was operated by a syringe pump to supply coolant to the generating reservoir.

One of the main requirements of this EWOD (bottom) chip is the ability to simulate a hotspot and monitor hotspot temperature. Thin film RTDs have been used in the past [16] for measuring temperature. Thin film RTDs are compatible with photolithography techniques thus, the perfect choice for measuring temperature in EWOD devices. At the same time, additional current could be supplied to the RTDs to induce joule heating for hotspot simulation. The heater is located in the center of the path connecting the two reservoirs. Figure 3.3 shows the front and back views of an indium tin oxide (ITO) ground (top) chip with an embedded ITO RTD.

There are two ways to integrate an RTD in this EWOD setup: (i) Pattern RTD underneath the electrodes on the bottom chip, or (ii) Pattern RTD on the top

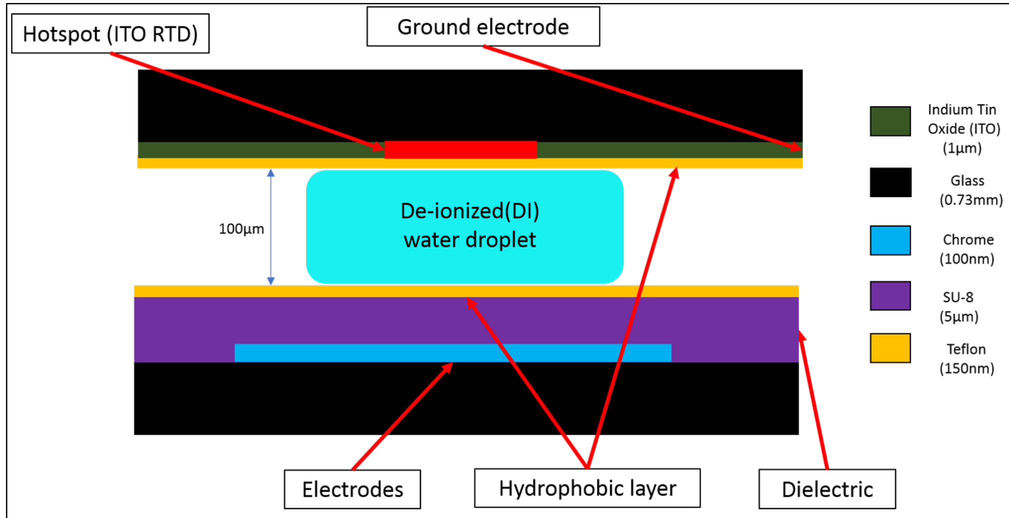

Figure 3.4. Material selection: EWOD stack in parallel plate configuration.

chip. In the first case, the RTD is insulated from the EWOD electrodes with a thick insulation layer. This inhibits the electrowetting performance as the voltage drop occurs on the dielectric below and above the electrodes. Also, the EWOD signal gets coupled with the RTD measurement data which is undesirable. Hence, the second method was preferred owing to the lack of these issues and the ease of fabrication.

3.2.2 Material selection

Figure 3.4 shows the EWOD stack using the material choices detailed here. The bottom chip consists of chromium EWOD electrodes which form the basis of droplet movement. The SU-8 forms the dielectric layer which charges and discharges on application of the underlying electric field. The dielectric layer, mentioned in the chapter 1, stores charges which influences the surface tension force balance of the droplet. The teflon layer provides the hydrophobicity which has a lower surface energy.

A glass substrate was used for the bottom chip instead of silicon due to its low thermal conductivity. The high thermal conductivity of silicon makes it prohibitive to simulate hotspots. All the electrodes were fabricated using chromium due to its low electrical resistance, good adhesion with glass, ease of fabrication and visualization in experiments. SU-8 was chosen as the dielectric due to simplicity of coating and uniformity. Moreover, its dielectric constant is high enough to avoid electrolysis.

The top chip was composed of a glass wafer coated with ITO. This was patterned to form ground and ITO heater/RTD. ITO is known to work as a linear RTD below 150°C [31]. Also, owing to its high resistivity, the heater has a high resistance of 1.1 kΩ which will allow for low current operation. The heater was connected to busbars to reduce the contact resistance with wires coming from the current source. The connection for the ground (top) and RTDs were taken out by applying silver epoxy on the busbar contact pads, wafer thickness side and on top of the wafer. The heater on the top chip is aligned with the center of the bottom chip. Deionized water is used as the coolant of choice owing to its high specific heat, latent heat of vaporization and high mobility on the EWOD platform.

3.3 RTD calibration

As mentioned earlier, ITO was chosen as the RTD/heater due to linear variation of temperature with resistance in the operating range for our experiments. The RTD was calibrated in a motor oil bath placed on a hot plate. The 4-wire resistance of the RTD was measured using a DAQ operated through labVIEW at increasing temperatures (25°C to 125°C) set by the hot plate. Similarly, the same process was repeated for decreasing temperatures from 125°C to 25°C. This procedure has been detailed in [31]. The heating and cooling calibration is done to ensure repeatability as shown in Figure 3.5.

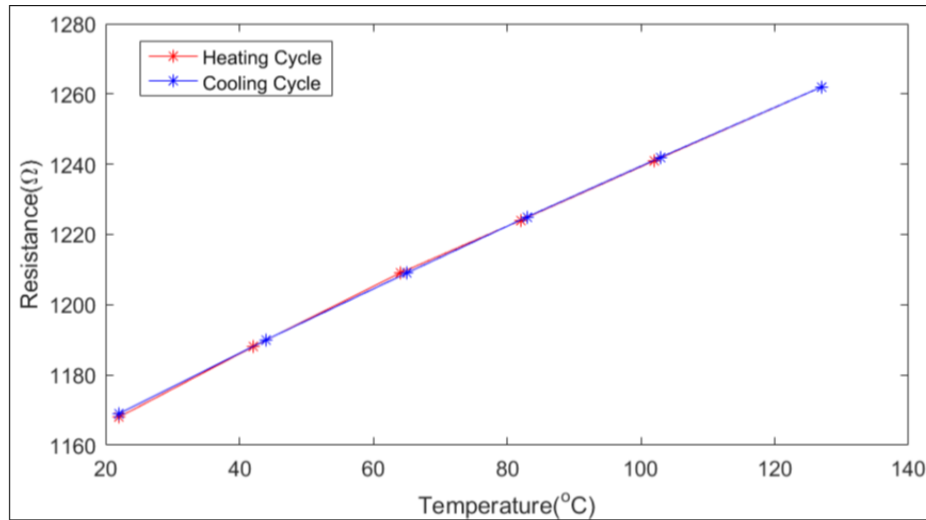

Figure 3.5. Calibration curve for ITO RTD [31].

3.4 Fabrication

Fabrication of the EWOD (bottom) and ground (top) chip was carried out at Shimadzu institute for research technologies, UT Arlington. As mentioned in chapter 1, EWOD devices can be fabricated using photolithography processes in a cleanroom environment. The majority of photolithography data such as bake temperatures, exposure times, bake times etc. are tailored for fabrication using silicon substrates, the fabrication process detailed below has been customized for use with metallized glass substrates.

Figure 3.6 shows the process flow for entire fabrication process for study I. A 0.71 mm thick 100 mm diameter glass wafer was used. The wafer was thoroughly cleaned by rinsing with acetone, isopropyl alcohol (IPA) and methanol. Subsequently, the wafer was agitated in a deionized (DI) water bath for a few seconds, rinsed with DI water and blow dried using nitrogen gas. The dry glass wafer was immersed in a piranha solution (3:1 mixture of 95-98% sulphuric acid with hydrogen peroxide) for 20 minutes as the solution loses strength beyond that time. The wafer was then

immersed and agitated in two consecutive water baths for a few seconds using a plastic tweezer. The wafer was blow dried with nitrogen gas and dehydrated at 230°C for 5 minutes. The high dehydration temperature ensures a clean substrate thus, promoting adhesion of the chromium layer.

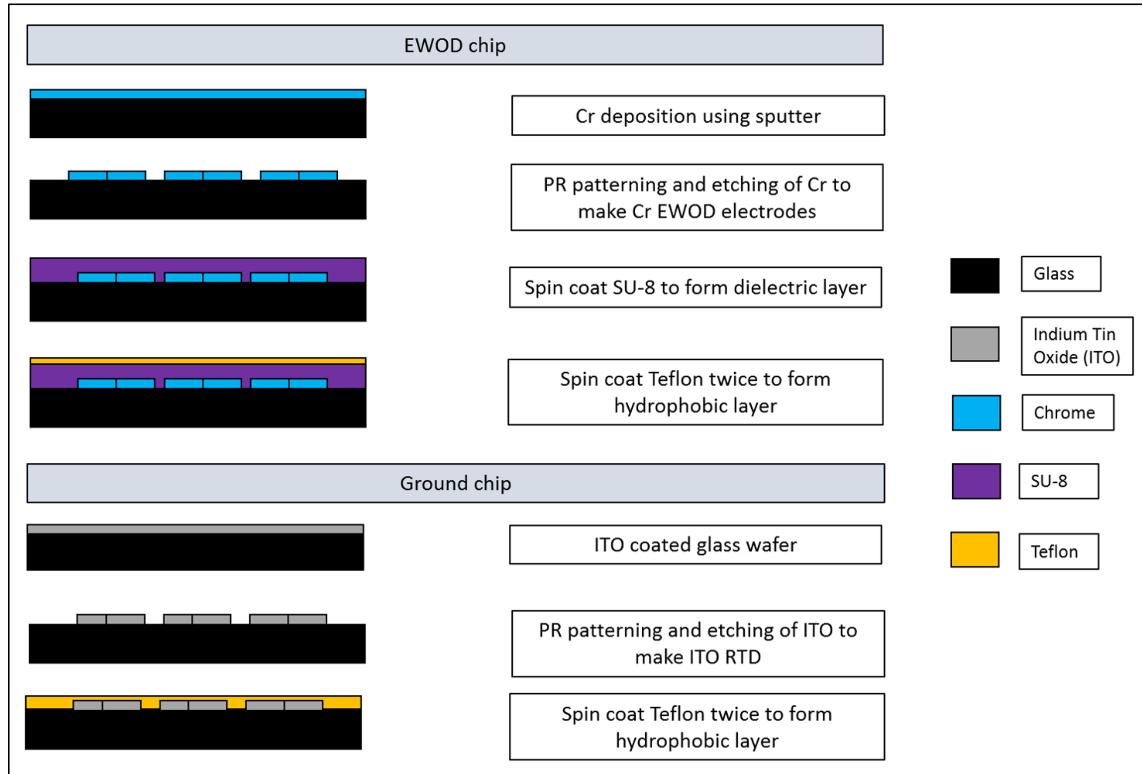

Figure 3.6. Photolithography process for EWOD (bottom) and ground (top) chips.

The cleaned wafer was sputtered for 150 seconds to yield a 100 nm chromium layer. The wafer was again cleaned with acetone, IPA and methanol and rinsed with DI water. The wafer was then dehydrated at 180°C. Hereafter, we begin the photolithography process. The substrate was spin coated with hexamethyldisilazane (HMDS) to form an adhesion layer for the photoresist (PR). The spin coat recipe is shown in Table 3.1. The wafer was baked at 150°C for 2 minutes 15 seconds.

Subsequently, a 1.3 μm thick PR (Microchem S1813 G2) layer was spincoated on the substrate using the spin coat recipe in Table 3.1. The wafer was then baked at 115°C for 1 minute 45 seconds to evaporate the excess solvent and cooled at the cool plate to reabsorb the moisture lost during baking. This moisture is critical to the photolithographic process.

Exposure time	Left			Center			Right		
	Wire thickness	Gap	Exposure level	Wire thickness	Gap	Exposure level	Wire thickness	Gap	Exposure level
14	20.51	23.07		23.07	17.96		17.96	15.41	
8	23.07	12.86		21.79	15.25		21.79	16.69	
5.5	24.45	-		23.07	-		23.18	-	
5.4	24.11	11.14		24.11	10.09		24.11	12.68	
5.3	25.63	10.24		24.34	11.51		24.35	11.59	
5.2	24.01	10.18		24.01	10.09		23.98	11.36	
5	24.01	11.43		24.01	12.62		23.98	12.62	
4.8	25.63	10.32		23.07	12.79		23.07	11.59	
4.8 R	23.07	14.13		20.51	12.79		23.07	14.08	

Optimum feature size:
Wire → 25µm
Gap → 10µm

Highly overexposed
Overexposed
Slightly overexposed
Correct exposure
Highly underexposed
Underexposed
Slightly underexposed

Figure 3.7. UV photolithography exposure characterization for Chromium coated glass substrates.

PR coated wafer was exposed to a 106 mJ/cm^2 dose of broad spectrum UV light on the OAI aligner. As mentioned earlier, most photoresists are characterized for use on silicon wafers. Thus, an exposure characterization was done for Chromium coated glass substrate to arrive at this value. The electrode gap and wire thickness were measured using a confocal microscope to characterize the exposure energy. Figure 3.7 shows the gap for various exposures. The ideal gap and wire thickness was10 microns and 25 microns respectively, which was achieved at 106 mJ/cm^2.

Table 3.1. Spin coating recipes

Coating	Step	Speed (rpm)	Ramp rate (rpm/sec)	Time (seconds)
HMDS	1	500	100	5
	2	4000	900	30
	3	0	1000	0.1
S1813 G2 photo resist	1	500	100	5
	2	4000	900	30
	3	0	1000	0.1
SU-8 2005 photo resist	1	500	100	5
	2	3000	300	30
	3	0	1000	0.1
Teflon	1	500	100	5
	2	1000	500	30
	3	0	1000	0.1

The aligner was fitted with a 5"x5" glass photomask designed using L-edit software (Tanner EDA) and printed at UT Dallas. The pattern on the photomask is imprinted on the PR layer of the glass wafer using this process. The wafer was then baked at 110°C at 1 minute 45 seconds to make the pattern stronger. The wafer was cooled on a hot plate for 3 minutes to remove standing waves in the pattern. The cooled wafer was agitated in a developer bath (Microposit MF-319) for 1 minute 15 seconds, rinsed with DI water and blow dried. The PR pattern was then observed under the microscope for accuracy. To further strengthen the pattern for etching, the substrate was hard baked at 135°C for 5 minutes. Water and CR-7 (KMG electronic chemicals) chromium etchant in a 1:4 mixture was used to etch the chromium. The etching was continued until it was visually confirmed that there is no stray chromium. The wafer was inspected under the microscope for accuracy. Thereafter. PR was stripped (Microposit remover 1165) at 75°C for 10 minutes.

After patterning the chromium electrodes, the wafer is cleaned using the above procedure. A 5 μm layer of SU-8 (microchem) was spin coated using the recipe in Table 3.1 to form the dielectric layer for electrowetting. The substrate was then baked at 65°C for 1 minute and immediately baked at 95°C for 2 minutes 40 seconds. The baked wafer was then exposed to a dose of 210 mJ/cm^2 using the OAI aligner. After exposing, the wafer was baked at 65°C and 95°C for 1 minute and 3 minute 40 seconds respectively. The wafer is then hard baked at 150°C for 5 minutes. The wafer is cooled slowly in the reverse order of baking to prevent cracks in the SU-8.

To form the hydrophobic layer, teflon solution (4% Dupont teflon AF1600 in FC40 solvent) was spincoated using the recipe in Table 3.1. This resulted in a 150 nm thick layer. The wafer was baked at 65°C, 150°C and 180°C for 1 minute, 2 minutes and 5 minutes respectively. The teflon spin coating process was repeated with baking at 65°C, 150°C and 180°C for 1 minute, 5 minutes and 15 minutes respectively. The teflon layer's thickness became 300 nm. This was done to reduce electrolysis during EWOD operation. The wafer is cooled slowly in the reverse order of baking to prevent cracks in the teflon. The completed device was finally annealed at 200°C in an oven for 5 hours to yield a uniform teflon coating and to evaporate all the solvent.

The ground (top) chip consists of a 5.8 cm x 5.8 cm ITO wafer drilled with two holes for fluidic connections. It is cleaned with acetone, IPA and methanol and rinsed with DI water. After dehydrating at 180°C for 5 minutes, the ITO is patterned using photolithography to form RTD. This is done using a transparency mask affixed to 5"x5" soda lime glass. All transparency masks were printed at CAD/Art services inc.

The patterned ground (top) chip is cleaned and dehydrated and spin coated with teflon solution using the recipe in Table 3.1.The wafer was then baked at 65°C, 100°C and 150°C for 1 minute, 5 minutes and 15 minutes respectively. This was done to prevent crystallization of ITO above 150°C [31], thus, ensuring the linearity of the

RTD. The wafer is cooled slowly in the reverse order of baking to prevent cracks in the teflon. Similarly, the top chip is then baked instead at 150°C in an oven for 2 hours to yield a uniform teflon coating and to evaporate all the solvent.

3.5 Experiment

As mentioned earlier, droplets are sandwiched between two parallel plates and translated over a simulated hotspot. The EWOD setup in parallel plate configuration consists of two glass wafers or chips - the EWOD (bottom) and ground (top) chips. These two chips could interchangeably be used in the top or bottom.

3.5.1 Setup and methodology

To conduct the experiments with the top and bottom chip, the chips need to be assembled in parallel plate configuration and held in place in this arrangement with supporting elements. Lexan™ was used to produce transparent polycarbonate pieces which were used to secure the EWOD (bottom) chip and the vertical connectors called ZEBRA™ connectors to interface the chip with the PCB. The entire setup was held with machine screws and nuts. Figure 3.8 shows the Lexan based EWOD setup with ZEBRA™ connectors and PCB. Double sided Kapton tape (Ted pella inc. 16087-12) is applied on the bottom chip to form spacers in the parallel plate configuration. The top chip has two holes drilled prior to cleanroom processing. These two holes correspond to fluidic connections for the inlet and outlet TCC reservoirs. Pipette tips (Eppendorf inc.) are attached and epoxy adhesive (Ace hardware quick set epoxy adhesive) is applied post fabrication to seal the connections.

The heater on the top chip is connected to the current source (Keithley 2400 source-meter) by means of 24AWG wires soldered onto copper strips attached to the top side of the ground (top) chip using silver epoxy adhesive (MG chemicals

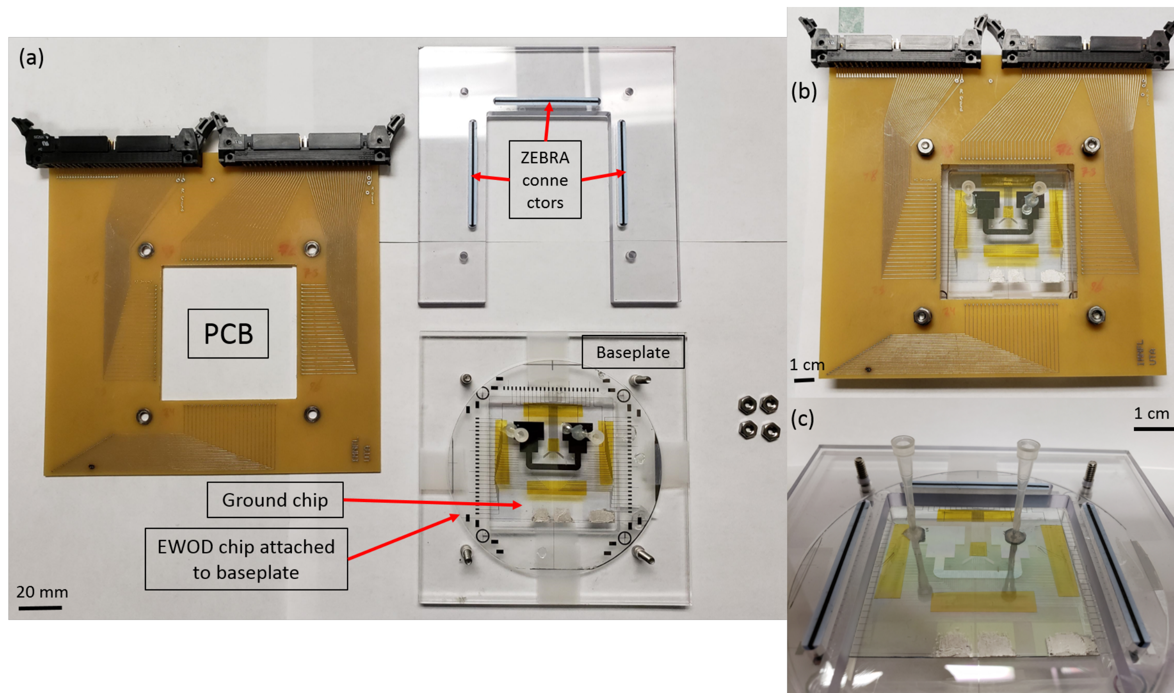

Figure 3.8. (a)Individual setup elements to assemble EWOD (b) Lexan pieces assembled with PCB (c) Close up view of ground (top) chip attached to EWOD device before placing PCB.

8331-14G). The silver epoxy is also applied on the side and underside of the ground (top) chip to complete the connection to the bus bars of the heater. Similarly, the ground connection is taken out and connected to the ground on the switch board. Figures 3.10 and reffig:expsetupsch show the schematic and actual pictures of EWOD setup. The PCB connects to a switching board using a pair of IDE cables. The switching board has 96 high voltage high speed relays corresponding to 96 outputs on the National instruments PCIe-6509 DAQ. The switch board is connected to the DAQ through another pair of IDE cables. The switching board is powered by a combination of function/arbitrary waveform generator (Keysight 33220A) routed through a voltage amplifier (TReK PZD350). The EWOD electrodes are switched ON/OFF using a labVIEW program which interfaces with the NI DAQ which in turn switches the

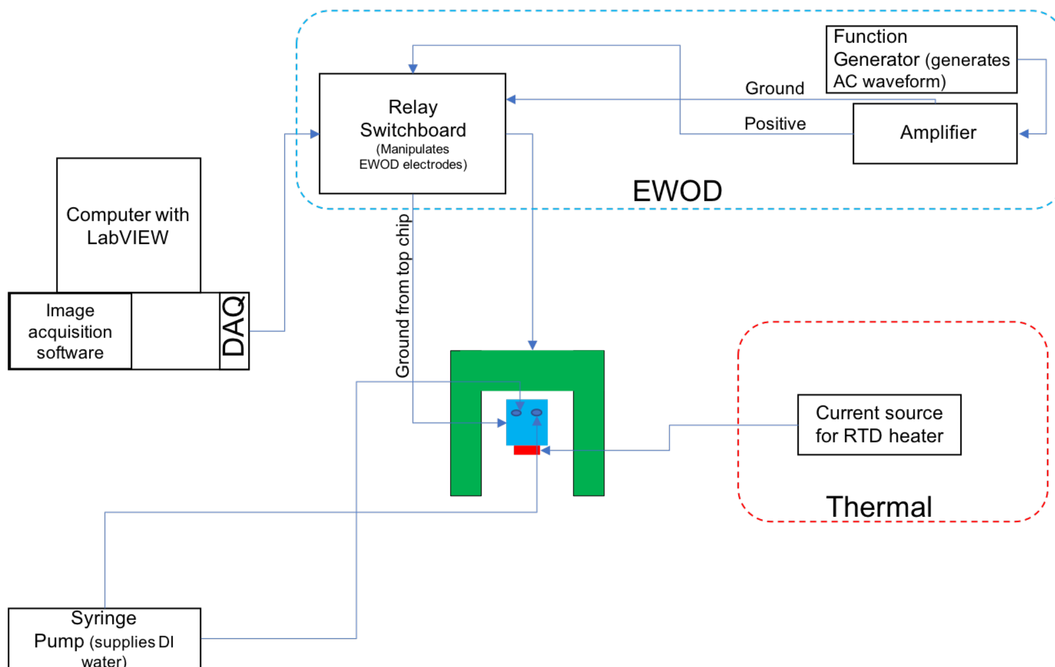

Figure 3.9. Schematic showing basic elements needed to operate EWOD.

relays corresponding to the electrodes on the chip. The switching of electrodes is automated inside labVIEW by feeding a text file containing the actuation scheme for various operations.

The RTD is operated through a separate labVIEW program interfacing with the current source. The current required for heating could be adjusted in the program. The resistance is measured using 4-wire method every 40ms to capture the temperature changes of hotspot during the high speed droplet motion. Prior to starting the experiment, the top chip is placed aligning the heater with the EWOD flow path and pressed to ensure a steady gap between the plates. The pipette tip corresponding to the inlet TCC reservoir is connected to a syringe by means of tubing (Tygon) and then placed in a syringe pump (KDS 100) as shown in the inset of Figure 3.10. The outlet pipette tip is connected to a syringe which is operated manually.

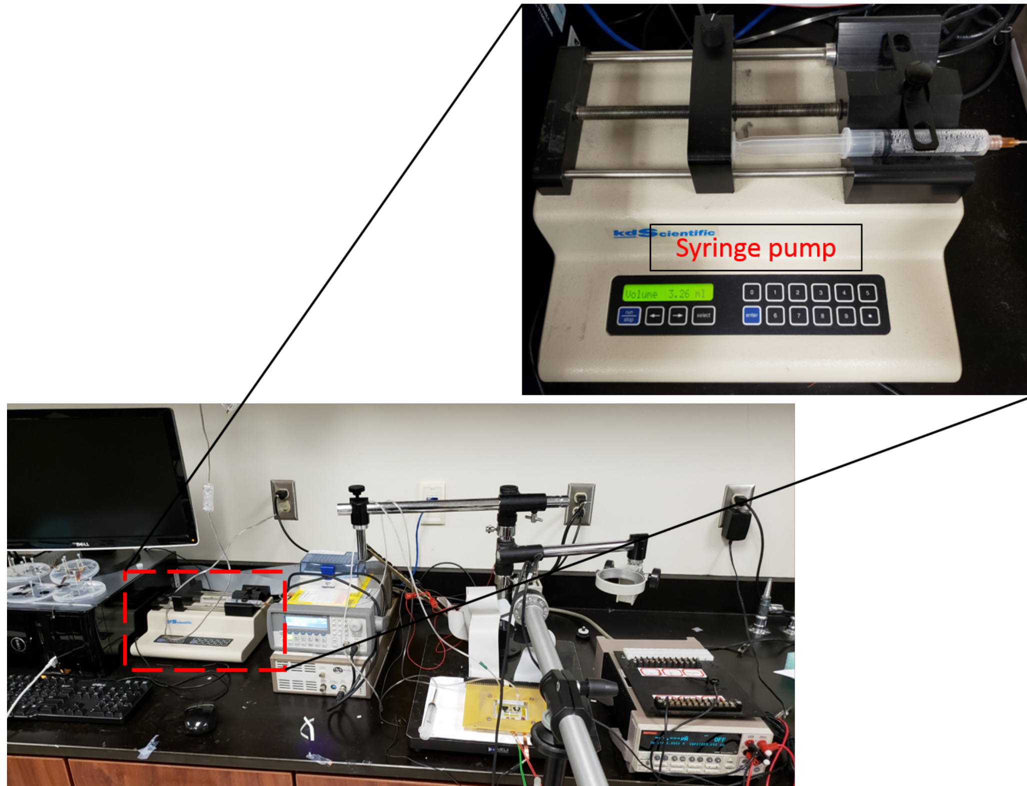

Figure 3.10. Pictures of EWOD setup. Syringe pump used for pumping liquid into the system (inset).

The droplet motion is visualized using a Hitachi camera (KP-D20A) affixed to a tripod hovering over the setup. The video obtained is recorded using OBS studio software. On completion of this setup, the heater is switched on by starting the corresponding labVIEW program and the heater is allowed to reach steady state. After about a minimum of 300s, the syringe pump and EWOD automation program are turned on and the hotspot temperature is continuously monitored as droplets travel over the hotspot. Variation in resistance of the RTD is captured and converted into temperature data using the calibration equation. The flow rate of the syringe pump is adjusted to match the generation rate of droplets.

3.6 Results and discussions

Several parameters affect the cooling of the hotspot. The inter-droplet delay dictates the number of droplets arriving on the hotspot in a given period of time. The switching time governs the droplet velocity. Figure 3.11 depicts the different parameters governing the droplet motion and heat transfer. The heat flux, inter droplet delay and switching time could be controlled through labVIEW programs. The heat flux is adjusted by changing the current passing through the heater. The inter-droplet delay is defined as the number of electrodes in between two consecutive droplets. The switching time is the time required to activate an electrode. The droplet will wet and de-wet the electrode in accordance with the activation or switching time. The inter-droplet delay is a function of the switching time. For a switching time of 50ms and a gap of 5 electrodes, the inter-droplet delay is 250ms.

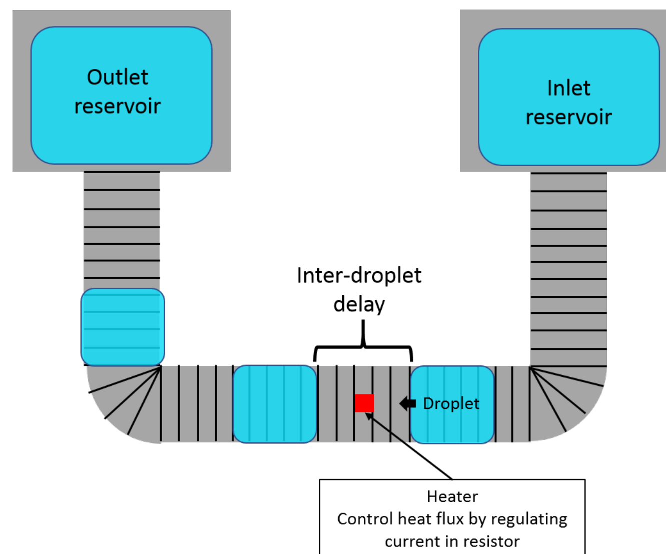

Figure 3.11. Electrowetting and heat transfer parameters.

3.6.1 Anatomy of hotspot cooling curve

Figure 3.12 shows the variation of hotspot temperature $T_{hotspot}$ with time. At the beginning of the experiment, the hotspot is allowed to reach steady-state and after a minimum of 300 seconds, the syringe pump and EWOD motion is switched on. On arrival of the advancing meniscus of the first droplet, there is a sharp drop in temperature owing to the cooling of the hotspot. The hotspot is in contact with the droplet for a period equal to:

Droplet dwell time = number of electrodes spanned by droplet x switching time

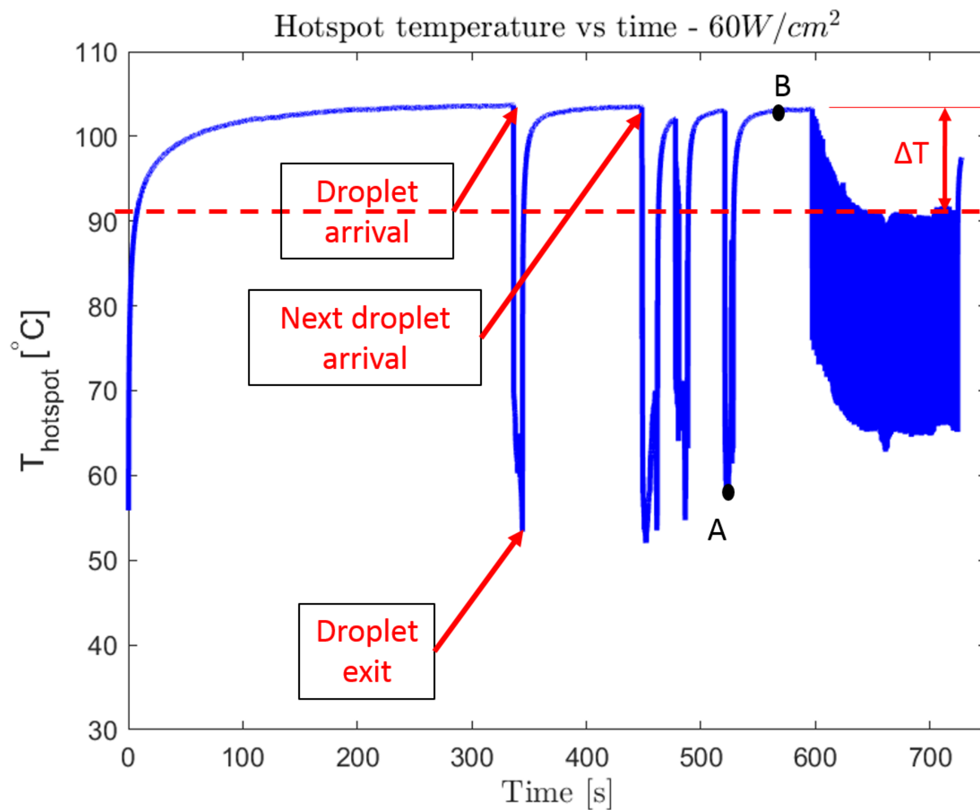

Figure 3.12. Anatomy of a transient cooling curve for electrowetting based hotspot cooling. Heat flux = 60 W/cm^2, switching time = 50 ms, inter-droplet delay = 250 ms, operating voltage = 150 ACV at 1 kHz.

During this short period of time, the hotspot undergoes cooling. On departure of the droplet, the hotspot experiences intermittent dryout which causes its temperature to shoot up to its steady-state value. As the temperature proceeds to rise, the next droplet arrives and the cycle continues. Although, there is a significant drop in $T_{hotspot}$, The reduced hotspot temperature on arrival of the first droplet, however, is not sustained once the droplet leaves the hotspot. The temperature spikes back up towards its steady state value. Multiple droplets can cause multiple dips in temperature and could help offset the transient response of the heater. This prevents the hotspot from reaching its steady state temperature. The rapid recovery behavior of the hotspot makes it necessary to feed droplets continuously to maintain the temperature in a specified envelope for a given heat flux.

3.6.2 Continuous/sustained droplet motion

Figure 3.12 also depicts the variation of $T_{hotspot}$ with time for the multiple droplet case. As can be seen, the heater is allowed to reach steady state evidenced by the flatlining of the temperature value with time. Soon after, liquid delivery is started. Droplets of water cross over the hotspot and cool it intermittently. This causes the temperature to fluctuate. The inset depicts a close up view with a sharp drop in temperature on droplet arrival. On droplet exit, the hotspot temperature shoots back up due to a temporary dryout until the next droplet arrival.

By sustaining a steady stream of droplets, the hotspot heat flux is contained and the hotspot temperature is maintained at a lower value than steady state. The cooled hotspot temperature is a function of a number of parameters. Two critical points are highlighted in Figure 3.12. Point A denotes the lowest hotspot temperature following an instantaneous drop on droplet arrival. Point B refers to the highest temperature

the hotspot attains before the arrival of the next droplet. ΔT is the difference between hotspot steady-state temperature and the overall drop in hotspot temperature.

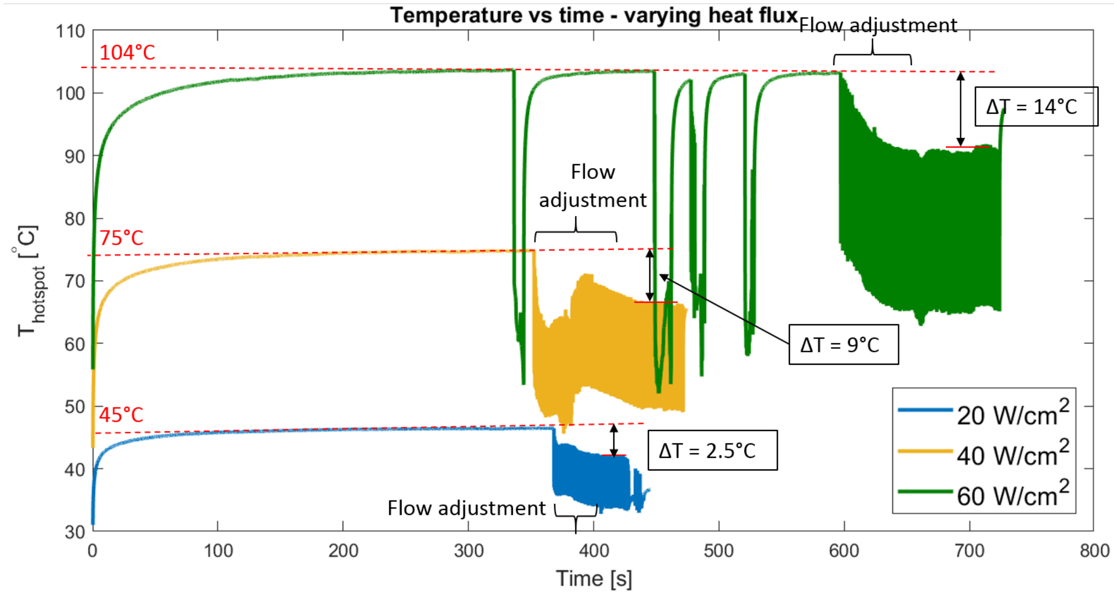

Figure 3.13. Hotspot temperature vs time for different heat fluxes 20, 40, 60 W/cm^2. Switching time = 50 ms, inter-droplet delay = 250 ms, operating voltage = 150 ACV at 1 kHz.

3.6.3 Variation of heat flux

Figure 3.13 shows the effect of varying the heat flux on the hotspot temperature keeping other parameters unchanged. The experiment is conducted at heat fluxes of 20, 40 and 60 W/cm^2. Higher heat flux causes an increase in the hotspot temperature. Figure 3.14 shows an image of a droplet moving over the hotspot for various heat fluxes. There is visible condensation on the droplet edges at 60 W/cm^2 suggesting evaporation at the meniscus. Higher heat flux allows for a bigger temperature drop due to increased possibility of phase change which can be neglected at lower heat fluxes.

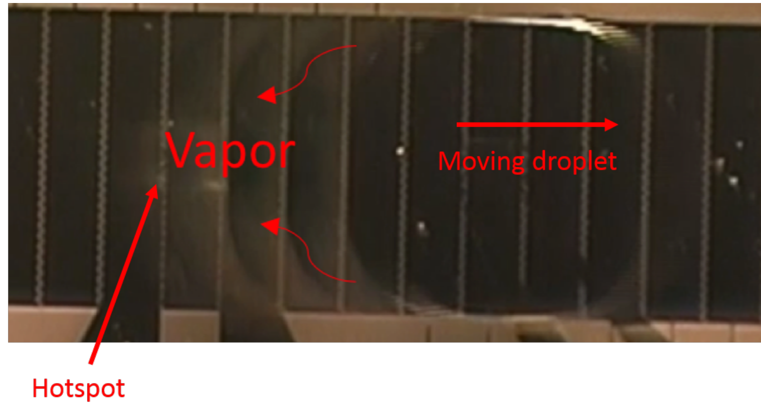

Figure 3.14. Visible condensation for droplet moving over the hotspot at high heat flux (60 W/cm^2). Switching time = 50 ms, inter-droplet delay = 250 ms, operating voltage = 150 ACV at 1 kHz. Detailed video available at [link].

3.6.4 Effect of inter-droplet delay

The inter-droplet delay can be controlled by adjusting the electrode gap between two droplets. With a constant switching time, the inter-droplet delay is defined as:

Delay = number of deactivated electrodes between droplets x switching time

Figure 3.15 shows the hotspot temperature variation with time for different inter-droplet delays and constant switching time. It is clear that by reducing the inter-droplet delay, the recovery of the hotspot temperature is cutoff at an earlier stage compared to 500ms. Thus , the inter-droplet delay is competing with the thermal time constant of the system. Having an inter-droplet delay less than the thermal time constant of the system will result in a higher ΔT and hence a perceivable temperature drop from steady state.

3.6.5 Effect of switching time

Reducing the switching time also indirectly reduces the inter-droplet delay but it also increases the droplet velocity. Since the droplet dwells over the hotspot for a very short period of time (250ms), the time constant of the heat transfer process

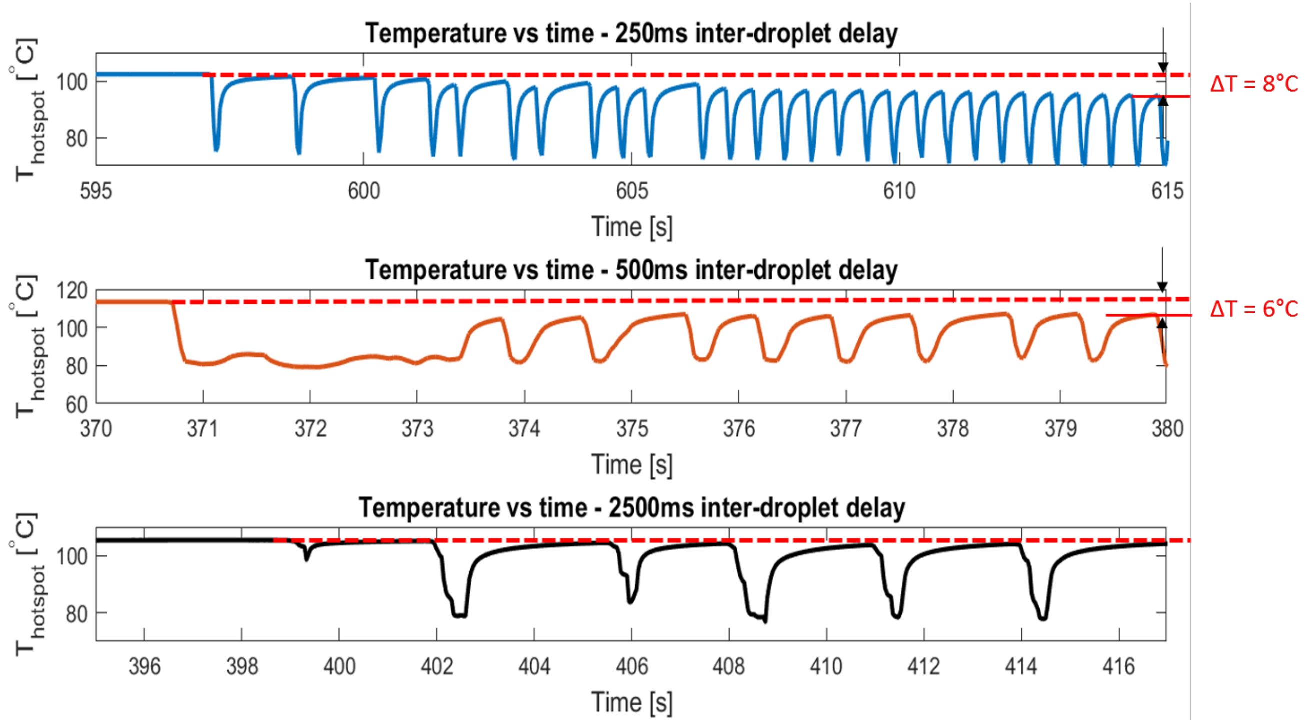

Figure 3.15. Hotspot temperature vs time for varying inter-droplet delay and constant switching time. Heat flux = 60 W/cm^2, switching time = 50 ms, operating voltage = 150 ACV at 1 kHz.

in comparison to the dwell time will then decide the efficacy of the cooling process. A low switching time increases the droplet velocity. The increased droplet velocity improves the convection within the droplet and can cool the hotspot to a greater extent. Figure 3.16 shows this effect with constant inter-droplet delay of 500ms and at a heat flux of 60 W/cm^2. To better understand this phenomena, the heat transfer mechanism needs to be elucidated. This can be clarified by conducting a thermal resistance network analysis.

3.6.6 Thermal circuit analysis

To understand the cooling mechanism of EWOD, it is important to create a thermal circuit of the system. This helps analyze the heat flow from the heater to

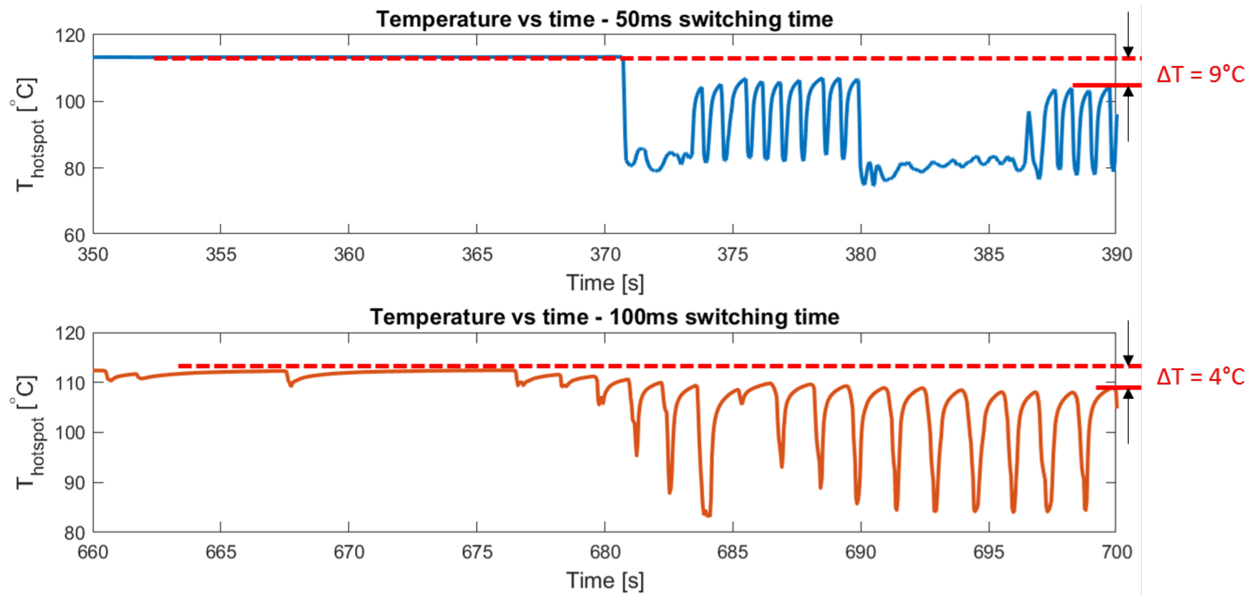

Figure 3.16. Hotspot temperature vs time for different switching times and constant inter-droplet delay. Heat flux = 60 W/cm^2, inter-droplet delay = 500 ms, operating voltage = 150 ACV at 1 kHz.

the ambient. Figure 3.17 shows the thermal circuit. The heat from the heater has two major pathways: (1) heat spreading through the substrate which is carried away by convection to the ambient, (2) Heat conduction through the layers to the droplet and top chip which is dissipated by a combination of evaporation and convection. The evaporative heat transfer coefficient has been found by Bindiganevale et al. to 2624 W/m^2K for a heat flux of 36.6 W/m^2. By assuming a convective heat transfer coefficient h = 1 W/m^2K, the temperature value obtained shows a good match with the experimental data. As can be seen from Table 4.2, the thermal resistance due to evaporation is 5 times the convection thermal resistance. The air convection here plays a major role in the cooling as opposed to droplet evaporation and conduction owing to its low thermal resistance. For evaporation to be of significance, it must be enhanced so that its thermal resistance is comparable to or lower than that of convection.

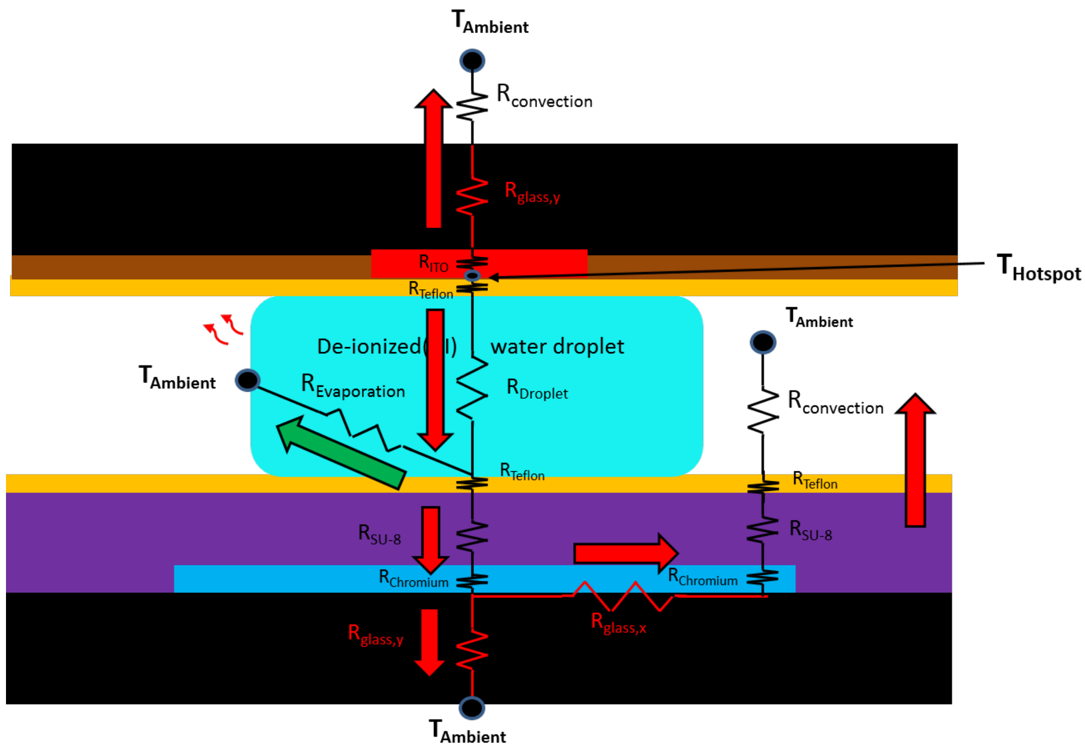

Figure 3.17. Thermal resistance circuit for EWOD cooling.

3.7 Conclusions

High speed EWOD based cooling was demonstrated. ITO RTD was used to monitor the hotspot temperature as well as to simulate the hotspot. The effect of various parameters such as inter-droplet delay, switching time and heat flux was studied. The thermal resistance circuit of the system showed that air convection is the dominant mechanism for cooling instead of droplet evaporation and conduction. This could be manipulated by enhancing the evaporation so as to make it the preferred heat path to the ambient.

Material	Thermal conductivity, k (W/mK)	Thermal resistance (°C/W)	Length, L(m)	Area, A(m^2)
Glass	0.8	5794.7	1x10^{-6}	1.5110^{-7}
Chromium, Cr	90	7.35x10^{-3}	1x10^{-7}	1.5110^{-7}
Teflon bottom	0.25	7.947	3x10^{-7}	1.5110^{-7}
Teflon top	90	3.973	1.5x10^{-7}	1.5110^{-7}
SU-8	0.3	132.45	6x10^{-6}	1.5110^{-7}
ITO	11	0.0752	1.25x10^{-7}	1.5110^{-7}
DI water	0.6065	1091.39	100x10^{-6}	1.5110^{-7}
Air convection (h=1 W/m^2K)	-	431.03	-	2.3210^{-3}
Evaporation (h=2624 W/m^2K)	-	2523.82	-	1.5110^{-7}

Table 3.2. Material properties for thermal resistance calculation

CHAPTER 4

STUDY II - HOTSPOT COOLING USING THIN FILM EVAPORATION

With the help of study I, discussed in the previous chapter, it has been established EWOD as a suitable candidate for hotspot cooling. A high speed version of this technology is available which is a better adaptation for hotspot cooling compared to the lab on a chip. In the previous study, it was concluded that although digital microfluidics can be leveraged for cooling, the coolant droplet aided air convection but did not undergo significant evaporation. Convection, on the other hand, was the pathway of choice for the heat to escape to the ambient. There are several ways to force the system to use the droplet as a means of cooling. Our focus is to increase component of evaporation while reducing reliance on the other cooling pathways.

Phase change phenomena encompasses boiling and evaporation. Boiling occurs at or above boiling temperature when the equilibrium vapor pressure of the substance is greater than the pressure exerted by the surrounding atmosphere. It is a bulk phenomena as opposed to evaporation which only occurs on the surface. Evaporation is a result of the escape of liquid molecules into the atmosphere as a gas. The molecules should have enough energy to overcome the vapor pressure, thus as a result of removal of this energy, evaporative cooling is observed. Both phenomena remove heat equal to the latent heat of vaporization of the liquid but evaporation can occur at any temperature.

As mentioned in chapter 1, boiling in microchannels has been widely researched but it is not without issues. Major issues of this method include high pressure drop required to pump the liquid and flow instabilities. Although, these problems would

be absent in EWOD due to its pumpless operation and sidewall less device design, evaporation is chosen over boiling. Boiling is a violent phenomena which requires high temperatures unlike evaporation. Thus, the device design should be such that it promotes evaporation instead of boiling.

Controlling the environment is out of scope of this work. Therefore, changing the heat transfer mode to phase change is feasible. To enforce and increase evaporation, the factors affecting the phenomena need to be understood and also, the behavior exhibited at the microscale.

4.1 Thin film evaporation

The rate of evaporation depends on several factors:

- **Concentration gradient.** It is one of the driving forces. The degree of saturation of the surrounding air affects the rate.
- **Pressure.** A lower pressure will allow for the liquid molecules to easily escape resulting in higher evaporation.
- **Air flow.** With the concentration gradient remaining the same, introduction of fresh air always favors faster evaporation.
- **Latent heat of vaporization.** Higher intermolecular forces would require higher enthalpy of vaporization.
- **Surface area.** A larger effective surface area will allow more molecules to escape.
- **Temperature.** Higher temperature will result in more kinetic energy of molecules which increases the rate.

Since the experiment will be carried out in ambient conditions to better mimic the environment of a typical microprocessor, only certain factors can be controlled. Those factors include surface area and temperature. The temperature is dictated by the heat

flux supplied to the hotspot. The surface area available for evaporation, on the other hand, could be manipulated.

Since the focus is on using droplets to cool hotspots, evaporation mechanism at the microscale needs to be understood. In 1964, Derjagin et al. [32] was one of first to study factors affecting the rate of evaporation in a capillary tube. It was determined that difference in intermolecular forces within the droplet contributed to liquid flow within the droplet. This in turn affected the rate of evaporation at this scale. The long range intermolecular forces are often referred to as the disjoining pressure [33]. The evaporation at this scale is referred to as thin film evaporation (TFE). The thickness of the liquid film in the thin film range is still ambiguous due to the limitations of studying a thin film.

Figure 4.1 shows a schematic showing evaporation at the microscale. Evaporation being a surface phenomena, at the microscale, the meniscus of the droplet is where thin film evaporation is focused. Hypothetically, a perfectly wetting fluid can be divided into three regions: (1) adsorbed region, (2) transition region and (3) bulk fluid [34]. Adsorbed film region is closest to the apparent contact line where the solid, liquid and gas phases meet. In this region, there is no evaporation due to the high intermolecular forces (disjoining pressure) between the solid and liquid molecules. The transition region sees a weaker disjoining pressure and a finite curvature of liquid-vapor interface. The bulk fluid region contains the bulk of the droplet and the contact angle is measured from the constant curvature of the liquid-vapor interface. Also, the intermolecular forces are its weakest here.

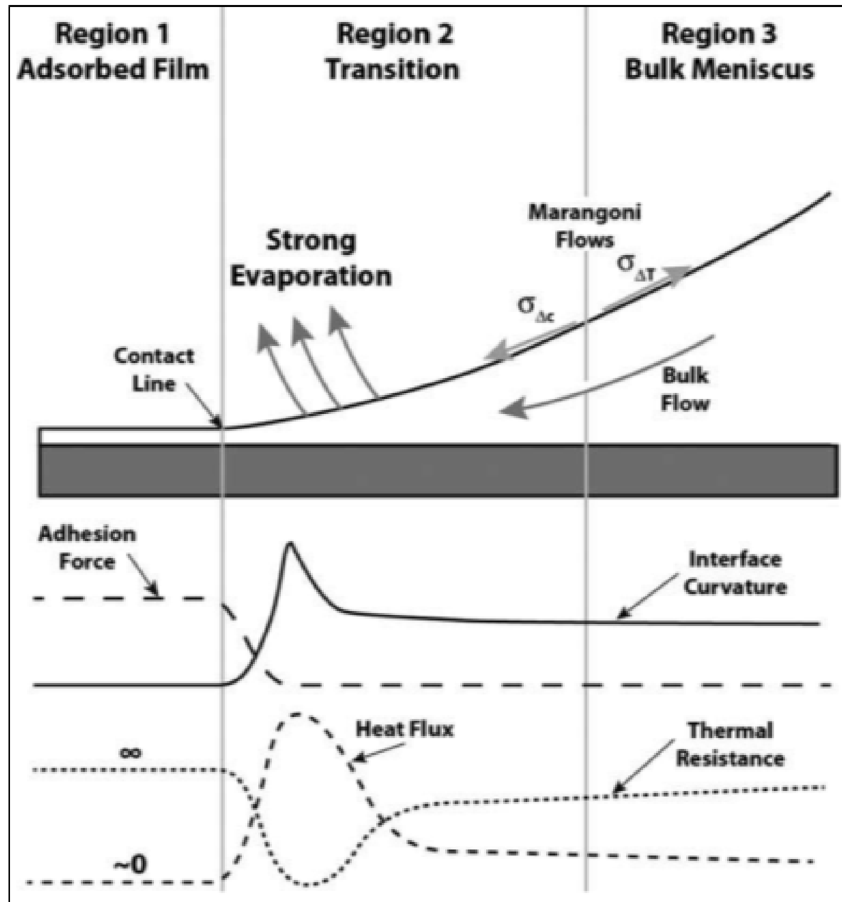

Figure 4.1. Anatomy of a perfectly wetting fluid. Variation of adhesion force, interface curvature and thermal resistance along the three regions [34].

There exists a disjoining pressure and curvature gradient between region 2 and 3. This is responsible for the fluid flow from region 3 to 2 owing to intermolecular and capillary forces. The bulk fluid region hence, feeds the transition region with fluid. Let's also look at the heat transfer characteristics of each region. The total thermal resistance in each region is composed of the conduction resistance in the solid, conduction resistance through the liquid and a liquid-vapor resistance acting at the interface [34]. The curvature and as a result the film thickness influences the liquid conduction resistance and interfacial liquid-vapor resistance. The film thickness

affects the disjoining pressure and eventually the interfacial liquid-vapor resistance. So, the disjoining pressure plays an important role in the overall thermal resistance.

The adsorbed film region, owing to no evaporation, has an infinite thermal resistance. The bulk region also, has high liquid conduction resistance due to a thicker liquid film than the other two regions. However, the transition region has the lowest overall thermal resistance of all three regions. This is attributed to thin enough liquid film which imposes an intermediate liquid conduction resistance. At the same time, the liquid film is thick enough for a low disjoining pressure leading to low interfacial liquid-vapor thermal resistance [34].

In addition to thermal resistances, hydrodynamic resistances decide how fast liquid can be delivered to the transition region and how fast the liquid vapor could be removed. Maximizing the transition region will maximize the evaporation of a droplet. At the same time, it should not come at the cost of increased hydrodynamic resistance which will again reduce the evaporation. Once evaporated, the vapor has to be pumped out to maintain the concentration gradient and support evaporation in case of closed systems.

4.2 Literature review

It has been established that maximizing the transition region maximizes the evaporation. Plawsky et al. [35] postulated that decreasing the contact angle increases the length of the transition region. Thus, a number of research works focus on surface modification to create superhydrophilic surfaces, which has a contact angle close to zero. Ojha et al. [1] studied experimentally the effect of magnitude and shape of surface roughness on microscale transport in the contact line region of liquid meniscus in 2010. The rough surface exhibited a higher evaporative heat transfer. In another

study, Ojha et al. concluded that nanoscale surfaces could be used to change the rate phase change rate[36].

As mentioned earlier, hydrodynamic resistances also play a crucial role in addition to the thermal resistance. One research work illustrates this issue. Ranjan et al. [37] checked the viability of nanowicks as shown in Figure 4.2 (right). Their analysis concluded that nanowicks generate a high capillary pressure. However, due to the decreased permeability, it has high resistance to fluid flow. Similarly, there are other works which employ nanostructures without the aforementioned issues. Nam and Sungtaek Ju [38] compared the heat transfer performance of nanostructured CuO wick samples and bare Cu wick samples in Figure 4.2 (left). They were able to delay dryout and improve critical heat flux (CHF) by 70%.

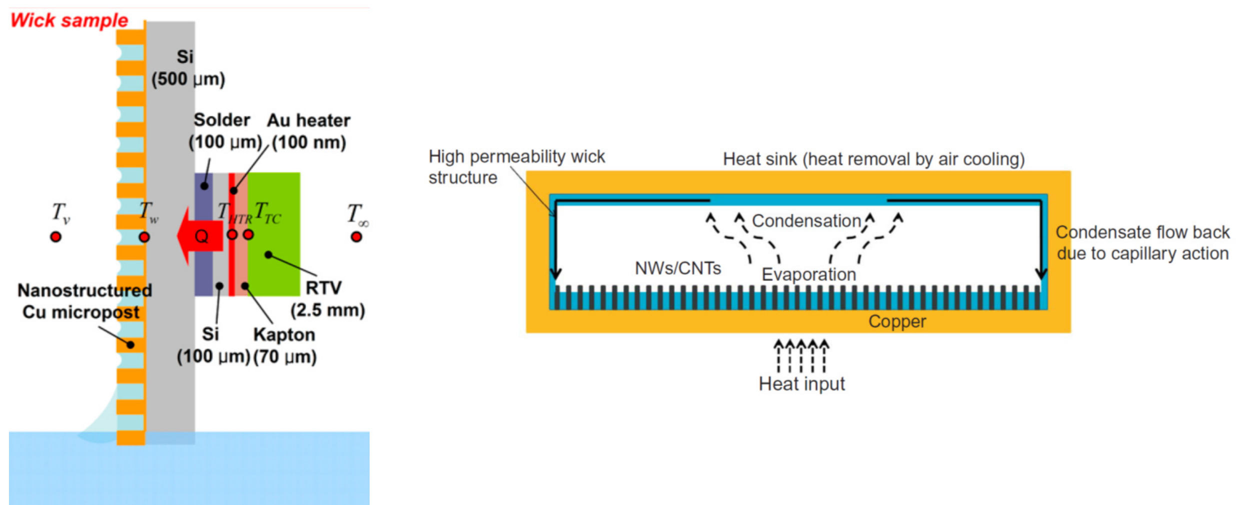

Figure 4.2. Nanostructured Copper oxide attached to heater chip (left) [38].Vapor chamber heat spreader lined with carbon nanotubes/nanowicks [37].

In addition to nanostructures, Xianming et al. used micromembrane enhanced evaporating surfaces to significantly enhance heat transfer coefficient and CHF [39] as shown in Figure 4.3 (right). A passive method was utilized to deliver water to the evaporating surface and were able to dissipate 152.2 W/cm^2. Narayanan et al., on the other hand, actively pumped water below a porous anodic alumina membrane which confines the liquid by capillary action [40] as shown in Figure 4.3 (left). The membrane top side is subjected to an impinging gas flow. They were able to dissipate 600 W/cm^2 consistently. The main drawback to this work is the elaborate setup needed to setup gas impingement and energy expended to achieve the same.

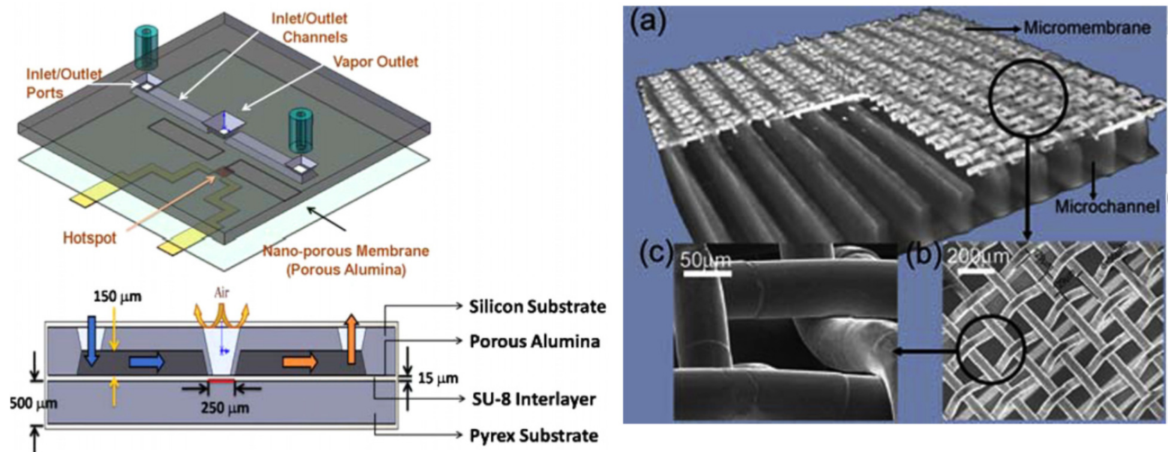

Figure 4.3. Capillary confinement using nanoporous membrane (left) [40].Micro-XCT image showing micromembrane composed of copper mesh [39].

Cheng and Chen integrated a copper mesh based hydrophilic hotspot into a parallel plate EWOD device [41]. Boiling was observed on the hotspot at relatively low heat fluxes of 25 W/cm^2 due to a thick copper mesh (1 mm) as shown in Figure 4.4 (left). The device was not able to maintain a thin film and as a result had huge

spikes in temperature. Similarly, Park and Nam integrated a hydrophilic coating on a single-sided EWOD chip [42] in Figure 4.4 (right). The hotspot was coated with a hydrophilic coating and promoted phase change. The device was able to dissipate 130 W/cm^2. The single sided configuration allows for high droplet velocities in the absence of friction from the top plate. However, the single sided configuration is not suitable for integration with microprocessors due to their open nature.

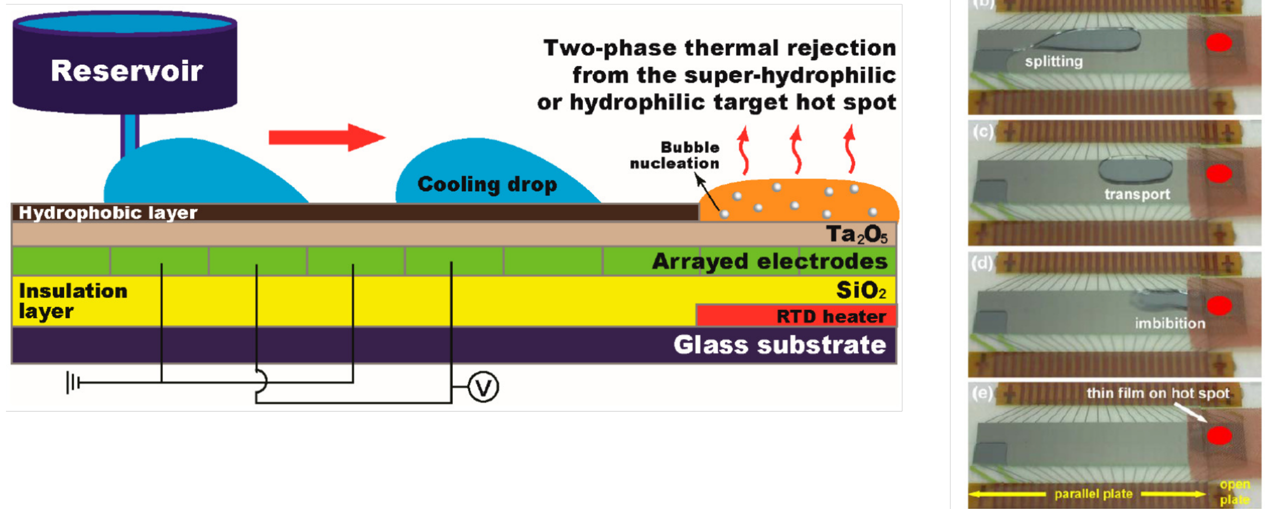

Figure 4.4. Hydrophilic hotspot implemented in open EWOD configuration (left)[42]. Copper mesh hydrophilic hotspot implemented in a hybrid open-sandwiched configuration [41].

In 2015, Bindiganevale et al. integrated a hydrophilic hotspot into a parallel plate EWOD device [16]. The device was able to handle heat fluxes upto 36.6 W/cm^2. Water droplets were brought over the hotspot where a small hydrophilic opening was present. On leaving the hotspot, the drop leaves behind a small pool of water to

prevent dryout. The hydrophilic hotspot is replenished with water from time to time. Evaporation was observed in the advancing and receding menisci.

In 2016, Adera et al. used micropillar wicks to passively deliver water to cool hotspots [43]. The device made use of passive liquid transport by use of capillary forces to deliver liquid to the micropillar wicks. The wicks are able to dissipate 5.8 kW/cm^2 using thin film evaporation. Although, the work made use of thin film evaporation and passive liquid delivery to achieve cooling, the experiment was carried out under saturated conditions. Moreover, a majority of the heat flux dissipated is not purely evaporative.

Wiedenheft et al. cooled hotspots using jumping drop vapor chambers [44]. Traditional

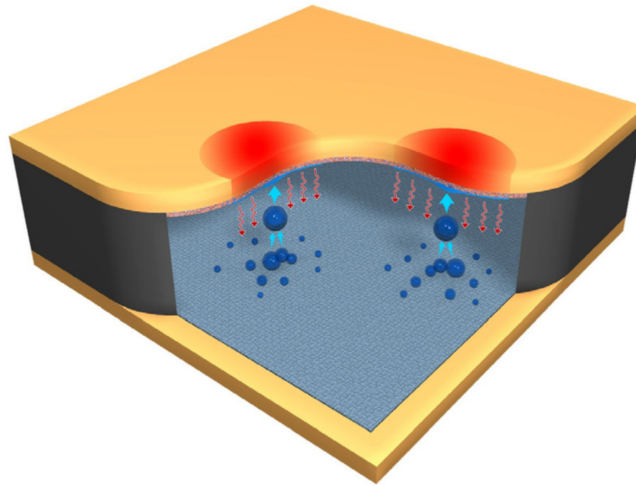

Figure 4.5. Jumping drop vapor chamber [44].

vapor chambers suffer from poor out of plane heat transfer. In addition to the conventional wicking struture on the sides of the evaporator, the condenser induces jumping of drops due to a difference in surface energy caused by coalescing of drops. This jumping of droplets creates an additional return path to the evaporator for the coolant as shown in Figure 4.5. This method demonstrates an effective thermal

conductivity equivalent to that of copper. Non condensable liquids can shorten the operation lifetime of such devices. Also, currently, the coating of this device is not able to withstand high vapor temperatures.

Hanks et al. [45] implemented nanoporous membranes instead of micropillars to improve upon their previous attempt [43]. Heat conduction is dominant in a number of these wicking structures and to mitigate this issue, nanoporous membranes have been used as shown in Figure 4.6. To achieve such high resolution in fabrication, interference lithography was used. Another issue in passive capillary transport is loss of permeability to achieve high capillarity. This can be taken care of by using biphilic structures. Heat fluxes of 665 W/cm^2 were achieved in this attempt. A major problem with nanostructures of this scale is fouling which affect the sustained running of these devices.

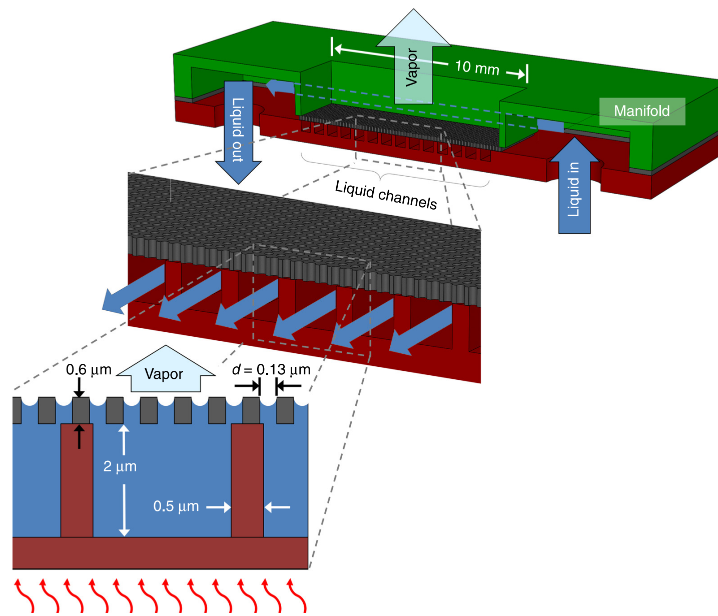

Figure 4.6. Passive liquid transport using nanoporous membrane [45].

4.3 Design

A number of research works have investigated thin film evaporation as a cooling method. Incorporating thin film evaporation in an EWOD device would certainly increase the role of phase change in hotspot cooling. To accomplish this objective, the following requirements need to be met:

- Inject coolant into system
- Transport coolant droplets over to hotspot
- Induce thin film evaporation over hotspot
- Heater to simulate hotspot
- Monitor and record hotspot temperature

4.3.1 Device structure

Based on the literature survey, surface modification to increase surface roughness and reduce the contact angle of the wetting fluid, can enhance evaporation. The reasoning behind this enhancement relates to increase in the transition region of the droplet by increasing the fluid wettability. More than 80% of the evaporation in a droplet happens in this microregion. To take advantage of this phenomena, a superhydrophilic surface should be employed in conjunction with electrowetting.

To induce thin film evaporation over the hotspot, a superhydrophilic area has to be created over it. Similar to study I, EWOD will be implemented in a parallel plate configuration. However, the hotspot and hence the superhydrophilic region would be open to the environment to facilitate easy removal of vapor.

EWOD in parallel plate configuration requires the use of two plates or chips. In this case, the bottom plate will be composed of the ground electrode and RTD heater covered with a superhydrophilic coating. The ground region on the bottom chip will be coated with a hydrophobic layer to coincide with the EWOD region on

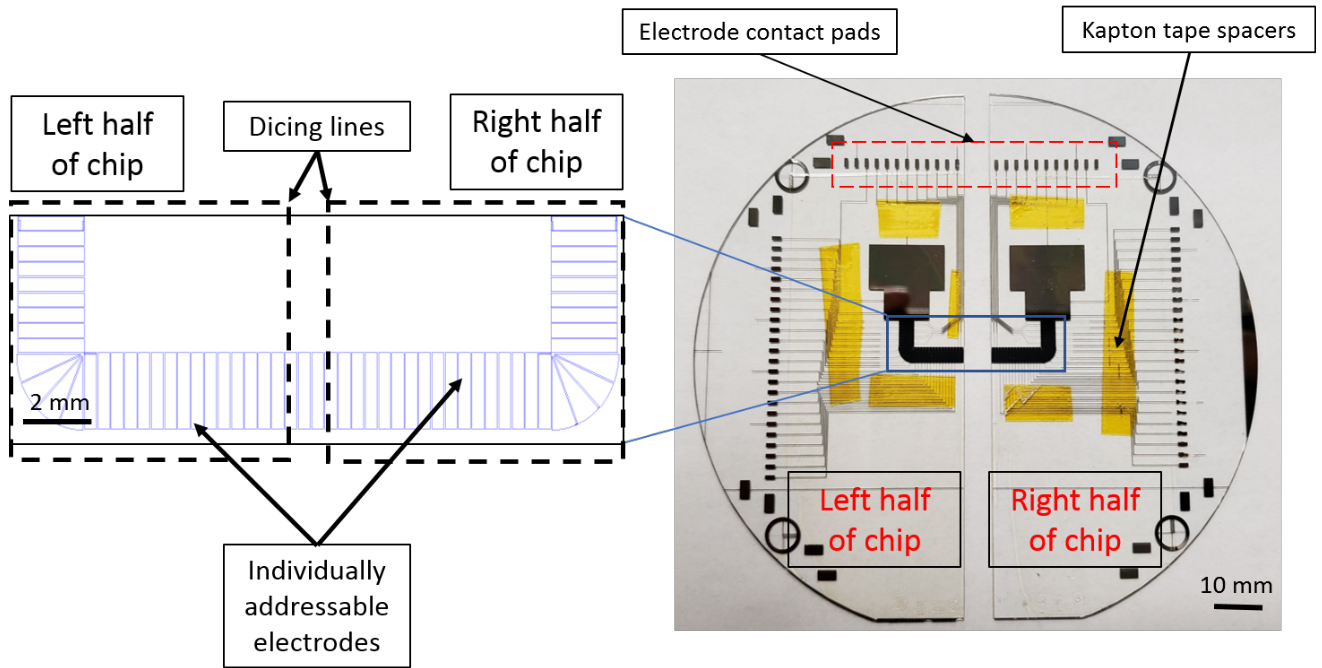

Figure 4.7. EWOD (top) chip design.

the top chip. The top chip, on the other hand, will consist of conductive electrodes coated with dielectric and hydrophobic layers. Both the plates, as done earlier, would be separated by a small gap (100 microns) where the droplet is sandwiched.

Figure 4.7 shows the design of EWOD (top) chip. Similar to the design for study I, to transport droplets efficiently over the hotspot, a manageable droplet volume has to be generated. L-junction along with slender electrodes would be implemented to expedite the generation and delivery of droplets to the hotspot. Sustained droplet delivery is enabled by creating a large reservoir to hold the coolant and supply as needed. Since the cooling droplet would evaporate over the superhydrophilic area, a 2nd reservoir for used droplets is not needed. Generated droplets are transported via a path of inter-digitated slender electrodes to the hotspot. The dimensions are so chosen that 5 electrodes worth of coolant when sandwiched between the two plates will amount to 0.9 μL. The gap between electrodes is ten microns, which is a

limitation imposed by fabrication constraints. Each of electrodes are connected by traces to contact pads surrounding the edge of device which will interface to a PCB.

Figures 4.8 and 4.9 depict the bottom ground chip. Figure 4.8 shows the ground (bottom) chip design before dicing. Once diced these chips could be used for the respective EWOD half devices. Figure 4.9 shows the ground (bottom) chip post dicing into two halves. Also, holes will be drilled into the wafers to facilitate liquid supply connections. The two plates are maintained at a fixed gap of 100 microns using kapton double sided tape as a spacer. Although EWOD would still function at different gaps, this value has been chosen for optimal electrowetting force for cutting and transport. Each of the halves have an octagonal superhydrophilic area. The shape of the superhydrophilic area is designed as such to provide sufficient space for the wiring to pass between the reservoir and the superhydrophilic area. The size is calculated by assuming that a 4 μL droplet spreads into a thin film 10 μm thick over the superhydrophilic area. This yields a 2 cm x 2 cm superhydrophilic region. Coolant must be continuously supplied to the reservoir to sustain droplet generation. To accomplish this, a hole has been drilled in the ground (bottom) chip to coincide with the location of the EWOD reservoir when assembled in parallel plate configuration. Furthermore, a single pipette tip has been attached to the drilled hole using quick-set epoxy to allow for an external fluidic connection. The pipette tip is in turn connected to a syringe using TYGON tubing which is operated by a syringe pump to supply coolant to the generating reservoir.

One of the main requirements of this EWOD chip is the ability to simulate a hotspot and monitor hotspot temperature. Thin film RTDs are compatible with photolithography techniques thus, the perfect choice for measuring temperature in EWOD devices. At the same time, additional current could be supplied to the

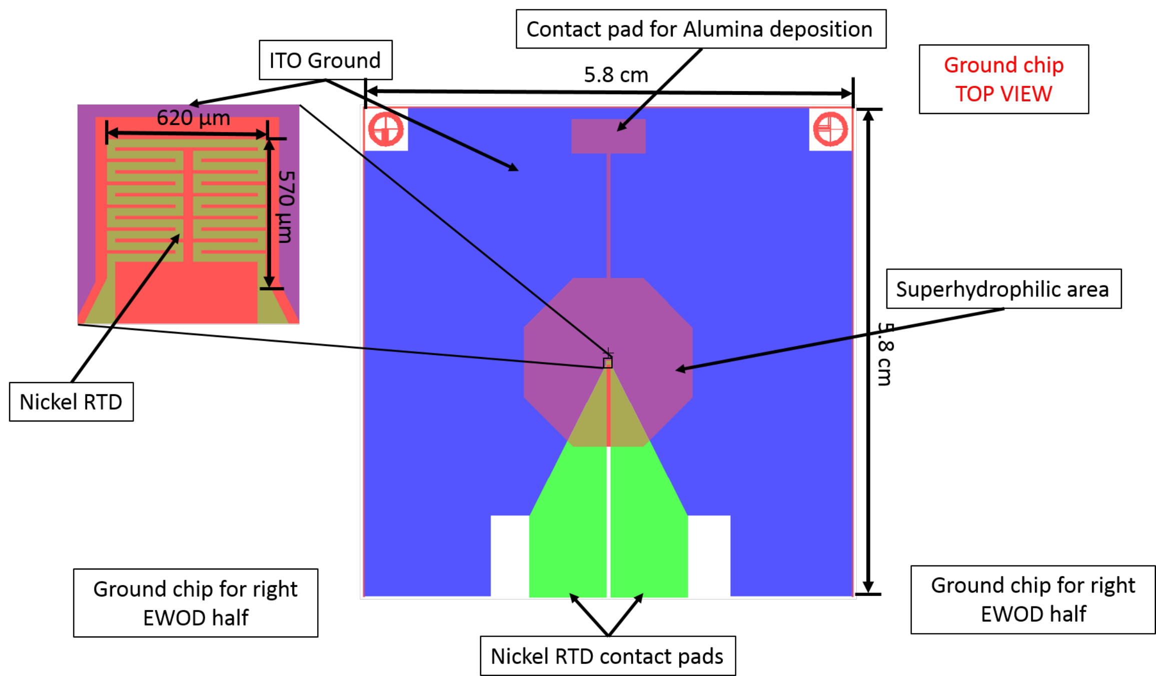

Figure 4.8. Ground chip (bottom) design before dicing.

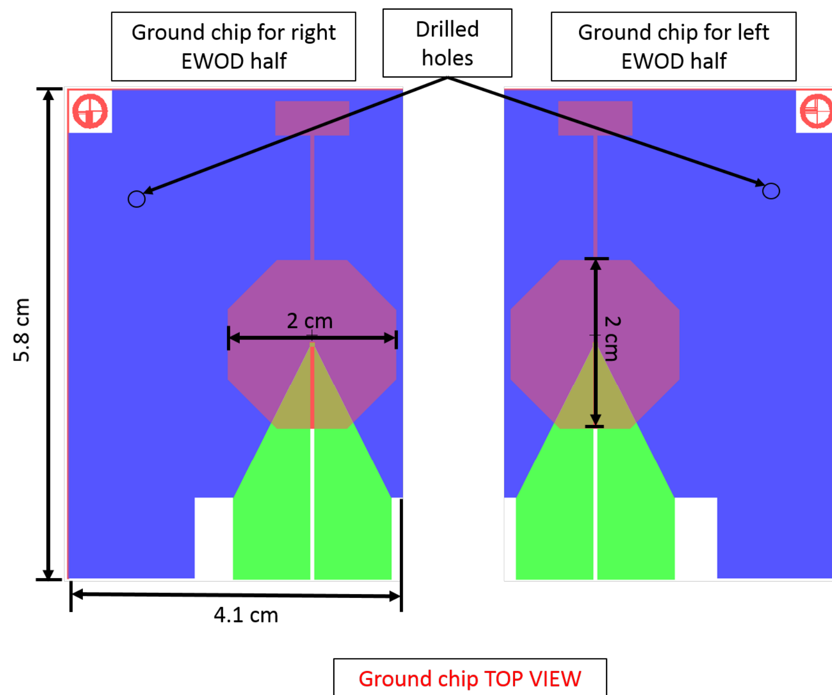

Figure 4.9. Ground chip (bottom) design for two EWOD device halves.

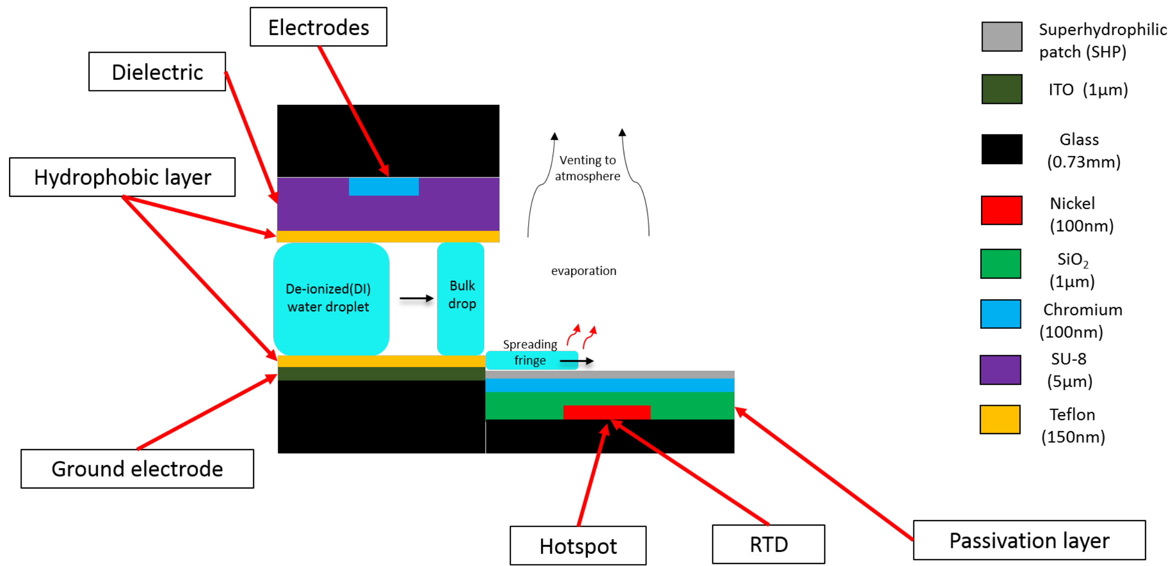

Figure 4.10. Material selection: EWOD stack in parallel plate configuration.

RTDs to induce joule heating for hotspot simulation. The heater is located in the superhydrophilic region at the end of the EWOD pathway.

As mentioned in chapter 3, it is preferred to integrate the RTD in the ground (bottom) chip away from the EWOD electrodes to prevent noise due to EWOD actuation signal and also to avoid reducing EWOD performance.

4.3.2 Material selection

Figure 4.10 shows the EWOD stack using the material choices detailed here. The EWOD (top) chip consists of chromium EWOD electrodes which form the basis of droplet movement. The SU-8 forms the dielectric layer which charges and discharges on application of the underlying electric field. The dielectric layer, mentioned in the chapter 2, stores electric charge which influences the surface tension force balance of the droplet. The teflon layer provides the hydrophobicity which provides a surface with low surface energy.

A glass substrate was used for the ground (bottom) chip instead of silicon due to its low thermal conductivity. All the electrodes were fabricated using chromium due to its low electrical resistance, good adhesion with glass, ease of fabrication and visualization in experiments. SU-8 was chosen as the dielectric due to simplicity of coating and uniformity. Moreover, its dielectric constant is high enough to avoid electrolysis.

The ground (bottom) chip was composed of a glass wafer coated with Indium tin oxide (ITO). This was patterned to form ground and provide space for integrating an RTD. Since, the experiment would be carried out at high heat fluxes compared to study I, higher temperatures were expected. ITO is known to work as a linear RTD below 150°C[31], as a precautionary measure, Nickel RTDs were implemented. Nickel has a higher operating window and is linear upto 200°C[31]. Moreover, Nickel is easy to deposit using e-beam evaporation and provides higher sensitivity compared to ITO.

The heater was connected to busbars to reduce the contact resistance with wires coming from the current source. The connection for the ground and RTDs were taken out by applying silver epoxy on the busbar contact pads, wafer thickness side and on top of the wafer. Moreover, the superhydrophilic area on the ground (bottom) chip is aligned with the EWOD pathway on the EWOD (top) chip. Deionized water is used as the coolant of choice owing to its high specific heat, latent heat of vaporization and high mobility on the EWOD platform.

The heater was coated with a 100 nm chromium base layer separated by 1 μm of silicon dioxide as an insulation layer to isolate the RTD. This metal base layer is required to enable deposition of an alumina superhydrophilic layer

4.4 RTD calibration

As mentioned earlier, Nickel was chosen instead of ITO as RTD/heater due to a larger operating window. The RTD was calibrated in a motor oil bath placed on a hot plate. The 4-wire resistance of the RTD was measured using a DAQ operated through labVIEW at increasing temperatures (25°C to 150°C) set by the hot plate. Similarly, the same process was repeated for decreasing temperatures from 150°C to 25°C. This procedure has been detailed in [31] . The heating and cooling cycle is done to ensure repeatability as shown in Figure 4.11.

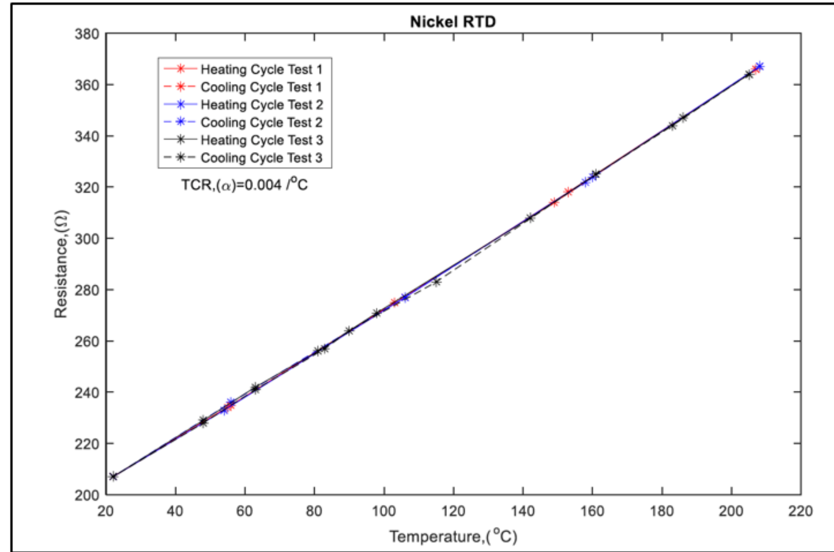

Figure 4.11. Calibration curve for Nickel RTD [31].

4.5 Fabrication

Fabrication of the EWOD (top) and ground (bottom) chips were carried out at Shimadzu institute for research technologies, UT Arlington. Similar to study I, the EWOD devices can be fabricated using photolithography processes in a cleanroom

environment. All baking steps mentioned hereafter have the same cooling time as the baking time unless otherwise mentioned.

4.5.1 Cleanroom fabrication

The EWOD (bottom) chip fabrication is exactly the same as in study I as outlined in section 3.4 except the wafer is diced at the end. Figures 4.12 and 4.13 show the process flow for entire fabrication process for study II EWOD (top) and ground (bottom) chips.

The ground chip consists of a 5.8cmx4.1cm ITO wafer drilled with a single hole for fluidic connection. It is cleaned with acetone, IPA and methanol and rinsed with DI water. After dehydrating at 180°C for 5 minutes, the ITO is patterned using photolithography to create a V-shaped groove to embed the Nickel RTD. This is done using a transparency mask affixed to 5"x5" soda lime glass. All transparency masks were printed at CAD/Art services inc. After stripping the photoresist and another

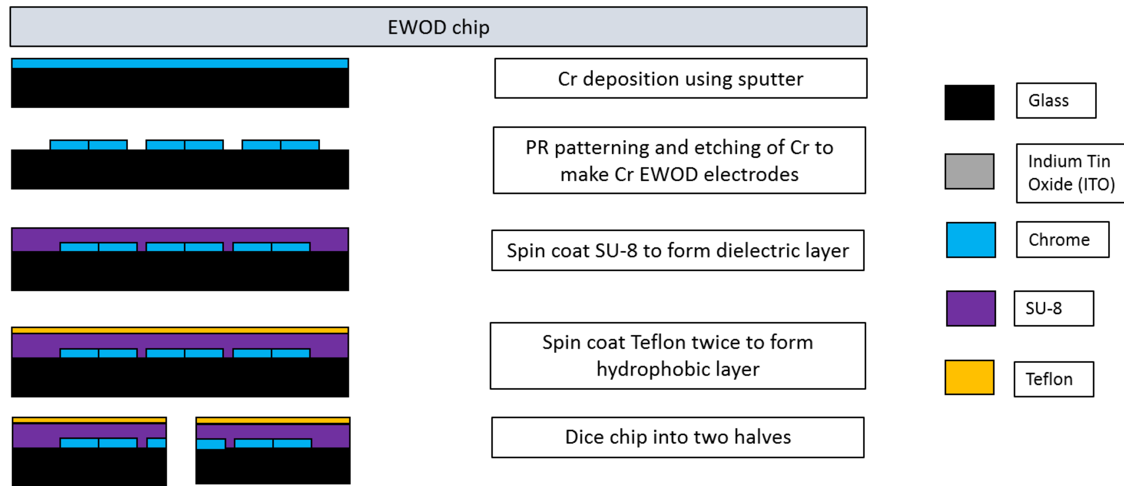

Figure 4.12. Photolithography process for EWOD (top) chip.

round of cleaning with acetone, IPA and methanol, the wafer is dehydrated at 180°C

for 5 minutes. The cleaned wafer is loaded into an e-beam evaporator and a 100 nm layer of Nickel was deposited on the wafer at 50 nm/second deposition rate. The deposited nickel was then aligned and patterned to form RTDs inside the V-shaped ITO groove formed earlier. After inspecting the pattern, the substrate was hard

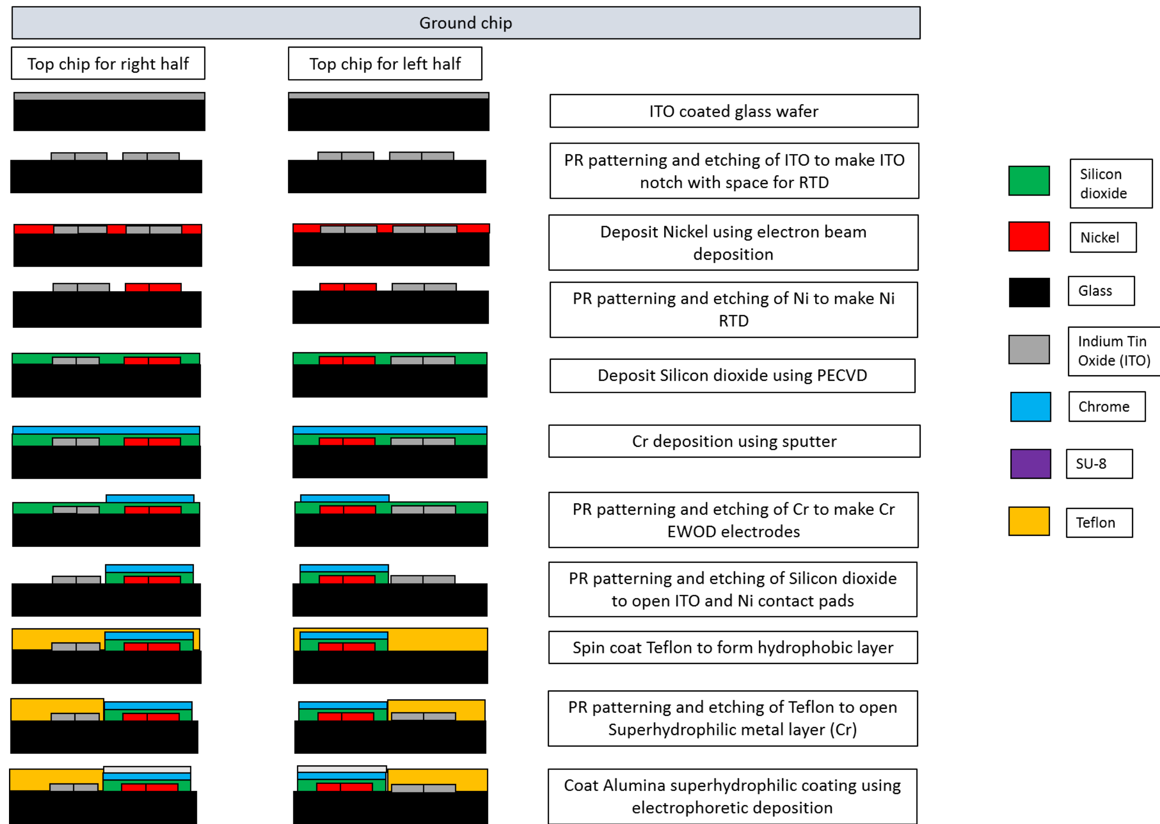

Figure 4.13. Photolithography process for ground (bottom) chip.

baked at 135°C for 5 minutes. The wafer was dipped intermittently in a hydrochloric acid bath to remove the native oxide layer. Thereafter, Water and Nitric acid in a 1:8 mixture was used to etch the nickel. The etching was continued until it was visually confirmed that there is no stray nickel. The wafer was inspected under the

Pressure (mtorr)	Power (W)	SiH_4 (sccm)	N_2 (sccm)	N_2O (sccm)	Deposition time (seconds)	Deposition rate (nm/min)
700	400	12	102	141	4500	2000

Table 4.1. PECVD parameters

microscope for accuracy. Thereafter. PR was stripped, cleaned and dehydrated for the next process.

To isolate the RTD and superhydrophilic base layer, a passivation layer consisting of Silicon dioxide was deposited on top of the Nickel RTDs. SiO_2 was deposited using plasma enhanced chemical vapor deposition (PECVD) at 360°C. PECVD parameters are listed in table 4.1. These parameters yield a uniform 1.5μm thin film. A low deposition rate was chosen to reduce stresses in the film. The wafer was cleaned to prepare it for sputtering chromium. Thereafter, the 100 nm sputtered chromium layer was patterned.

After depositing the insulation layer, a 100 nm layer of chromium was sputtered after cleaning and dehydrating the wafer. The chromium layer once deposited was cleaned and patterned to form an octagonal box on top of the RTD. On completion of the patterned chromium base layer, the Silicon dioxide is patterned and etched using 10:1 buffered oxide etchant for 8 minutes.

This etching process now opens up the nickel and ITO contact pads required for connecting the RTD and ground for EWOD respectively. The wafer was then cleaned and teflon was spin coated using recipe in table 3.1 to form the hydrophobic layer. As teflon is hydrophobic, photoresist has poor adhesion. To improve the adhesion, the wafer was etched for 5 seconds at 300W (25 sccm Argon gas) using reactive ion etching (RIE). This roughens up the teflon layer and allows us to proceed with patterning.

Once developed, the PR coated wafer is again etched using RIE for 15 minutes at 300W (25 sccm Argon gas).

Thereafter, the PR is stripped using 1165 PR stripper at 75°C for 10 minutes. The wafer is allowed to cool on a cool plate instead of water bath as nickel is sensitive to sudden temperature changes. On cooling, the ground (bottom) chip was immersed in a water bath and gently blow dryed to prevent peeling of teflon. Since, only one reservoir is required, the 4 inch wafer containing the EWOD (top) chip is diced into two halves each containing its own reservoir and EWOD pathways. The ground (bottom) chips were drilled appropriately to locate the hole on the top of reservoir for each half of the EWOD (top) chip. The patterning was also adapted accordingly.

Finally, both the devices (EWOD and ground) were annealed at 180°C in an oven for 5 hours to yield a uniform teflon coating and to evaporate all the solvent. The chip was coated with electrophoretically deposited alumina nanoparticles to form the superhydrophilic coating using the procedure described in [46]. This completes the fabrication of the EWOD (top) and ground (bottom) chip.

4.5.2 Electrophoretic deposition

Following the completion of the ground (bottom) chip using photolithography, the superhydrophilic coating was deposited on the chromium coated octagon. An ethanol solution with magnesium nitrate charging salt was prepared and alumina nanoparticles were dispersed. This solution was prepared in accordance with the procedure described in [46]. The solution was agitated using a ultrasonicator for 3 hours to prevent aggregation of the nanoparticles. Subsequently, the electric field was applied across the suspended chromium and graphite electrodes maintained at 1 cm gap. Owing to the electric double layer formation on the nanoparticles, they are electrophoretically deposited on the chromium coated octagon. Precautions were

taken to tape the ITO and nickel contact pads to prevent any stray deposition. After the completion of the process, the ground (bottom) chip coated with alumina nanoparticles was baked in an oven at 180°C for 15 minutes to regain the hydrophobicity lost by the surrounding teflon. Figure 4.14 shows a schematic representing a general electrophoretic deposition technique showed by boccaccini et al. [47].

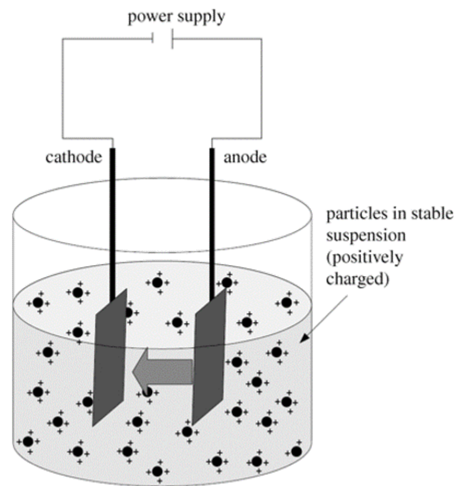

Figure 4.14. Electrophoretic deposition of alumina nanoparticles [47].

4.6 Experiment

4.6.1 Setup and methodology

To conduct the experiments with the EWOD (top) and ground (bottom) chip, the chips need to be assembled in parallel plate configuration and held in place in this arrangement with supporting elements. Lexan™ was used to produce transparent polycarbonate pieces which were used to secure the EWOD (top) chip and the vertical connectors called ZEBRA™ connectors to interface the chip with the PCB. The entire setup was held with machine screws and nuts. Figure 4.15 shows the Lexan based EWOD setup with ZEBRA™ connectors and PCB. Double sided Kapton tape (Ted

pella inc. 16087-12) is applied on the EWOD (top) chip to form spacers in the parallel plate configuration. The ground (bottom) chip has a hole drilled prior to cleanroom processing. This hole corresponds to a fluidic connection for the inlet reservoir. A pipette tip (Eppendorf inc.) was attached and epoxy adhesive (Ace hardware quick set epoxy adhesive) was applied post fabrication to seal the connections.

Since the ground (bottom) chip is at the bottom and the electrodes are at the top, the lexan setup has to be inverted compared to study I. The inverted setup is mounted in a cutout created on a Delrin stand. This setup allows for placing a camera underneath the lexan setup to image the droplet motion. At the same time, the superhydrophilic area is exposed at the top to the environment to allow for proper venting. In addition to the camera placed below, another camera will record the liquid spreading on the superhydrophilic area from the top. Figure 4.16 the actual experimental setup based on the schematic outlined in chapter 3.

The heater on the ground (bottom) chip was connected to the current source (Keithley 2400 source-meter) by means of 24AWG wires soldered onto copper strips attached to the top side of the ground (bottom) chip using silver epoxy adhesive (MG chemicals 8331-14G). The silver epoxy was also applied on the side and underside of the ground (bottom) chip to complete the connection to the bus bars of the heater. Similarly, the ground connection was taken out and connected to the ground on the switch board.

The PCB connects to a switching board using a pair of IDE cables. The switching board has 96 high voltage high speed relays corresponding to 96 outputs on the National instruments PCIe-6509 DAQ. The switch board is connected to the DAQ through another pair of IDE cables. The switching board is powered by a combination of function/arbitrary waveform generator (Keysight 33220A) routed through a voltage amplifier (TReK PZD350). The EWOD electrodes are switched ON/OFF using a

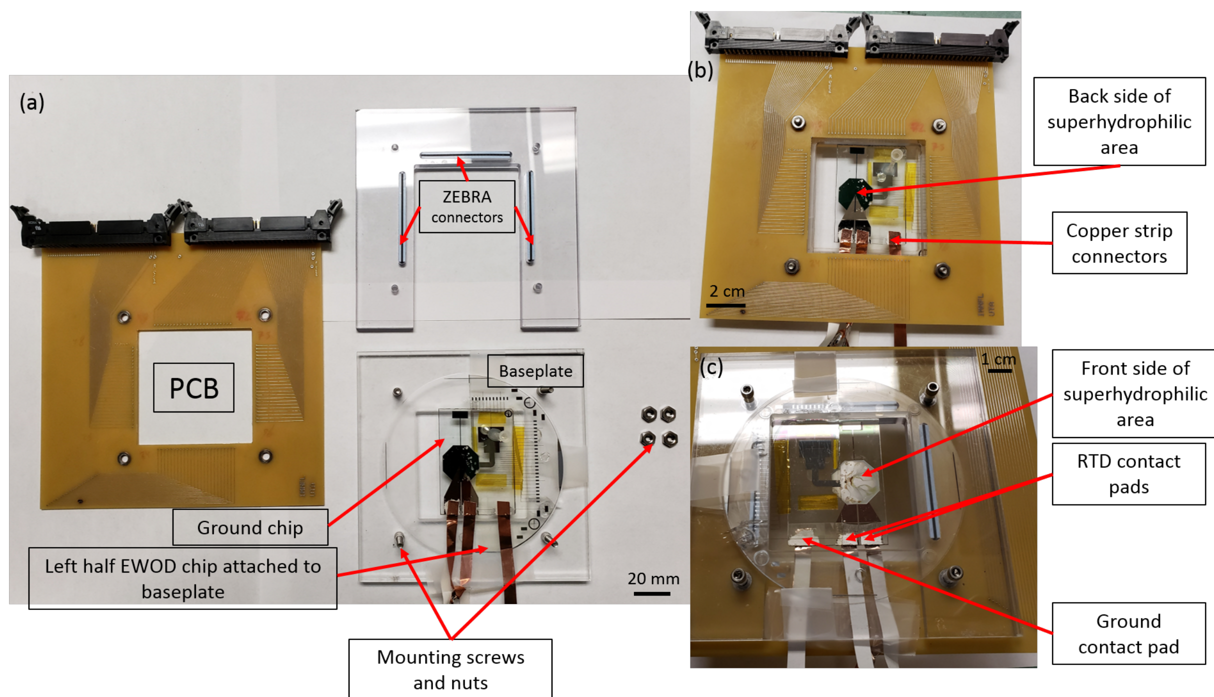

Figure 4.15. (a) Various elements of EWOD setup Lexan pieces assembled with PCB: (b) Front side (c) Back side.

labVIEW program which interfaces with the NI DAQ which in turn switches the relays corresponding to the electrodes on the chip. The switching of electrodes is automated inside labVIEW by feeding a text file containing the actuation scheme for various operations.

The RTD is operated through a separate labVIEW program interfacing with the current source. The current required for heating could be adjusted in the program. The resistance is measured using 4-wire method every 40ms to capture the temperature changes during evaporation. Prior to starting the experiment, the ground (bottom) chip is placed aligning the heater with the EWOD flow path and pressed to ensure a steady gap between the plates. The pipette tip corresponding to the inlet reservoir is connected to a syringe by means of tubing (TYGON) and then placed in a syringe

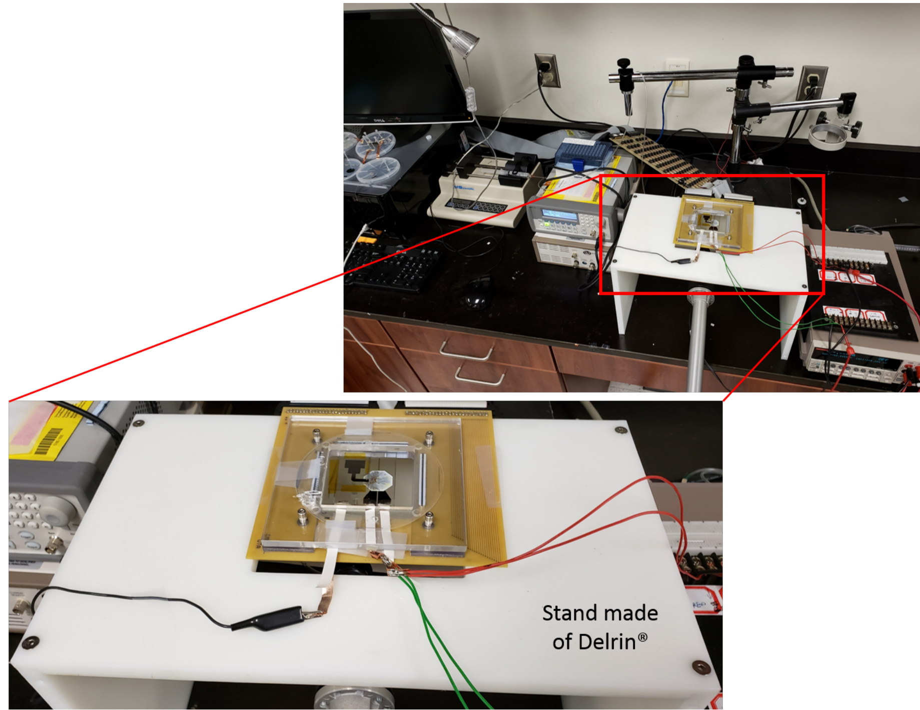

Figure 4.16. Pictures of EWOD setup. EWOD inverted and mounted on a stand with superhydrophilic area facing up.

pump (KDS 100). The outlet pipette tip is connected to a syringe which is operated manually.

The droplet motion is visualized using a Hitachi camera (KP-D20A) affixed to a tripod beneath the inverted EWOD setup. The video obtained is recorded using OBS studio software. On completion of this setup, the heater is switched on by starting the corresponding labVIEW program and the heater is allowed to reach steady state. After about a minimum of 300s, the syringe pump and EWOD automation program are turned on and the hotspot temperature is continuously monitored. Variation in resistance of the RTD is captured and converted into temperature data using the calibration equation. The flow rate of the syringe pump is adjusted to match the generation rate of droplets.

4.7 Droplet spreading over superhydrophilic area

Owing to the superhydrophilicity, the droplet gets sucked into the area as soon as it arrives close to the superhydrophilic region. On entering the region, majority of the volume of the droplet stays at the entrance while a thin film or fringe steps out as shown in Figure 4.17. This thin film spreads rapidly due to the high capillary force in the region. The thickness of this thin film during this initial spreading phase is high.

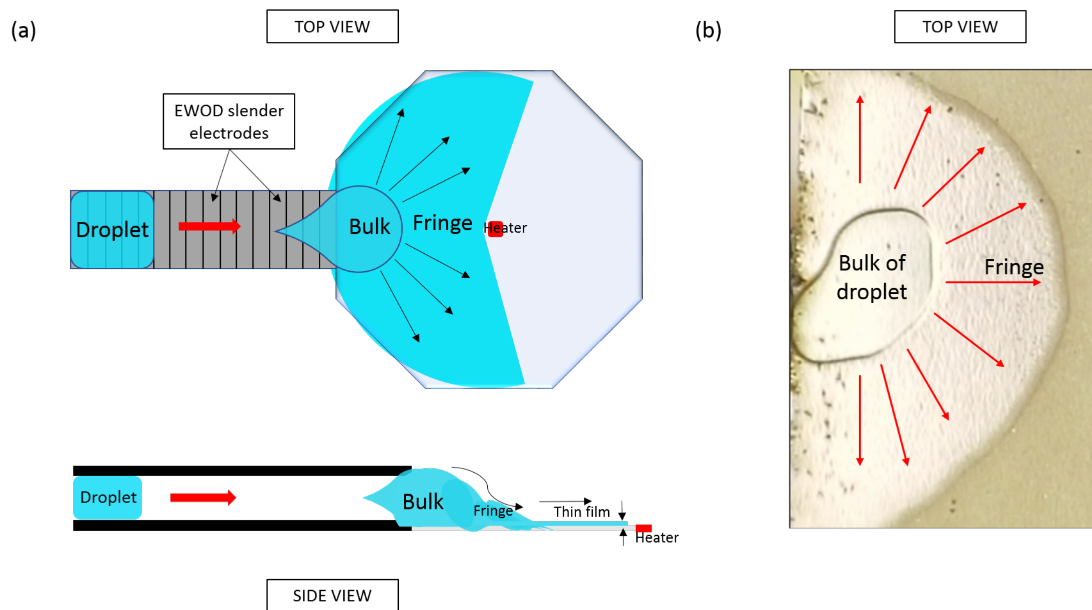

Figure 4.17. (a) Schematic of droplet spreading in superhydrophilic area (b) Photograph of sandwiched droplet spreading in superhydrophilic area.

As explained in section 4.1, the bulk of the droplet keeps replenishing the fringe until the bulk itself starts receding. The fringe keeps moving forward until it can no longer sustain due to the bulk shrinking. Once no more droplets are supplied to the superhydrophilic region, the fringe starts receding into the bulk and dryout eventually

happens. While the fringe is receding, its thickness drops considerably allowing for thin film evaporation to occur.

4.8 Results

Figure 4.18 shows the variation of the hotspot temperature $T_{hotspot}$ with time correlated with spreading of the liquid film on the superhydrophilic area. The plot can be divided into various sections depending on the progress of liquid film. Initially, the heater is allowed to reach steady state for 340s as evidenced by the flatlining of the curve. As soon as electrowetting is switched on, a sharp decrease in temperature is observed. Initially, the liquid wets the periphery of the area slowly spreading towards the hotspot as more droplets are supplied to the superhydrophilic region. After a certain period of time, as liquid continues evaporating, the liquid film starts to recede. This eventually results in an intermittent dryout phase until the more droplets are supplied to re-wet the region around the hotspot. This experiment was performed for heat fluxes of 60 and 100 W/cm^2 but the analysis will be carried out only for 100 W/cm^2 data. This behavior was visible in the 60 W/cm^2 case as well.

4.8.1 Spreading phase

The experiment involves repeatedly supplying droplets to replenish the liquid lost by evaporation. On continuous supply of droplets, the liquid formed a bulk and fringe whose movement followed a certain pattern. This movement pattern could be categorized into three different phases out of which the 1st phase is spreading. Figure 4.19 highlights the various spreading events happening throughout the experiment showing the temperature and visual data. This phase is accompanied by a sharp drop in temperature of various degrees depending on the extent of spreading. Owing

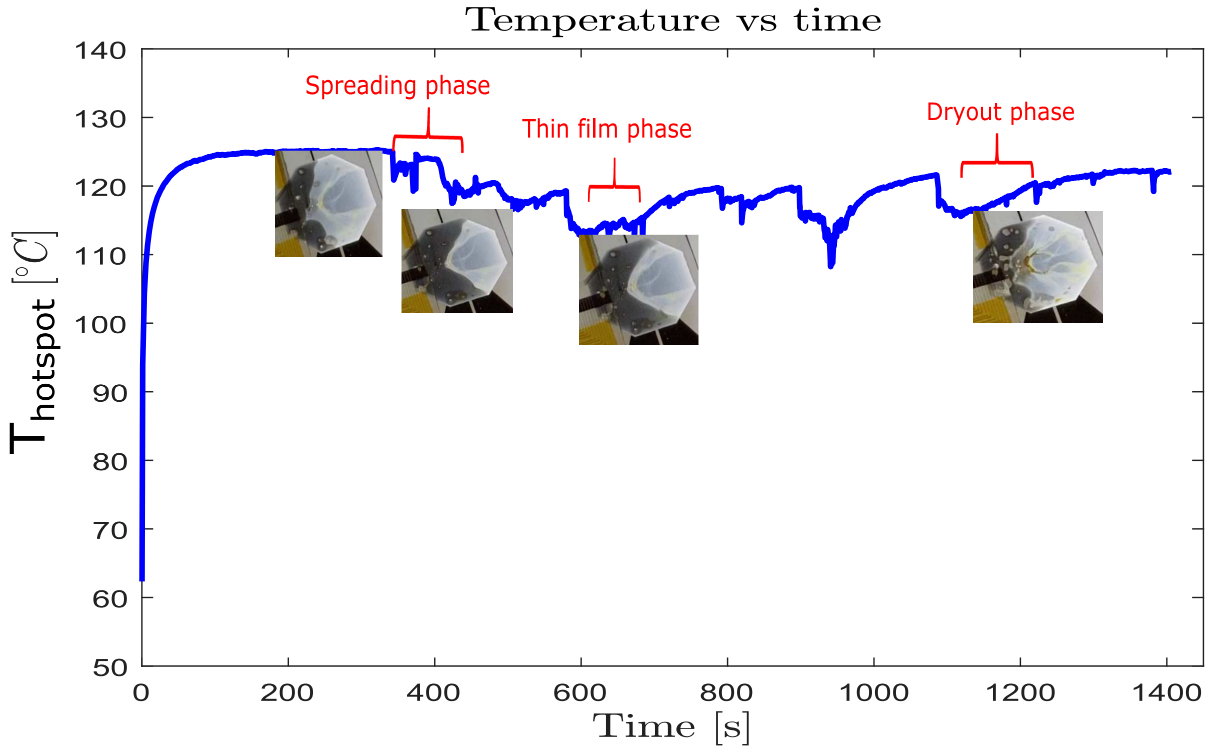

Figure 4.18. Hotspot temperature variation during the entire experiment. Images show various stages of liquid film propagation.Heat flux = 110 W/cm^2, inter-droplet delay = 5s, switching time = 500 ms, operating voltage = 150 ACV at 1 kHz.

to the superhydrophilic coating, there is a high capillary pressure driving the liquid across the superhydrophilic area. Initially, the large supply of liquid produces a fringe-bulk situation. The bulk of the droplet stays back at the entrance to the superhydrophilic region. A thin fringe steps out of the bulk and spreads towards the hotspot. This fringe however, is still not adequately thin (10microns) to induce thin film evaporation. Hence, the drop in temperature observed can be attributed primarily to convection.

Since, convection is the dominant mode of heat transfer at this stage, it makes sense that the spreading area has a direct effect on the extent of the temperature drop in each of these cases. The largest temperature drop is associated with the maximum coverage of the droplet around the hotspot. Inspite of the high coverage,

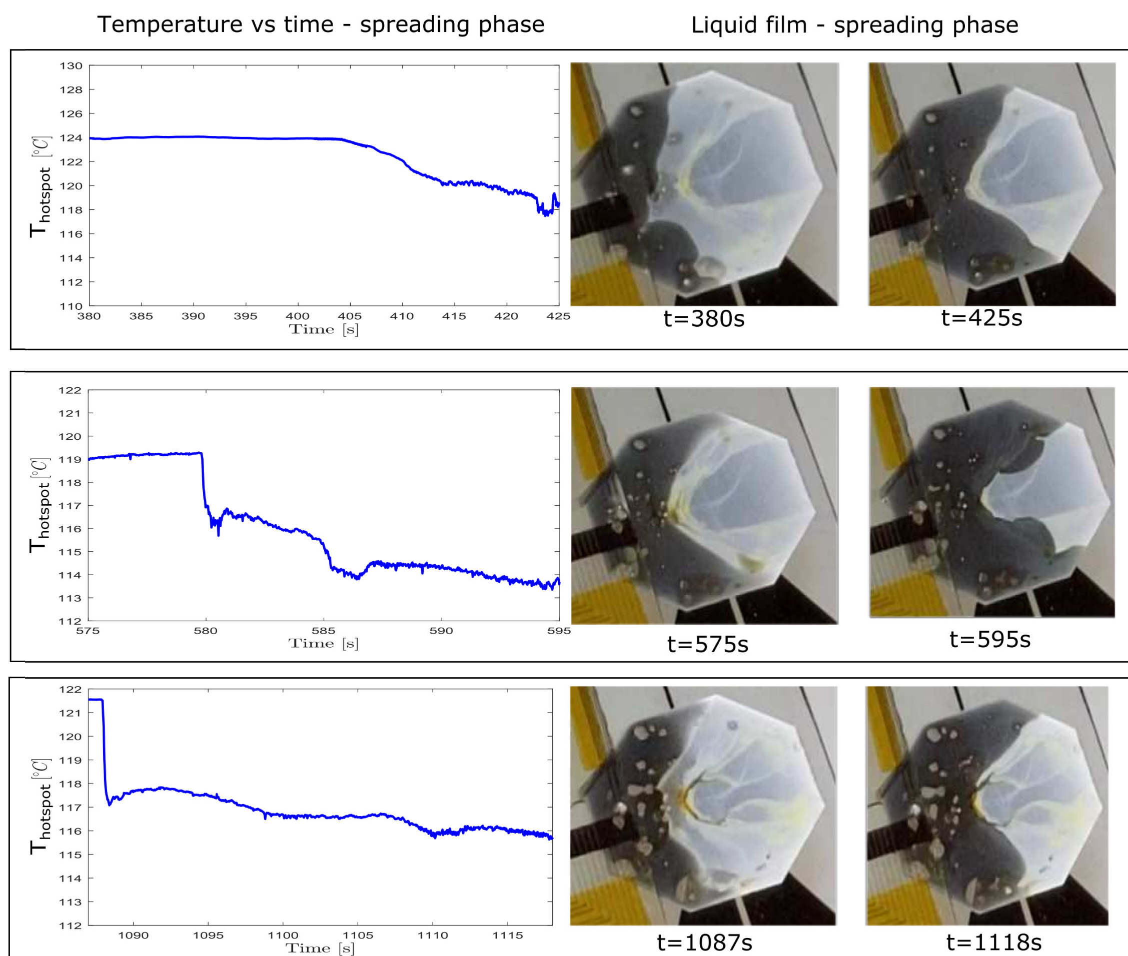

Figure 4.19. Hotspot temperature and extent of spreading. Heat flux = 110 W/cm^2, inter-droplet delay = 5s, switching time = 500 ms, operating voltage = 150 ACV at 1 kHz.

the spreading does not seem to completely wet the hotspot. This could be due to the high rate of evaporation over the hotspot.

Due to the superhydrophilic coating being made of alumina, it has a thermal conductivity of 26 W/mK which makes the temperature distribution on the surface non-uniform. The highest temperature is exactly over the hotspot with the temperature reducing as we move away from it. With high heat flux, the wicking speed is not able to keep up with the rate of evaporation, thus causing a dry spot over the hotspot.

4.8.2 Thin film phase

Once the thick liquid film spreads over the superhydrophilic area and the bulk is no longer able to replenish the liquid lost due to evaporation, the receding of the liquid film is observed. Figure 4.20 shows the temperature and visual data for various instances of receding liquid film throughout the experiment. This phase sees a maintaining of the hotspot temperature after the initial temperature due to spreading. Once the liquid front stops moving, there is constant wicking of the liquid due to the

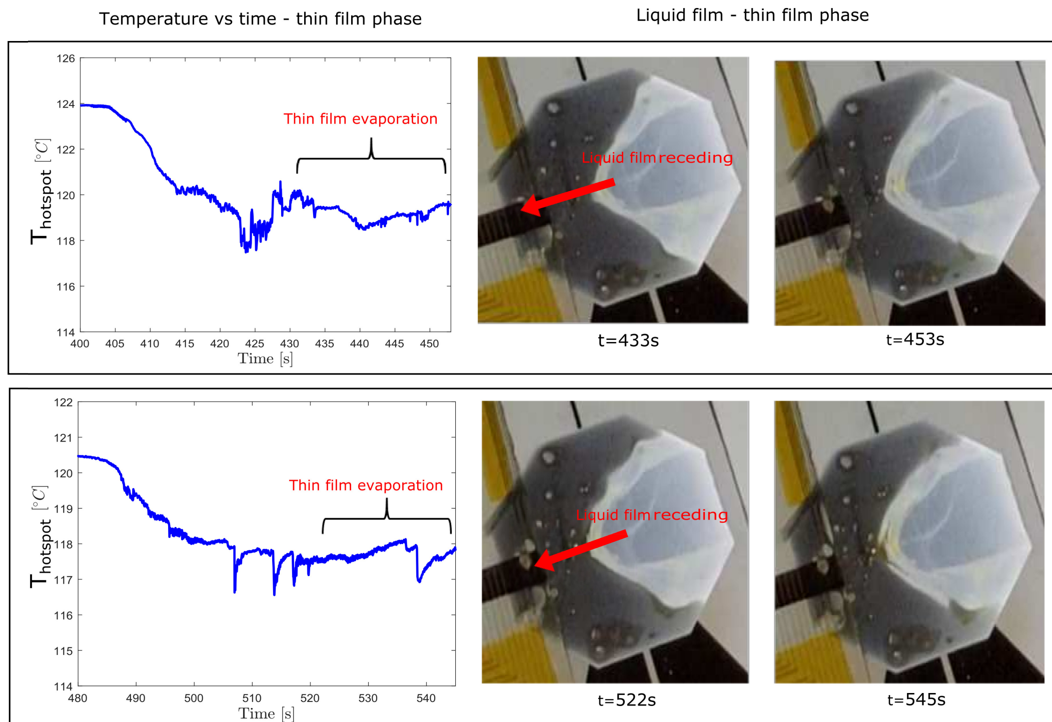

Figure 4.20. Hotspot temperature and receding of liquid film. Heat flux = 110 W/cm^2, inter-droplet delay = 5s, switching time = 500 ms, operating voltage = 150 ACV at 1 kHz.

capillary forces. Due to the high temperature encountered by the liquid film at various points on the surface, evaporation starts happening. The liquid film front is determined by the balance of capillary wicking and evaporation. The balance is

maintained for a brief period of time after the wicking speed is not able to keep up with the evaporation rate.

As long as the wicking speed and evaporation rate are equal, the hotspot is maintained at a constant temperature. As the liquid film begins to recede, the thickness of the liquid film reduces. Hence, the liquid undergoes thin film evaporation and with the help of the superhydrophilic surface, the thin film area is also maximized. So, from the initial phase where convection is dominant, the cooling slowly transitions into thin film evaporation as the liquid film starts to recede. Ideally, the device should always be operated in this mode to cool the hotspot and maintain its temperature.

4.8.3 Dryout phase

As the liquid film recedes, the hotspot temperature remains constant. However, the temperature remains constant only for a brief period of time followed by a slow increase. This increase in hotspot temperature happens in every instance after the droplet recedes as shown in Figure 4.21. The constant receding of the droplet should ensure a constant hotspot temperature but that is not the case. As the droplet recedes, the coverage area also changes and the liquid film becomes further away from the hotspot. Hence, the temperature changes back to a higher value corresponding to a different degree of spreading. In the absence of subsequent liquid supply, this can be perceived as intermittent dryout as the liquid film recedes back to the bulk. The bulk does not have enough liquid to produce a fringe in the presence of evaporation. As mentioned in section 4.1, in the absence of bulk flow coming from the bulk meniscus, the droplet will recede and the area will eventually dryout.

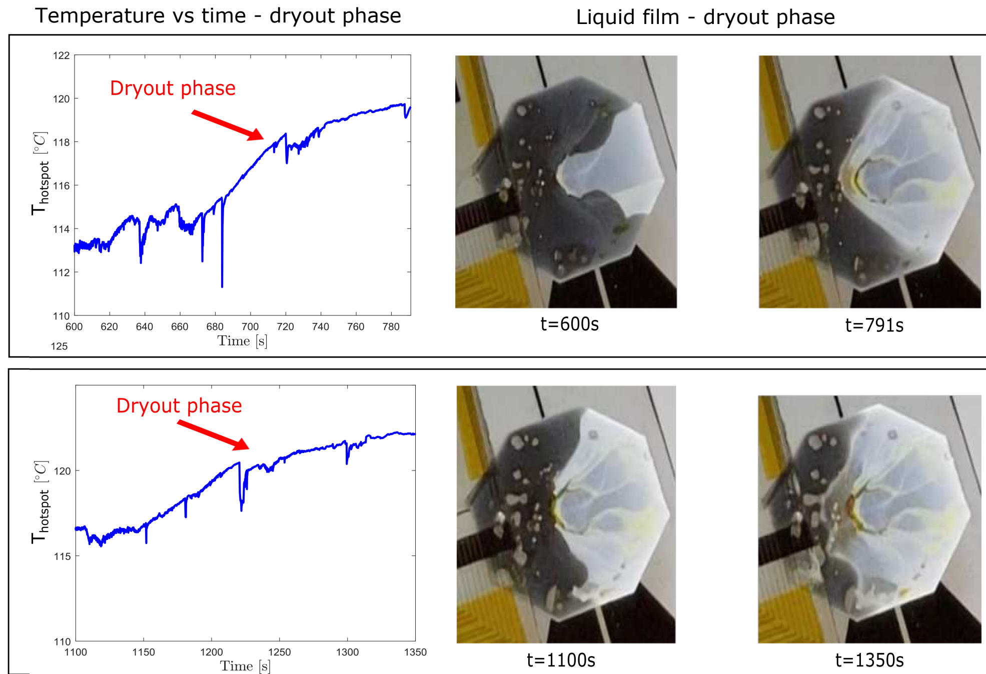

Figure 4.21. Hotspot temperature and dryout of liquid film over hotspot. Heat flux = 110 W/cm^2, inter-droplet delay = 5s, switching time = 500 ms, operating voltage = 150 ACV at 1 kHz.

4.9 Discussion

4.9.1 Thermal circuit analysis - baseline

The hotspot attached to the superhydrophilic area could be modeled as a chip attached to a heat sink as shown in Figure 4.22. The baseline case assumes there is no liquid film present on the superhydrophilic area. Table 4.2 lists the material properties and dimensions used to calculate the thermal resistances. In the baseline case, the total thermal resistance is composed of the conduction resistances of the individual layers, the spreading resistance and the convection thermal resistance over the top surface. In the absence of evaporation, convection is main mode of heat transfer to the ambient. To account for thermal spreading within the layers, Lee et al. [48] developed an analytical model to predict spreading resistances within multiple layers. To avoid singularities, the rectangular chip is modeled as a circular chip with a circular hotspot

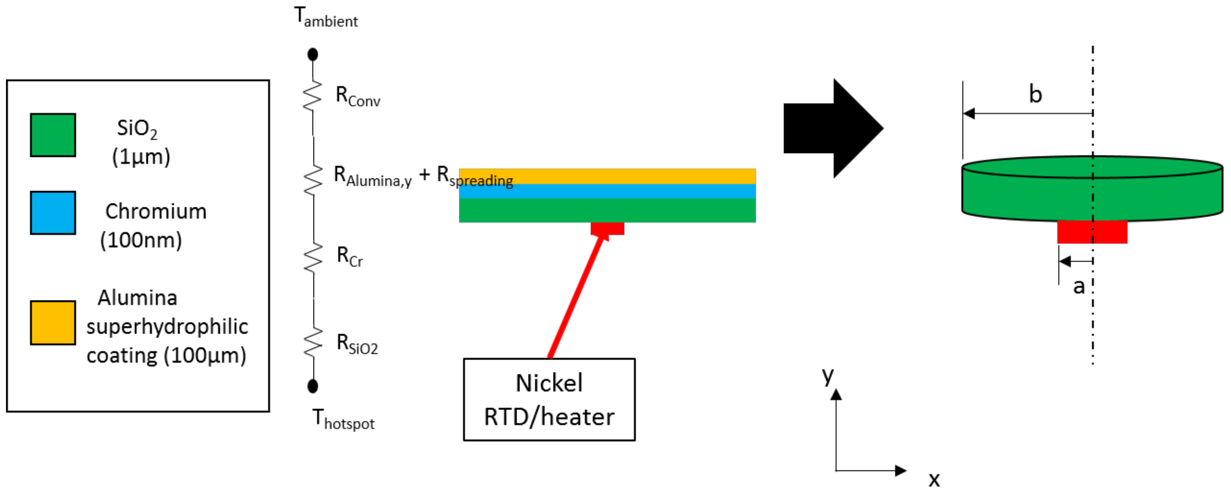

Figure 4.22. Approximation of rectangular substrate as equivalent circular model.

as shown in Figure 4.22. The radii a and b of the layers and hotspot are the equivalent radii of their rectangular counterparts. Listed below are the equations for finding the spreading thermal resistance using the model developed by Lee at al. [48].

$$a = \sqrt{A_s/\pi} \tag{4.1}$$

$$b = \sqrt{A_p/\pi} \tag{4.2}$$

$$\Psi = \frac{1}{2}(1-\epsilon)^{3/2} \tag{4.3}$$

$$\phi_C = \frac{tanh(\lambda_C \tau) + \lambda_C/Bi}{1 + \frac{\lambda_C}{Bi} tanh(\lambda_C \tau)} \tag{4.4}$$

$$\lambda_C = \pi + \frac{1}{\sqrt{\pi}\epsilon} \tag{4.5}$$

$$R_{spreading} = \frac{\Psi_{avg}}{ka\sqrt{A_s}} \tag{4.6}$$

where,

A_s = Cross-sectional hotspot area

A_p = Cross-sectional area of layers above hotspot

a = equivalent radius of hotspot

b = equivalent radius of layers above hotspot

ϵ = ratio of equivalent radii a and b, a/b

Bi = Biot number, $h_{conv}b/k_{Alumina}$

τ = ratio of alumina thickness and equivalent radius b, t/b

Ψ_{avg} = Average dimensionless spreading resistance

$R_{spreading}$ = Spreading thermal resistance

The spreading resistance for the Chromium and silicon dioxide layers were calculated to be very high($\sim 10^5$ $^\circ C/W$) and hence spreading can be neglected in these layers. By accounting for spreading only in the alumina layer, the total conduction resistance is given by:

$$R_cond = R_{Cr} + R_{SiO2} + R_{Alumina,y} \tag{4.7}$$

and the total thermal resistance,

$$R_{total} = R_cond + R_{spread} + R_{conv} \tag{4.8}$$

where,

R_{Cr} = Chromium conduction resistance

Material	Thermal conductivity, k (W/mK)	Thermal resistance (°C/W)	Length, L(m)	Area, A(m^2)
Silicon dioxide, SiO_2	1.06	0.000982	1x10^{-6}	0.00096
Chromium, Cr	90	2.77x10^{-6}	1x10^{-7}	0.0004
Alumina, Al_2O_3	26	0.009615	1x10^{-4}	0.0004

Table 4.2. Material properties and dimensions for thermal resistance calculation

R_{SiO2} = Silicon dioxide conduction resistance

$R_{Alumina,y}$ = Alumina conduction resistance in the y-direction

R_{spread} = Spreading resistance

R_{conv} = Convection resistance

A bulk thermal conductivity value has been used for alumina since calculation or characterization of the nanoscale value is beyond the scope of this work. Moreover, due to the high surface roughness of the alumina, the surface acts as a series of nanofins which increases the effective heat transfer in addition to the evaporation. This effect could be used to compensate for using the bulk thermal conductivity value. The main unknown in this thermal resistance network is the convection coefficient h_{conv}. By comparing the experimental steady state hotspot temperature with the hotspot temperature obtained using the thermal resistance network, the value of h_{conv} is guessed to be 8.5. The higher convection coefficient obtained as opposed to study I confirms our assertion about the alumina surface acting as nanofins.

4.9.2 Thermal circuit analysis considering thin film evaporation

The convection coefficient obtained from the thermalcircuit in section 4.9.1 will be plugged into a new thermal resistance model developed in the current section. In section 4.8.1, it was observed that the extent of spreading of the liquid film

over the superhydrophilic area affected the hotspot temperature. Also, the surface temperature distribution is non-uniform owing to lateral conduction on alumina surface. Taking this into consideration, there are two parallel paths for the heat to dissipate:

- Removal of heat through convection in areas where there is no liquid film
- Lateral heat spreading through conduction at the alumina surface and subsequent evaporation through the liquid film

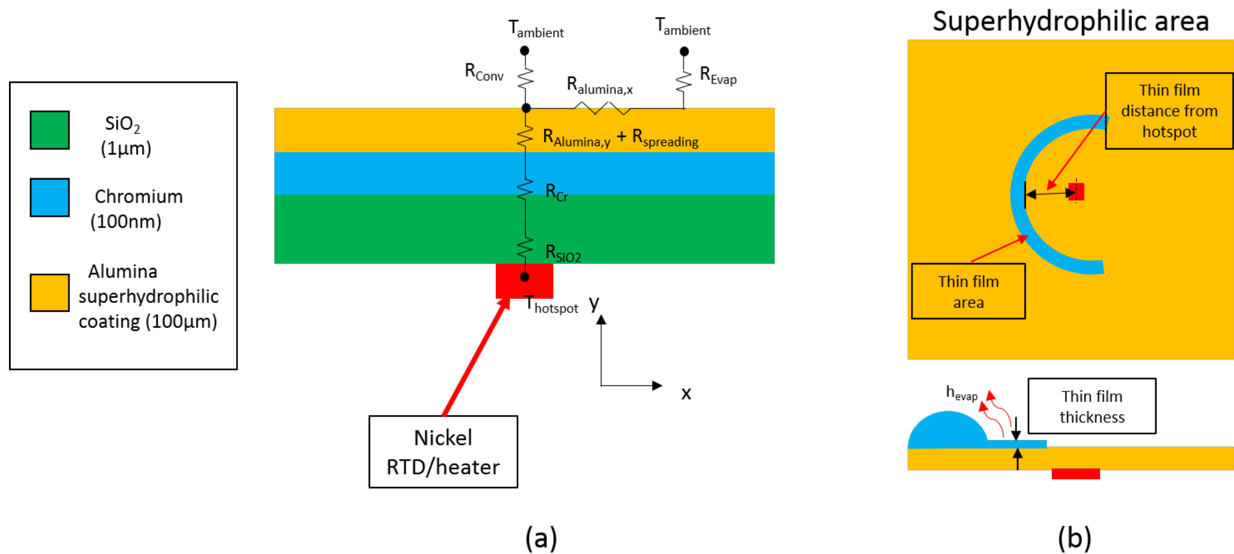

Figure 4.23. (a)Thermal resistance network with evaporation(b) Critical parameters varied to analyse heat dissipation.

Figure 4.23(a) shows the updated thermal resistance network taking these heat paths into consideration. Table 4.3 shows the additional parameters used for thermal resistance calculations. The conduction resistance through the surface is denoted

$R_{Alumina,x}$ and the evaporative thermal resistance is denoted by R_evap. The total thermal resistance is given by:

$$R_{total} = R_m + R_{spread} + R_{conv}||(R_{Alumina,x} + R_{evap}) \tag{4.9}$$

where,

R_{Cr} = Chromium conduction resistance

R_{SiO2} = Silicon dioxide conduction resistance

$R_{Alumina,x}$ = Alumina conduction resistance in the x-direction

$R_{Alumina,y}$ = Alumina conduction resistance in the y-direction

R_{spread} = Spreading resistance as calculated in section 4.9.1

R_{conv} = Convection resistance

R_{evap} = Evaporative thermal resistance

The evaporative thermal resistance is given by:

$$R_{evap} = R_L + R_{LV} \tag{4.10}$$

where,

R_L = Liquid film conduction resistance

R_{LV} = Liquid-vapor interface thermal resistance

Figure 4.23(b) shows the important parameters governing the hotspot temperature. They are:

- Evaporative heat transfer coefficient h_{evap}
- Thin film transition region area
- Thin film thickness
- Location of thin film

Critical parameters	Value
Evaporation heat transfer coefficient, h_{evap}	100000 W/m^2K
Thin film thickness	10μm
Thin film area	17.3mm^2
Thin film distance from hotspot	5 mm
Surface conduction area	1.61x10^{-7}m^2

Table 4.3. Critical parameters assumed for thermal resistance analysis

The above four parameters are the primary unknowns which need to be assumed to carry out the analysis. As mentioned in section 4.1, 80% of the evaporation takes place in the transition region of a droplet. The thin film transition region area is defined by the dimensions of the area as shown in table 4.3. Thin film thickness is assumed to be 10 microns based on the numerical model developed by Ranjan et al. [49]. In the experiments, the location of the thin film played a crucial role in cooling the hotspot. The liquid thin film is assumed to be located at distance of 5 mm from the hotspot. Based on these assumptions, the thermal resistance model is able to predict the hotspot temperature with reasonable accuracy. The parameters assumed cannot be otherwise controlled accurately in a real world experiment, so the variation of these parameters will be analysed using this model. Figure 4.24 shows the variation of hotspot temperature $T_{hotspot}$ with evaporative heat transfer coefficient h_{evap}. The hotspot shows negligible change in its temperature inspite of increasing the value to 200000 W/m^2K as predicted in Ranjan et al.'s [49] numerical model. Figure 4.25 shows the variation of hotspot temperature with thin film

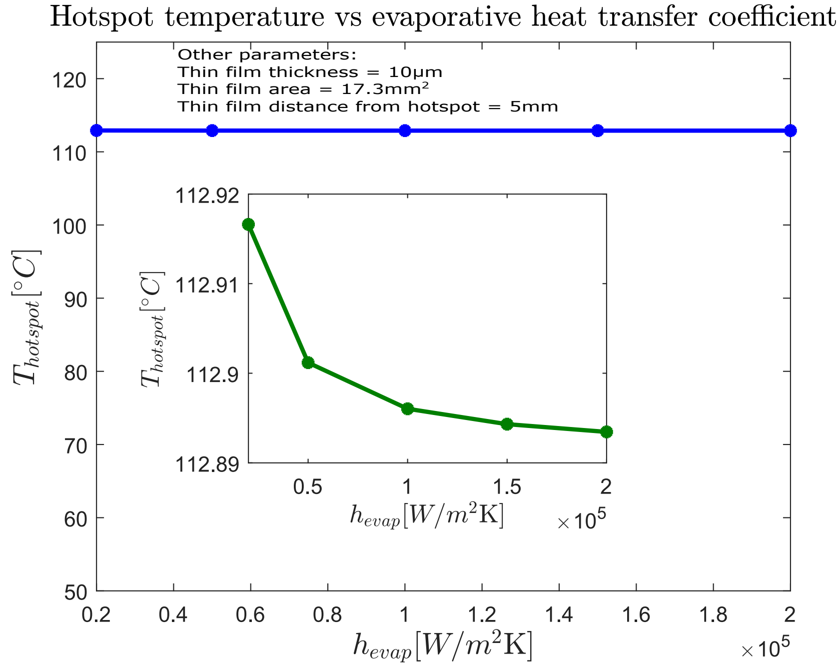

Figure 4.24. Variation of hotspot temperature with evaporation heat transfer coefficient, h_{evap}. Inset shows zoomed in view of plot.

area. Inspite of increasing the thin film area from 17.3 mm^2 to 30mm^2, there is no noticeable change in the hotspot temperature. Next, Figure 4.26(a) shows the variation of hotspot temperature with thin film location. There is dramatic reduction in hotspot temperature as the liquid thin film approaches the hotspot. This can be attributed to the equally sharp drop in surface conduction thermal resistance as shown in Figure 4.26(b). The nominal evaporative thermal resistance R_{evap} itself is very small (1.53°C/W) but the total thermal resistance is largely influenced by the surface conduction which is function of the thin film location.

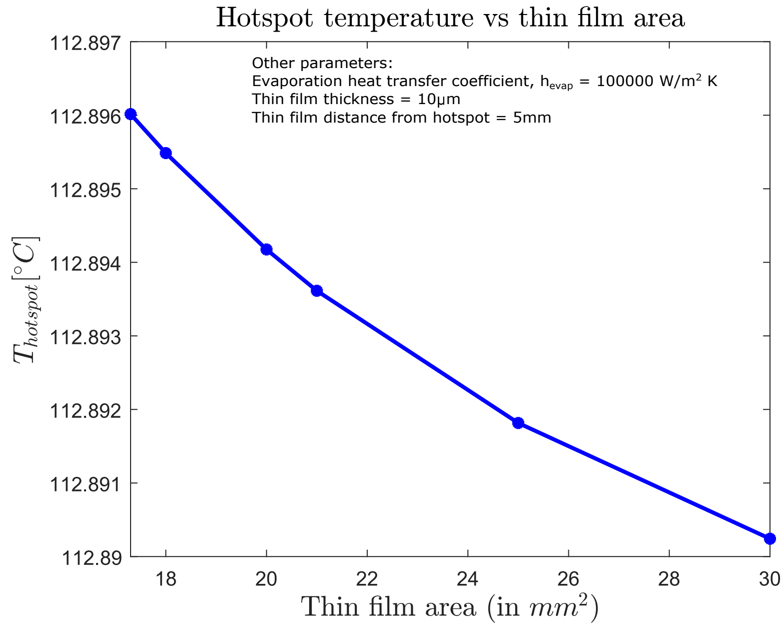

Figure 4.25. Variation of hotspot temperature with thin film area.

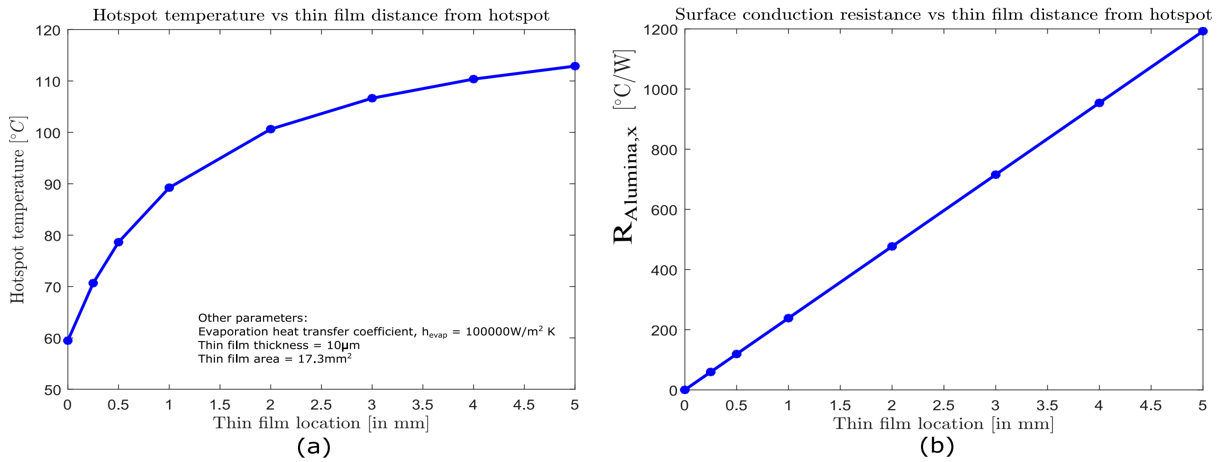

Figure 4.26. (a)Variation of hotspot temperature with thin film distance from hotspot (b) Variation of surface conduction thermal resistance with thin film distance from hotspot.

4.9.3 Comparison with Study I

Based on thermal resistance network analysis conducted in chapter 3, it was determined that convection was the dominant mode of heat transfer in Study 1. It was proposed that enhancing the evaporation is the key for the heat to favor phase change as the preferred path of heat dissipation. Based on our analysis in sections 4.9.1 and 4.9.2, it has been determined that conduction thermal resistance impedes the heat flow through evaporative liquid thin film. Due to constraints in controlling the

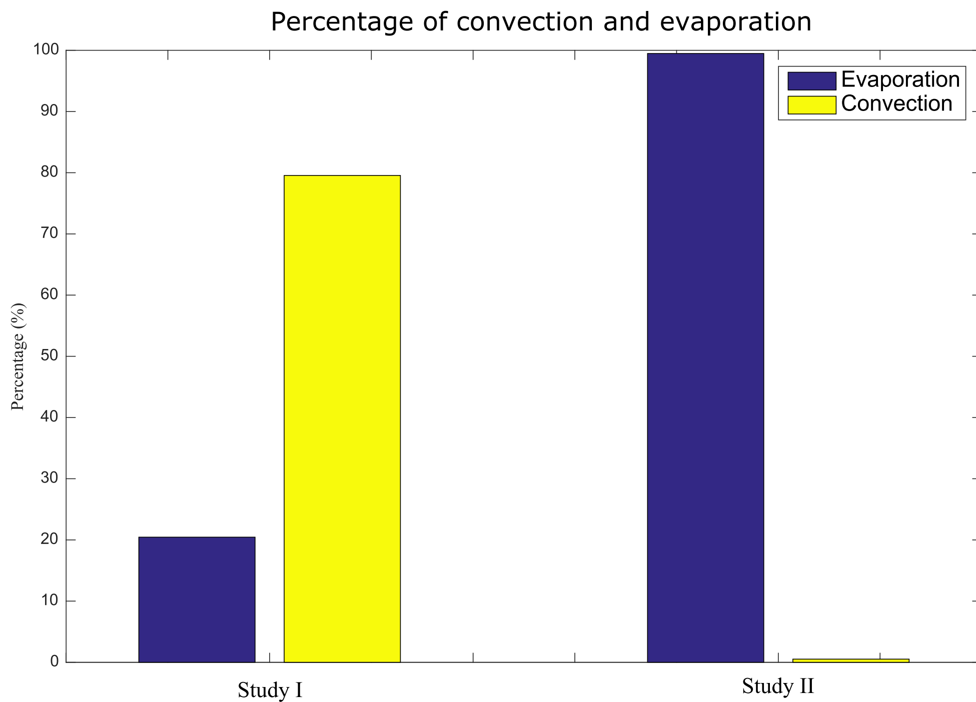

Figure 4.27. Comparison of percentage of convection and evaporation in Studies I and II.

flow of the liquid thin film in the experiment, this cannot be avoided. Conduction is a well known problem when studying evaporation as shown by[43]. The experiment

needs to be conducted in a controlled environment to make the heat dissipation purely evaporative.

Taking into account these practical issues and assume the thin film to be situated exactly over the hotspot, Figure 4.27 shows clearly marked improvement in the percentage of heat dissipation through phase change in Study II over Study I. Our original assumption to enhance evaporation to dissipate heat primarily through phase change is proved.

4.10 Conclusions

In this chapter, a superhydrophilic coating was integrated into an electrowetting device to study hotspot cooling using thin film evaporation. Visual data and hotspot temperature obtained using RTDs were synchronized and studied. The propagation of the liquid film on the superhyrdophilic surface could be classified into three different regimes based on the hotspot temperature data. Initial spreading of the liquid film caused a steep drop in temperature of 13°C owing to convection. Thereafter, the heat transfer mechanism transitioned to thin film evaporation during the recession of the thin film into the bulk of the droplet. This allowed the hotspot temperature to be sustained before increasing again during dryout caused by the thin film completely receding into the droplet bulk.

A thermal resistance analysis was carried out to study the heat dissipation mechanism in detail. It was found that owing to the non-uniform surface temperature distribution, surface conduction resistance plays a significant role in the total thermal resistance involved during heat dissipation. The influence of various evaporative parameters on hotspot temperature was studied. The evaporative thermal resistance was found to be very low compared to the convective thermal resistance but the thin film evaporation was impeded by the high surface conduction resistance.

In the ideal case, evaporation exactly over the hotspot diminished the surface conduction effect and would theoretically result in a 66°C drop in hotspot temperature. Compared to study I, theoretically, study II shows a clear improvement in the percentage of heat dissipation through phase change compared to convection.

CHAPTER 5

CONCLUSIONS

This work focuses on utilizing electrowetting on dielectric devices to study evaporative hotspot cooling. The study was conducted using two different approaches. Hotspot cooling was first implemented in a traditional parallel-plate configuration with high speed droplet transport over the hotspot. The second approach involved designing an electrowetting device integrated with a superhyrdophilic surface over the hotspot. This facilitated the use of thin film evaporation to dissipate heat and further analysis was done to study the heat transfer mechanism in detail.

- In study I, hotspot cooling was demonstrated using a high speed droplet generation scheme with sustained droplet transport. The effect of various parameters such as inter-droplet delay, switching time and heat flux was studied. A temperature drop between 5-14°C was observed for heat fluxes ranging from 20-60W/cm^2. The thermal resistance circuit of the system showed that convection was the dominant mechanism for cooling instead of droplet evaporation.
- In study II, liquid film spreading over the superhyrdophilic surface could be classified into three different phases based on the hotspot temperature data. Initial spreading of the liquid film caused a steep drop in temperature of 13°C owing to convection. Thereafter, the heat transfer mechanism transitioned to thin film evaporation during the recession of the thin film into the bulk of the droplet. This allowed the hotspot temperature to be sustained before increasing again during dryout caused by the thin film completely receding into the droplet bulk.

- A thermal resistance analysis was carried out to study the heat dissipation mechanism in detail. Surface conduction resistance plays a significant role in the total thermal resistance involved during heat dissipation. The influence of various evaporative parameters on hotspot temperature was studied. The evaporative thermal resistance was found to be very low compared to the convective thermal resistance but the thin film evaporation was impeded by the high surface conduction resistance.
- In the ideal case, evaporation exactly over the hotspot diminished the surface conduction effect and would theoretically result in a 66°C drop in hotspot temperature. Compared to study I, theoretically, study II shows a clear improvement in the percentage of heat dissipation through phase change compared to convection.

CHAPTER 6

FUTURE WORK

Based on the thermal resistance analysis performed in Section 4.9.2, it was determined that conduction resistance is significantly large compared to both convection and evaporative thermal resistances. This impedes the thin film evaporation phenomena to cool the hotspot and prevents the device from performing to its full potential. The major issue is the inability to control the thickness as well as the spreading of the liquid thin film over the superhydrophilic region. The following are suitable topics to investigate to further advance the present work:

- Since electrowetting is highly flexible and adaptive, as an extension of the current work, a method to monitor liquid film thickness will allow for precise response from the EWOD delivery system to control the thickness of the liquid film.
- The experiment could be complemented by numerical simulations to predict the spreading of a liquid film on a superhydrophilic surface and coupling it with heat transfer to study thin film evaporation in detail.
- Although, de-ionized water has been used as a coolant in this work, nanofluids and dielectric fluids hold a lot of promise to enhance the cooling capabilities of the device.
- Conducting the evaporation experiments in a controlled environment would allow for isolating the evaporation phenomena and avoid parasitic cooling effects.

- The superhydrophilic coatings could be patterned either to further increase the transition region area or to manipulate the liquid film spreading to control the thin film thickness over the hotspot.

REFERENCES

[1] M. Ojha, A. Chatterjee, G. Dalakos, P. C. Wayner Jr, and J. L. Plawsky, "Role of solid surface structure on evaporative phase change from a completely wetting corner meniscus," *Physics of Fluids*, vol. 22, no. 5, p. 052101, 2010.

[2] E. Pop, S. Sinha, and K. E. Goodson, "Heat generation and transport in nanometer-scale transistors," *Proceedings of the IEEE*, vol. 94, no. 8, pp. 1587–1601, 2006.

[3] K. Rupp, "42 years of microprocessor trend data," February 2018.

[4] A. Bar-Cohen, P. Wang, and E. Rahim, "Thermal management of high heat flux nanoelectronic chips," *Microgravity Science and Technology*, vol. 19, no. 3-4, pp. 48–52, 2007.

[5] K. S. Udell, "Heat transfer in porous media considering phase change and capillaritythe heat pipe effect," *International Journal of Heat and Mass Transfer*, vol. 28, no. 2, pp. 485–495, 1985.

[6] R. Chu, R. Simons, and G. Chrysler, "Experimental investigation of an enhanced thermosyphon heat loop for cooling of a high performance electronics module," in *Fifteenth Annual IEEE Semiconductor Thermal Measurement and Management Symposium (Cat. No.99CH36306)*, pp. 1–9, IEEE, 1999.

[7] D. Tuckerman and R. Pease, "High-performance heat sinking for VLSI," *IEEE Electron Device Letters*, vol. 2, pp. 126–129, may 1981.

[8] A. E. Bergles and A. Bar-Cohen, "Immersion cooling of digital computers," in *Cooling of Electronic Systems*, pp. 539–621, Springer, 1994.

[9] S. Campbell, W. Black, A. Glezer, and J. Hartley, "Thermal management of a laptop computer with synthetic air microjets," in *ITherm'98. Sixth Intersociety Conference on Thermal and Thermomechanical Phenomena in Electronic Systems (Cat. No.98CH36208)*, pp. 43–50, IEEE, 1998.

[10] I. Sauciuc, H. Erturk, G. Chrysler, V. Bala, and R. Mahajan, "Thermal devices integrated with thermoelectric modules with applications to cpu cooling," in *ASME 2005 Pacific Rim Technical Conference and Exhibition on Integration and Packaging of MEMS, NEMS, and Electronic Systems collocated with the ASME 2005 Heat Transfer Summer Conference*, pp. 2153–2159, American Society of Mechanical Engineers, 2005.

[11] S. G. Kandlikar and A. V. Bapat, "Evaluation of jet impingement, spray and microchannel chip cooling options for high heat flux removal," *Heat Transfer Engineering*, vol. 28, no. 11, pp. 911–923, 2007.

[12] S. G. Kandlikar, "Fundamental issues related to flow boiling in minichannels and microchannels," *Experimental Thermal and Fluid Science*, vol. 26, no. 2-4, pp. 389–407, 2002.

[13] R. J. Phillips, "Microchannel heat sinks," *Lincoln Lab. J*, vol. 1, no. 1, pp. 31–48, 1988.

[14] Linan Jiang, J. Mikkelsen, Jae-Mo Koo, D. Huber, Shuhuai Yao, Lian Zhang, Peng Zhou, J. Maveety, R. Prasher, J. Santiago, T. Kenny, and K. Goodson, "Closed-loop electroosmotic microchannel cooling system for VLSI circuits," *IEEE Transactions on Components and Packaging Technologies*, vol. 25, pp. 347–355, sep 2002.

[15] K. Pettigrew, J. Kirshberg, K. Yerkes, D. Trebotich, and D. Liepmann, "Performance of a mems based micro capillary pumped loop for chip-level

temperature control," in *Micro Electro Mechanical Systems, 2001. MEMS 2001. The 14th IEEE International Conference on*, pp. 427–430, IEEE, 2001.

[16] G. S. Bindiganavale, *Study of hotspot cooling for integrated circuits using electrowetting on dielectric digital microfluidic system*. PhD thesis, University of texas at Arlington, 2015.

[17] H. F. Hamann, A. Weger, J. A. Lacey, Z. Hu, P. Bose, E. Cohen, and J. Wakil, "Hotspot-limited microprocessors: Direct temperature and power distribution measurements," *IEEE Journal of Solid-State Circuits*, vol. 42, no. 1, pp. 56–65, 2007.

[18] G. Lippmann, *Relationship between electrical and capillary phenomena*. PhD thesis, Gauthier-Villars, 1875.

[19] B. Berge, "Electrocapilarity and wetting of insulator film by water," *C.R Acad. Sci.*, vol. Paris Ser II., no. 317, pp. 157–163, 1993.

[20] S. K. Cho, H. Moon, and C.-J. Kim, "Creating, transporting, cutting, and merging liquid droplets by electrowetting-based actuation for digital microfluidic circuits," *Journal of microelectromechanical systems*, vol. 12, no. 1, pp. 70–80, 2003.

[21] A. Dupré and P. Dupré, *Théorie mécanique de la chaleur*. Gauthier-Villars, 1869.

[22] L. Malic, D. Brassard, T. Veres, and M. Tabrizian, "Integration and detection of biochemical assays in digital microfluidic loc devices," *Lab Chip*, vol. 10, pp. 418–431, 2010.

[23] H. Moon and J. Nikapitiya, "Digital microfluidic devices and methods of dispensing and splitting droplets in digital microfluidic devices," June 23 2016. US Patent App. 14/976,019.

[24] N. J. B. Nikapitiya, M. M. Nahar, and H. Moon, "Accurate, consistent, and fast droplet splitting and dispensing in electrowetting on dielectric digital microfluidics," *Micro and Nano Systems Letters*, vol. 5, no. 1, p. 24, 2017.

[25] R. Malk, A. Rival, Y. Fouillet, and L. Davoust, "EWOD in Coplanar Electrode Configurations," in *ASME 2010 8th International Conference on Nanochannels, Microchannels, and Minichannels: Parts A and B*, pp. 239–248, ASME, jan 2010.

[26] J. B. Yaddessalage, "Study of the capabilities of electrowetting on dielectric digital microfluidics (ewod dmf) towards the high efficient thin-film evaporative cooling platform," 2013.

[27] M. M. Nahar, J. B. Nikapitiya, S. M. You, and H. Moon, "Droplet velocity in an electrowetting on dielectric digital microfluidic device," *Micromachines*, vol. 7, no. 4, p. 71, 2016.

[28] L. Shang, Y. Cheng, and Y. Zhao, "Emerging Droplet Microfluidics," *Chemical Reviews*, vol. 117, pp. 7964–8040, jun 2017.

[29] J.-T. Cheng and C.-L. Chen, "Adaptive Chip Cooling Using Electrowetting on Coplanar Control Electrodes," *Nanoscale and Microscale Thermophysical Engineering*, vol. 14, pp. 63–74, apr 2010.

[30] K. Mohseni, "Effective cooling of integrated circuits using liquid alloy electrowetting," in *Semiconductor Thermal Measurement and Management Symposium, 2005 IEEE Twenty First Annual IEEE*, pp. 20–25, IEEE, 2005.

[31] K. A. Chaudhari *et al.*, *Fabrication, Calibration and Characterization of Micro-scale Resistance Temperature Detectors.* PhD thesis, University of texas at Arlington, 2016.

[32] B. Deryagin, S. Nerpin, and N. Churaev, "To the theory of liquid evaporation from capillaries," *Kolloidn. Zh*, vol. 26, pp. 301–307, 1964.

[33] B. Derjaguin and N. Churaev, "Structural component of disjoining pressure," *Journal of Colloid and Interface Science*, vol. 49, pp. 249–255, nov 1974.

[34] J. L. Plawsky, A. G. Fedorov, S. V. Garimella, H. B. Ma, S. C. Maroo, L. Chen, and Y. Nam, "Nano- and Microstructures for Thin-Film EvaporationA Review," *Nanoscale and Microscale Thermophysical Engineering*, vol. 18, pp. 251–269, jul 2014.

[35] J. L. Plawsky, M. Ojha, A. Chatterjee, and P. C. Wayner, "Review of the effects of surface topography, surface chemistry and fluid physics on the evaporation at the contact line," *Chemical Engineering Communications*, vol. 196, pp. 658–696, dec 2008.

[36] M. Ojha, A. Chatterjee, F. Mont, E. Schubert, P. C. Wayner, and J. L. Plawsky, "The role of solid surface structure on dropwise phase change processes," *International Journal of Heat and Mass Transfer*, vol. 53, pp. 910–922, feb 2010.

[37] R. Ranjan, S. V. Garimella, J. Y. Murthy, and K. Yazawa, "Assessment of Nanostructured Capillary Wicks for Passive Two-Phase Heat Transport," *Nanoscale and Microscale Thermophysical Engineering*, vol. 15, pp. 179–194, jul 2011.

[38] Y. Nam and Y. S. Ju, "A comparative study of the morphology and wetting characteristics of micro/nanostructured Cu surfaces for phase change heat transfer applications," *Journal of Adhesion Science and Technology*, vol. 27, pp. 2163–2176, oct 2013.

[39] X. Dai, F. Yang, R. Yang, Y.-C. Lee, and C. Li, "Micromembrane-enhanced capillary evaporation," *International Journal of Heat and Mass Transfer*, vol. 64, pp. 1101–1108, sep 2013.

[40] S. Narayanan, A. G. Fedorov, and Y. K. Joshi, "On-chip thermal management of hotspots using a perspiration nanopatch," *Journal of Micromechanics and Microengineering*, vol. 20, p. 075010, jul 2010.

[41] J. Cheng and C.-l. Chen, "Active Chip Cooling Using Electrowetting with Site-specific Treatments," in *42nd AIAA Thermophysics Conference*, (Reston, Virigina), American Institute of Aeronautics and Astronautics, jun 2011.

[42] S.-Y. Park, Y. Nam, W. Wei, C.-H. Chen, and Z. Wu, "Single-Sided Digital Microfluidic (SDMF) Devices for Effective Coolant Delivery and Enhanced Two-Phase Cooling," *Micromachines*, 2016.

[43] S. Adera, D. Antao, R. Raj, and E. N. Wang, "Design of micropillar wicks for thin-film evaporation," *International Journal of Heat and Mass Transfer*, vol. 101, pp. 280–294, oct 2016.

[44] K. F. Wiedenheft, H. A. Guo, X. Qu, J. B. Boreyko, F. Liu, K. Zhang, F. Eid, A. Choudhury, Z. Li, and C.-H. Chen, "Hotspot cooling with jumping-drop vapor chambers," *Applied Physics Letters*, vol. 110, p. 141601, apr 2017.

[45] D. F. Hanks, Z. Lu, J. Sircar, T. R. Salamon, D. S. Antao, K. R. Bagnall, B. Barabadi, and E. N. Wang, "Nanoporous membrane device for ultra high heat flux thermal management," *Microsystems & Nanoengineering*, vol. 4, p. 1, dec 2018.

[46] A. Balram, S. Santhanagopalan, B. Hao, Y. K. Yap, and D. D. Meng, "Electrophoretically-deposited metal-decorated cnt nanoforests with high thermal/electric conductivity and wettability tunable from hydrophilic to superhydrophobic," *Advanced Functional Materials*, vol. 26, no. 15, pp. 2571–2579, 2016.

[47] A. Boccaccini, S. Keim, R. Ma, Y. Li, and I. Zhitomirsky, "Electrophoretic deposition of biomaterials," *Journal of the Royal Society Interface*, vol. 7, no. suppl_5, pp. S581–S613, 2010.

[48] S. Song, V. Au, and K. P. Moran, "Constriction/spreading resistance model for electronics packaging," in *Proceedings of the 4th ASME/JSME thermal engineering joint conference*, vol. 4, pp. 199–206, 1995.

[49] R. Ranjan, J. Y. Murthy, and S. V. Garimella, "A microscale model for thin-film evaporation in capillary wick structures," *International Journal of Heat and Mass Transfer*, vol. 54, no. 1-3, pp. 169–179, 2011.